Universidade de Aveiro Departamento de Engenharia Mecânica
2016

Xin Xue

Modelação e controlo do retorno elástico torcional em estruturas automóveis leves com secção transversal complexa

Modelling and control of twist springback in lightweight automotive structures with complex cross-sectional shape

Universidade de Aveiro Departamento de Engenharia Mecânica
2016

Xin Xue

Modelação e controlo do retorno elástico torcional em estruturas automóveis leves com secção transversal complexa

Modelling and control of twist springback in lightweight automotive structures with complex cross-sectional shape

Tese apresentada à Universidade de Aveiro para cumprimento dos requisitos necessários à obtenção do grau de Doutor em Engenharia Mecânica, realizada sob a orientação científica da Doutora Gabriela Tamara Vincze, Professora Auxiliar Convidada do Departamento de Engenharia Mecânica da Universidade de Aveiro

Apoio financeiro da FCT e do FSE no
âmbito do III Quadro Comunitário de
ApoioSFRH/BD/103010/2014

In memory of Prof. José Joaquim de Almeida Grácio (1959-2014)

o júri

presidente

Prof. Dr. António Manuel Rosa Pereira Caetano
Professor catedrático da Universidade de Aveiro

Prof. Dr. Frédéric Gérard Barlat
Professor catedrático da Pohang University of Science and Technology (POSTECH), Korea

Prof. Dr. Catalin Radu Picu
Professor catedrático do Rensselaer Polytechnic Institute, Troy, USA

Dr. Edgar Fernand Rauch
Directeur de Recherche au Centre National de la Recherche Scientifique (CNRS), Grenoble INP, França

Prof. Dr. Abel Dias dos Santos
Professor associado da Faculdade de Engenharia da Universidade do Porto

Prof.ª Dr.ª Marta Cristina Cardoso Oliveira
Professora auxiliar da Faculdade de Ciências e Tecnologia da Universidade de Coimbra

Prof. Dr. António Manuel de Bastos Pereira
Professor auxiliar da Universidade de Aveiro

Prof.ª Dr.ª Gabriela Tamara Vincze
Professora auxiliar convidada da Universidade de Aveiro (Orientadora)

agradecimentos

First of all, I would like to express the sincere gratitude to my supervisor Prof. Gabriela Tamara Vincze for her guidance, encouraging and enthusiastic support during all these years.

I wish to express gratefulness to Prof. José Joaquin de Almeida Grácio who received me so well at University of Aveiro and provided me with an immense sense of motivation on research works. It was with great sadness that we learn of his death. He was always very constructive and had very good ideas for new initiatives.

A special thank goes to Prof. Fréderic Barlat for his valuable comments, motivating discussion and the writing assistance for the publications.

I truthfully thank to Prof. António Manuel de Bastos Pereira for his kindness and technical support through the duration of this research.

I would like to express my thanks to Prof. Abel Dias dos Santos for the help of hydraulic bulge tests and the maching of grip pieces used for improved simple shear test device.

I am grateful to Prof. Myoung-Gyu Lee of Korea University for providing user-material subroutine code of the HAH model.

I would like to thank to Prof. Ricardo José Alves de Sousa for his help on the sheet grid pattern marking used in DIC techniques.

Senior technician Msc. António Festas is acknowleged, especailly for the machining of the samples and the experimental tools, technician Msc. Ricardo Beja for the technical assistance of the testing equipments, and Msc. José Sousa for the help of mechanical tests.

I also thank to my colleagues and friends from TEMA for their fellowship.

This is a great opportunity to express my thanks to all the members of the jury who reviewed this dissertation and gave helpful comments.

The financial support from FEDER funds through the Operational Program for Competitiveness Factors - COMPETE and National Funds through the FCT - Foundation for Science and Technology of Portugal under the project (PTDC/EMS-TEC/0777/2012) and the grant (SFRH/BD/103010/2014) is acknowledged. Some works on tube bending were supported by the industrial project cooperated with Portuguese company CICLO-FAPRIL: Optimization of forming conditions of the plastic deformation of aluminium alloy (2013).

Finally, I wish to express my love and gratitude to my beloved family. Without their endless encouragement and assistance, I would not have finished this dissertation.

palavras-chave

Retorno elástico torsional, aços dual-phase (DP), liga de alumínio, embutidura, dobragem de tubos, modelos constitutivos anisotrópicos

resumo

Este trabalho é dedicado à investigação dos mecanismos / fontes de retorno elástico torsional em estruturas automóveis leves e à identificação de formas de controlar este problema.

Em primeiro lugar, para garantir uma correta modelação do retorno elástico torsional, foram utlizados os resultados de vários ensaios do material, incluindo diferentes solicitações de carga/descarga, assim como a utilização de modelos constitutivos adequados. O comportamento mecânico dos materiais submetidos a trajetórias simples e complexas de carga é descrito utilizando leis de encruamento e critérios de plasticidade anisotrópicos.

Foi desenvolvido um novo dispositivo de ensaios de corte para os aços DP para realização de ensaios de inversão de carga. Foram realizados testes cíclicos de carga-descarga-carga de tração uniaxial e biaxial assim como testes de dobragem em três pontos em material pré -deformado com vista à determinação da degradação do módulo de elasticidade com o aumento de deformação plástica. O efeito da trajetória de deformação na determinação do valor inicial do módulo de elasticidade e a sua degradação foram registados e analisados.

Em segundo lugar, foram selecionados como casos de estudo dois processos clássicos de deformação plástica de metais, nomeadamente embutidura de chapas de aço DP e dobragem por matriz rotativa de tubos de alumínio de parede fina e secção assimétrica, devido ao seu evidente efeito de retorno elástico torsional. Foi proposta uma definição melhorada de retorno elástico torsional baseada nos eixos principais de inércia da secção transversal. A relação entre o momento de torção e ângulo de torção foi introduzida para explicar a ocorrência de retorno elástico torsional. Para melhorar a robustez dos modelos numéricos, foram realizadas várias técnicas de modelação, incluindo a identificação de coeficiente de atrito, a restrição de acoplamento da superfície para mandril flexível utilizando um elemento conector articulado, e a correlação de imagens digitais. O mecanismo de retorno elástico torsional foi analisado tendo em conta a evolução de estado plano de tensão e a trajetória de deformação nos componentes após a enformação por deformação plástica.

Em terceiro lugar, foi analisada e discutida a sensibilidade dos modelos constitutivos de materiais no que diz respeito à precisão da previsão do retorno elástico torsional. Além disso, foi investigada a influência dos parâmetros do processo de embutidura profunda (direção de material, “blank-piercing” e lubrificação) e dos parâmetros numéricos do processo de dobragem de tubos (restrição dos limites do mandril flexível e atrito nas zonas de contacto) no retorno elástico torsional.

Finalmente, foram propostas duas estratégias de controlo para o processo de embutidura profunda, com base no raio da curvatura da matriz variável e na posição dos freios, para reduzir o retorno elástico torsional de duas peças “C-channel” e “P-channel”, respetivamente. No caso de dobragem de tubos, o controlo do retorno elástico torsional foi alcançado pela otimização da função do mandril e inclusão de um assistente de impulso de carga. Estas estratégias de controlo, baseadas em FEA, apresentam-se como métodos alternativos para a redução do momento torsor e do retorno elástico torsional em termos de aplicações específicas.

keywords

Twist springback, dual-phase steels, aluminium alloy, deep drawing, rotary draw tube bending, anisotropic constitutive models

abstract

This work is devoted to the investigation of the mechanism/source of twist springback in lightweight automotive structures and to the identification of ways to control this problem.

Firstly, to ensure accurate twist springback modelling, a reliable test data of material behaviours under various loading /unloading conditions as well as appropriate constitutive models are necessary. The anisotropic yield criteria and hardening models were adopted to characterize the material behaviours under monotonic and complex strain paths.

An enhanced simple shear device was developed to obtain the stress-strain behaviour under reversal loading of DP steels. Uniaxial and biaxial loading-unloading-loading cycle tests and the proposed three-point bend test with pre-strained sheets, were conducted to determine the elastic modulus degradation with the increase of plastic strain. A significant effect of the loading strategy on the determination of the initial and the degradation of elastic modulus was observed and discussed.

Secondly, two typical metal forming processes, namely deep drawing of DP steel sheets and mandrel rotary draw bending of asymmetric thin-walled aluminium alloy tube, were selected as case studies due to their evident twist springback. A more reasonable definition of twist springback with respect to the principal inertia axes of the cross-sections was proposed. The relationship between torsion moment and twist angle was introduced to explain the occurrence of twist springback. Several key modelling techniques including the friction coefficient identification, surface-based coupling constraint for flexible mandrel using HINGE connector element and digital image correlation were performed for improving the robustness of the numerical models. The mechanism of twist springback was analysed from the evolution of in-plane stress and deformation history in the components after forming.

Thirdly, the sensitivities of material constitutive models to the accuracy of twist springback prediction were analysed and discussed. The influence of deep drawing process parameters (material direction, blank piercing and lubrication) and numerical parameters of tube bending (boundary constraint for flexible mandrel and interfacial friction) on twist springback are provided.

Finally, two control strategies for deep drawing process, based on variable die radius and partial draw bead design, were proposed to reduce the twist springback of the C-channel and the P-channel, respectively. In case of tube bending, the control of twist springback was reached by the optimization of mandrel nose placement and inclusion of push assistant loading. These FEA-based control strategies appear to be alternative methods to reduce the unbalance torsion moment and the twist springback in terms of particular case.

Table of Contents

List of Figures

List of Tables

Symbols and Abbreviations

A	cross sectional area
A_E	the enclosed area defined by the wall midline
a	material coefficient associated to the crystal structure
φ	global twist angle
$d\varphi$	relative twist angle
σ	true stress
ε	true strain
ε_t^B	thickness strain under biaxial loading
θ	bending angle
θ_e^s	extrados sidewall opening angle
θ_i^s	intrados sidewall opening angle
θ_e^f	flange tip angle on the extrados side
θ_i^f	flange tip angle on the intrados side
δ	elongation
δ_r	ratio of torsion moment
δ_w	wiper die rake angle
ϕ	yield function
ω	bending angular velocity
Φ	homogeneous, asymmetric yield function
$\hat{\mathbf{h}}^{\mathbf{s}}$	microstructure deviator
$\mathbf{i}$	the principal axis of inertia for the cross-section before springback
$\mathbf{j}$	the principal axis of inertia for the cross-section after springback
ρ	density
υ	Poisson' ratio
E_0	initial elastic modulus
E_a	the chord modulus obtained for a large plastic pre-strain
E_{chord}	unloading elastic modulus by chord model
E_0^U	the initial elastic modulus under uniaxial tension
E_0^B	the initial elastic modulus under biaxial tension
E_0^T	the initial elastic modulus under TPB
E_a^U	the saturated value of the chord modulus under uniaxial loading
E_a^B	the saturated value of the chord modulus under biaxial loading

E_a^T	the saturated value of the chord modulus under TPB
E_{equi}^B	the equivalent elastic modulus under biaxial loading
E_L	the elastic modulus in the longitudinal plane
F_x	axial force along the x-direction
F_y	axial force along the x-direction
G_T	the shear modulus in the transverse plane
I_p	the inertia moment of the section after pre-straining
W_p	the average width of pre-strained specimen
t_p	the average thickness of pre-strained specimen
R_e	the radius of the extrados sidewall curl
R_i	the radius of the intrados sidewall curl
J	torsion constant
T	torsion moment
$\langle \varepsilon^* \rangle$	virtual strain
$\langle u^* \rangle$	virtual displacement
$\{f\}$	equivalent nodal force
q	shear flow
μ	Coulomb friction coefficient
P(f)	the moment magnitude of the frictional tangential tractions
M_N	the friction-producing normal moment
M_C	contact moment for predefined friction
ζ	the decrease rate of elastic modulus
V_p	Speed of pressure die
V_m	Speed of mandrel retracting

AA	aluminium alloy
AHSS	advanced high strength steels
ANOVA	analysis of variable
AOI	area of interest
AUV	autonomous underwater vehicle
BHF	blank-holder force
BLUL	biaxial loading-unloading-loading cycle test
CC	comprehensive compensation
CCD	central composite design
CFT	curved-flanging test

COF	coefficient of friction on interface
C-channel	curved channel
CMM	coordinate-measuring machine
CNC	computer numerical control
DA	displacement adjustment
DCA	discrete curvature adjustment
DD	diagonal direction or 45º to rolling direction
DIC	digital image correlation technique
DP	dual-phase steel
FDM	force descriptor method
FEM	finite element model
FEA	finite element analysis
HAH	homogeneous anisotropic hardening
IA	inverse approach
IH	isotropic hardening
IHKH	combined isotropic and kinematic hardening model
MNP	mandrel nose placement
MRDB	mandrel rotary draw bending
NIP	number of integration points
PTFE	polytetrafluoro- ethylene
PAL	push assistant loading
P-channel	P-shaped variable cross-sectional channel
PVW	the principle of virtual work
QPE	Quasi-Plastic-Elastic
R3D4	4-node 3-D bilinear quadrilateral discrete rigid elements
RD	rolling direction
RSM	response surface methodology
S11	tangential stress
S22	circumferential or transverse stress
S4R	quadrilateral shell elements with reduced integration
SD	standard deviation
SDA	smooth displacement adjustment
SRDD	stroke returning deep drawing
SS	simple shear
TCT	twist compression test
TD	transverse direction
TPB	three-point bending test
TPB-P	three-point bending with pre-strained sheet

TRIP	transformation induced plasticity
ULUL	uniaxial loading-unloading-loading cycle test
UMAT	user material subroutine by implicit time integration
VUMAT	user material subroutine by explicit time integration
UR3	the rotation about Z-direction or 3-direction of numerical element
2D	two-dimensional
3D	three-dimensional

Chapter 1

Introduction

1.1 Motivation and objectives

Due to weight reduction efforts to meet fuel economy pressure and increase vehicle safety requirements, the use of advanced high strength steels (AHSS) and aluminium alloy (AA) is gaining popularity for almost every vehicle maker for their promising higher strength without compromising ductility. For example, recently, Cadillac will use an advanced mixed-material approach for the lightweight body structure of the upcoming CT6 range-topping full-size sedan, as shown in Figure 1-1. Advanced high strength steels are used for sound deadening and body structure reinforcing. Aluminium extrusions with multi-void hollows are utilized for the rocker and engine cradle assemblies. This mixed material approach saves 90 kg weight compared to a predominately steel construction.

Source: www.aec.org

Figure 1-1 Cadillac CT6 mixed material lightweight structure.

However, several undesirable phenomena are observed during the forming of such materials, which compromise the quality of the formed part. Springback is one of the most significant drawbacks encountered in various metal forming processes. The shape deviation caused by springback always results in quality defects and difficulties during the assembly of components. It is of vital importance to improve the springback prediction accuracy and control strategies in industrial practices.

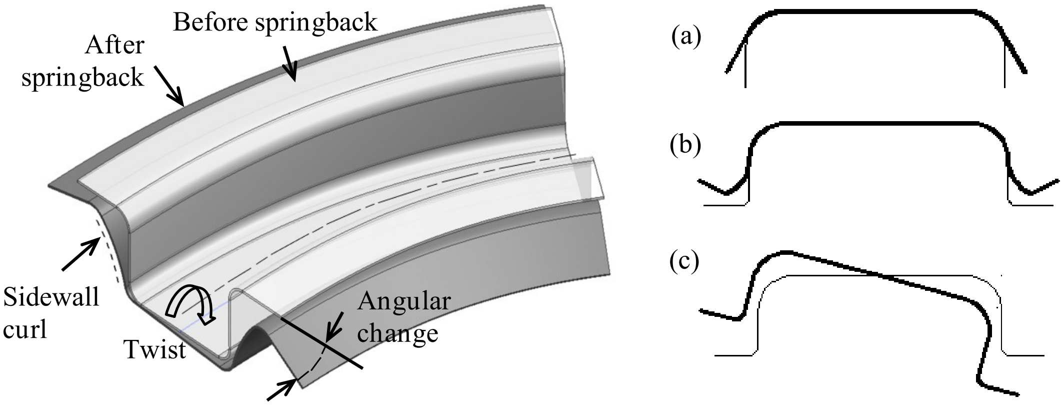

Figure 1-2 Schematic of three springback modes: (a) angular change; (b) sidewall curl; (c) twist (the bold line is the shape after springback and the light line is the design intent).

There are three common modes of springback, i.e. angular change, sidewall curl and twist, as described in Figure 1-2. In practice, twist is the most complex springback behaviour compared to other two modes due to its nonlinear global dimensional distortion. The corresponding forming processes always involve nonlinear large strain and complex strain path changes when the sheet or tube is subjected simultaneously to a combination of bending, unbending, stretching and torsion. Although many techniques have been developed to control and compensate for springback of automotive panels in the past, it is still a tough task when encountering the twist problem. At present, the significant twist springback typically observed in lightweight automotive structures with complex cross-sectional shape (e.g., Figure 1-3) has become a serious issue and needs to be conquered urgently.

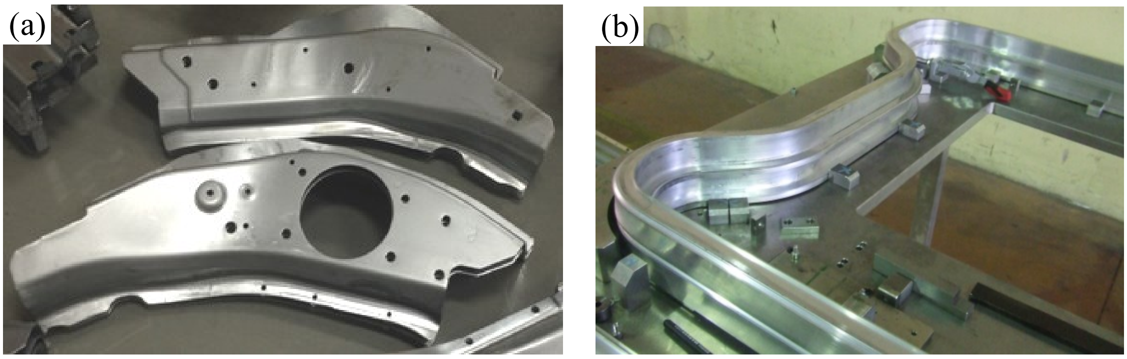

Figure 1-3 lightweight automotive structures with complex cross-sectional shape: (a) Industrial channel–shaped rails made by AHSS (b) thin-walled tube made by AA.

In order to meet the requirements for reduced environmental impact, advanced high strength steel sheets and aluminium alloy tubes have become a favourite resource for the weight reduction of automotive structures. However, twist springback inevitably occurs when the load is released due to asymmetric load and the elastic property of material. This leads to geometrical inaccuracy of parts and causes difficulty at the following assembly stage. The twist springback is more serious when advanced high strength steels and aluminium alloys are involved due to their high ratio of yield strength to elastic modulus. Effective methods of predicting and control of twist springback in metal forming processes are vital in precision manufacturing.

The main goal of this work is to gain a deeper understanding of the mechanics/source of twist springback for lightweight automotive structures and to identify ways to control this problem. This objective involves experiments, constitutive modelling and applications to answer to the following questions:

i. How to develop accurate modelling of complex twist springback behaviour? How the material models and process parameters affect the accuracy of twist springback prediction?

ii. What is the fundamental mechanism of twist occurring during the unloading process? Which is the best way to evaluate this behaviour from the source of twist?

iii. What are the important factors affecting the twist springback in metal forming processes? How do these factors affect twist springback?

iv. Is there any efficient strategy to control twist springback of complex products?

1.2 Thesis organization

The dissertation is organized in eight main chapters. The description of each chapter is as follows:

- In *Chapter 1,* a brief motivation and objectives on twist springback in lightweight automotive structures are given. The reading outline and the list of publications in the scope of this dissertation are also provided.
- In Chapter 2, a literature review including elastoplastic constitutive models, springback prediction, springback control and historic twist springback

investigation is presented.

- In *Chapter 3,* several experimental methodologies are introduced and used to characterize the studied materials. The theoretical descriptions of the adopted anisotropic constitutive models are presented as well as the introduction of apparent elastic modulus degradation.
- In *Chapter 4*, the material parameters of the adopted constitutive models are identified. The determination of nonlinear elastic behaviour of DP steels and its loading strategy dependency are described.
- In *Chapter 5*, two metal forming processes, i.e., deep drawing of DP steel sheet and mandrel rotary drawing tube bending, are introduced due to their evident twist springback characteristics. Some key modelling techniques are presented to improve the prediction accuracy of the models. The theoretical analyses of the occurrence of twist springback are performed as well as the development of the corresponding experimental and numerical models.
- In *Chapter 6*, the sensitivities of material constitutive models to the accuracy of twist springback prediction are analysed and discussed. The influence of some deep drawing process and numerical parameters of tube bending on twist springback are also provided.
- In *Chapter 7*, in order to reduce or eliminate the twist springback, some FEA-based control strategies are assessed in terms of individual forming case. Variable die radius and partial draw bead design are proposed to minimize the twist springback of the C-channel and the P-channel, respectively. Two process control strategies related to the mandrel nose placement and the push assistant loading are also evaluated for the efficient reduction of twist springback of asymmetric thin-walled tube.
- In *Chapter 8*, the closure is given along with final conclusions and future works of research.

1.3 List of publications in the scope of this dissertation

This dissertation includes some original papers that have been previously published or submitted for publications, as follows:

Submitted/in preparation

1) **Xin Xue,** Juan. Liao, Gabriela. Vincze, António B. Pereira, Frederic Barlat. Experimental assessment of nonlinear elastic behaviour of dual-phase steels and application to springback prediction. International Journal of Mechanical Sciences, 2016, under review.

2) Juan Liao, **Xin Xue**, Myoung-Gyu Lee, Frédéric Barlat, Gabriela Vincze, António B. Pereira. Constitutive modelling for path-dependent behaviour and its influence on twist springback in channel forming. International Journal of Plasticity, 2016, to be submitted in July.

Papers in international scientific periodicals with referees:

1) Juan Liao, Jose Sousa, Augusto B. Lopes, **Xin Xue**, Frederic Barlat, António B. Pereira. 2016. Mechanical, microstructural behavior and modeling of dual phase steels under complex deformation paths, International Journal of Plasticity, in press. doi:10.1016/j.ijplas.2016.03.010

2) **X. Xue,** J. Liao, G. Vincze, J. A. Sousa, F. Barlat, J. Gracio. 2016. Modelling and sensitivity analysis of twist springback in deep drawing of dual phase steel. Materials & Design 90, pp204-217. doi:10.1016/j.matdes.2015.10.127

3) **X. Xue,** J. Liao, G. Vincze, F. Barlat. 2015. Twist springback characteristics of dual-phase steel sheet after non-symmetric deep drawing. International Journal of Material forming. doi: 10.1007/s12289-015-1275-2.

4) **X. Xue,** J. Liao, G. Vincze, J. Gracio, 2015. Modelling of mandrel rotary draw bending for accurate twist springback prediction of an asymmetric thin-walled tube. Journal of Materials Processing Technology 216, pp405-417. doi:10.1016/j.jmatprotec.2014.10.007

5) Juan Liao, **Xin Xue**, Myoung-Gyu Lee, Frederic Barlat, Jose Gracio, 2014. On twist

springback prediction of asymmetric tube in rotary draw bending with different constitutive models. International Journal of Mechanical Sciences 89, 311-322. doi:10.1016/j.ijmecsci.2014.09.016

6) J. Liao, **X. Xue**, C. Zhou, J. J. Gracio, F. Barlat, 2014. A semi-analytic model to predict and compensate springback in the 3D stretch bending process. Steel Research International 85(4), 697-709. doi: 10.1002/srin.201300216
7) Juan Liao, **Xin Xue**, Chi Zhou, Frederic Barlat and Jose Gracio. 2013. A springback compensation strategy and applications to bending cases. Steel Research International, V84 (5): pp463-472. doi: 10.1002/srin.201200220

Papers in conference proceedings:

1) **Xin Xue,** Juan Liao, Gabriela Vincze, Jose J Gracio. Optimization of an Asymmetric Thin-walled Tube in Rotary Draw Bending Process. The 9th International Conference and Workshop on Numerical Simulation of 3D Sheet Metal Forming Processes (NUMISHEET 2014). Melbourne, Australia. Jan.6-10. AIP Conference Proceeding, 1567: 1111-1116. doi: 10.1063/1.4850165
2) **X. Xue**, J. Liao, G. Vincze, J. Gracio, Twist springback of asymmetric thin-walled tube in mandrel rotary draw bending process. The 11th International Conference on Technology of Plasticity (ICTP2014), 19-24 October 2014, Nagoya, Japan. Procedia Engineering, v81, 2014, 2177-2183. doi:10.1016/j.proeng.2014.10.305
3) **Xin Xue,** Juan Liao, Gabriela Vincze, Frédéric Barlat. Twist springback characteristics in C-rail of dual-phase steel sheet after deep drawing. Proceeding of International Deep Drawing Research Group 2015(IDDRG2015), Shanghai, China, 31st May-3rd June, pp511-521.
4) **Xin Xue**, Juan Liao, Gabriela Vincze. Benchmark report: Strain Prediction Benchmark – Cross Die (DC05). Forming Technology Forum 2015 (FTF2015), Benchmark report, June29-30th, 2015, Zurich, Switzerland.
5) Juan Liao, **Xue Xin**. Experimental investigation of deep drawing of C-rail benchmark using various lubricants., MATEC Web of Conferences, v21, 2015, 04011, The 4th International Conference on New Forming Technology (ICNFT2015), Aug. 6-9th.

Glasgow, Scotland, UK. DOI：doi.org/10.1051/matecconf/20152104011.

6) **Xin Xue**, Juan Liao and Gabriela Vincze. Assessment of anisotropic yield criterion for strain prediction in non-axisymmetric deep drawing of dual-phase steel. International Conference of Advanced High Strength Steel and Press Hardening (ICHSU2015), Changsha, October 15-18, 2015. http://dx.doi.org/10.1142/9789813140622_0061

7) **Xin Xue**, Juan Liao, Gabriela Vincze, António B. Pereira. Control strategy of twist springback for an asymmetric thin-walled tube subjected to rotary draw bending. First International Conference and Workshop on Mechanical Engineering Research (RTME2016), 11-13th July 2016, Aveiro, Portugal.

Chapter 2

Literature review

2.1 Elastoplastic constitutive models

The springback phenomenon, occurring in connection to metal forming processes, is mainly a stress-driven problem. When a work piece is removed from tools, the residual stresses after forming are released, and give rise to an additional deformation. This leads to the decrease of the geometrical accuracy of products and makes more difficult the assembly stage. The magnitude of the springback is roughly proportional to the ratio between the residual stress and Young's modulus (Eggertsen and Mattiasson, 2009). The phenomenon is particularly troublesome for high strength steels (high residual stresses) and aluminium (low elastic modulus). However, these are the types of materials that have found an increasing use in the automotive industry, in order to improve crash performance and reduce weight.

The magnitude of the residual stresses depends on a large number of material and process parameters. In simulations of metal forming processes, the same input parameters as true process influence the predicted residual stresses. However, besides these physical parameters, a number of deficiencies of the numerical model also influence the result. Especially, the quality of the material modelling has a great impact on the accuracy of the predicted residual stresses. A phenomenological model of plastic deformation is made up of several components, such as yield condition, strain hardening law, and the model for the degradation of elastic stiffness due to plastic straining. Those metal products that contribute most to the global springback have generally undergone one or more bending, unbending, stretching and torsion. Therefore, it is important to consider the complex loading path behaviours for accurate springback prediction.

Over the years, some yield functions have been introduced to describe the initial plastic anisotropy of metals. A detail review of the anisotropic yield criterion development can be found in (Banabic et al., 2010; Mattiasson et al., 2008; Vrh et al., 2014). The most commonly used yield criterion is still Hill's anisotropic quadratic yield function (Hill'48). The relative simplicity of this model makes it attractive to use, and is the reason for its numerical efficiency. But, the Hill'48 criterion is often criticized for its application to metals with low r-values (Laurent et al., 2009). Another widely used yield function is Yld2000-2d (Barlat et al., 2003), which are based on two linear stress transformations. Several works have showed that it has a satisfactory correlation with the experimental data for aluminium (Luo et al., 2012; Guner et al., 2012).

Besides the yield loci, FE springback prediction is also strongly dependent on work-hardening model, especially on how the model describes the material's mechanical behaviour under a strain-path change, such as the stress reversal occurring during the bending to unbending transition process (Oliveira et al., 2007; Lee et al., 2012a; Lee et al., 2013). Yoshida and Uemori (2003) showed the hardening law should be able to consider some phenomena, e.g., the Bauschinger effect, the transient behaviour, permanent softening, and work-hardening stagnation (See Figure 2-1; and Boger et al., 2006). The Bauschinger effect is characterized by early re-yielding of the material during reverse loading. The transient behaviour is a smooth, elastic–plastic transition with a rapid change of the work hardening rate. After the transient period, a stress offset occurs for some materials, namely permanent softening. Furthermore, for some mild steels abnormal shapes of the reverse stress–strain occurs due to work-hardening stagnation.

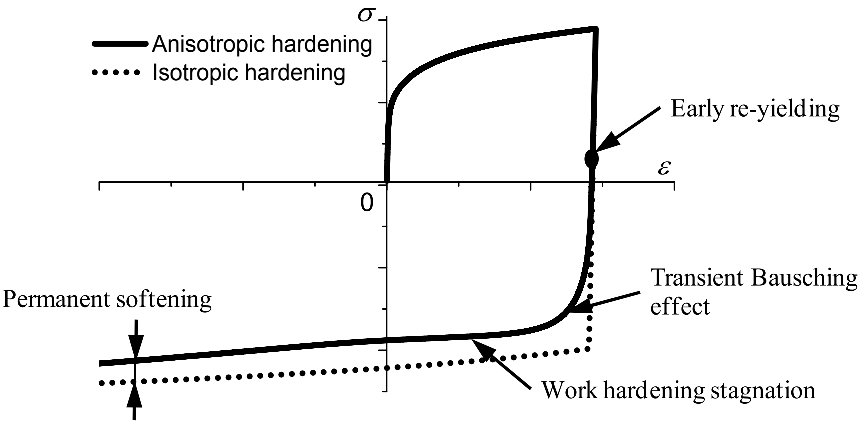

Figure 2-1 Schematic unloading curves to illustrate the Bauschinger effect, the transient behaviour, the permanent softening, and the work hardening stagnation (Yoshida, 2003).

Several phenomenological material models have been proposed to describe the evolution of the yield surface when the material undergoes plastic deformation. The simplest assumption is that of isotropic hardening, which means that the initial yield surface expands radially in the stress space during plastic deformation. This assumption is reasonably effective when the material undergoes monotonous and proportional loading. However, with this assumption none of the effects demonstrated in Figure 2-1 are taken into consideration. To include these effects, kinematic hardening has to be added, i.e. the translation of the yield surface. For the kinematic hardening, two main approaches can be identified: one is based on the shifting of a single yield surface, and the other one involves multiple yield surfaces. The first approach is based on linear kinematic hardening models proposed by Prager (1956) and Ziegler (1959), both of which can describe the Bauschinger effect. A combination of linear kinematic hardening and isotropic hardening, that better predicts the Bauschinger effect, is proposed by Hodge (1957). To account for the transient behaviour, several models have been proposed. Armstrong and Frederick (1966) and Chaboche (1986) introduced an additional term to Prager's kinematic hardening model in order to capture the transient behaviour. The second approach focuses on multiple yield surfaces. Mroz (1967) proposed a model with several yield surfaces, in which piecewise linear hardening is defined. To describe a smooth nonlinear curve, an infinite number of yield surfaces are necessary. In order to avoid the difficulties associated with a large number of yield surfaces, Dafalias and Popov (1976) proposed a model based on two yield surfaces that can represent realistic smooth hardening with continuously varying plastic modulus. Armstrong–Frederick and Chaboche models can be considered as two-surface models, with one yield surface and one bounding surface, where the bounding surface defines the limiting state of stress. For the permanent softening, several modifications of the Armstrong–Frederick and Chaboche models have been proposed, in which the bounding surface evolves kinematically (Bower 1989; Geng and Wagoner, 2000; Chun et al., 2002), or where the bounding surface can undergo both kinematic and isotropic evolution (Yoshida and Uemori, 2002 and 2003). Among other hardening models based on two surface schemes, the Yoshida–Uemori (Y–U) model is gaining popularity in part because it has relatively few parameters to be determined and it has been implemented into the commercial FE software Pam-Stamp (ESI/PSI, 1995). It assumes kinematic hardening of the loading surface and combined isotropic-kinematic hardening for the bounding surface, with both surfaces based on Hill's yield function (Hill, 1948). Recently, Ghaei et al. (2010) propose an implicit stress integration algorithm for Y–U model for ABAQUS code and apply it to a channel draw springback of DP 600 steel sheet. Predicted springback angles using Y–U and Chaboche-type hardening models are in good agreement with experiments, although the accuracy is enhanced by taking into account reduced elastic modulus.

Kinematic hardening models, whether involving one or two yield surfaces, still invoke the translation and expansion of a fixed surface shape, thus preserving the direction of normal at given locations. A new approach presented by Barlat et al. (2011) describes the smooth change of yield surface shape by homogenous yield function-based anisotropic hardening (HAH). The homogeneous yield function consists of a stable component associated with a general anisotropic yield function and a fluctuating component which distorts the overall shape of the yield surface. The yield surface shape is flattened opposite from the active stress state during the proportional loading, but this fluctuating component does not affect the shape of the yield surface near the active stress state. The HAH approach leads identical plastic flow stress response to the isotropic hardening for the monotonous loading, but the Bauschinger effect and transient hardening behaviour can be efficiently reproduced by the appropriate control of fluctuating component during continuous and reverse loading. In this regard, the HAH model is similar to the combined isotropic-kinematic hardening, but does not involve the translation of the yield surface. Although other approaches have been introduced and applied to the forming and springback simulations (Teodosiu, 1998; Haddadi,2006; Holmedal, 2008; Thuillier, 2010; Kim,2012)), these models usually require many parameters. For example, the model by Teodosiu and Hu (1998) has 13 parameters to describe the evolutions of state variables including fourth- and second-order tensors. Recently, the HAH model was successfully extended to describe more complex material behaviour during strain path change such as cross-loading (Barlat et al., 2012). With 8 hardening parameters, the extended model could predict measured stress-strain responses of an EDDQ or DP steel sheet sample during various two-step tension tests. Especially, the flow stress overshooting and transient hardening behaviour (a lower yield stress followed by a rapid change of strain hardening) for cross-loading conditions could be captured reasonably.

During unloading of the material, i.e. removal of the forming tools, the amount of springback depends to a great extent on the elastic stiffness of the material. In classic plasticity theory, the unloading of a material after plastic deformation is assumed to be linearly elastic with the stiffness equal to a constant modulus. However, several experimental investigations in the literature have revealed that this is an incorrect assumption. The degradation of the elastic unloading modulus with an increase of the plastic strain has a considerable effect on springback predictions, especially for AHSS (Cleveland and Ghosh, 2002; Chatti, 2011 and 2014; Zhan et al., 2014; Ghaei et al., 2015; Komgrit et al., 2016). The unloading elastic modulus was reported to decrease up to 30%

for mild steel (Yoshida et al., 2002), 20% for high strength steels (Yang et al., 2004) and 10% for aluminium (Yoshida et al., 2002) at a moderate plastic strain. In particularly, for uniaxial tension, Hassan et al. (2015) found that the decrease of elastic moduli for DP600 and DP1000 were 28% and 26%, respectively. More recently Mendiguren et al. (2015) observed that the drop of the chord modulus for TRIP700 was about 15-20% after 12% plastic deformation.

Many researchers attempted to interpret the source of elastic modulus change with the increase of plastic strain by means of microscopic observations and elasto-plastic analyses. Yang et al. (2004) reported that this phenomenon is due to the mobile dislocations accompanying the pile-ups near to the grain boundaries. The dislocations nucleated during pre-strain move along the slip plane and pile-up easily, while the front of dislocations can be stopped by obstacles, e.g., grain boundaries or solutes. The release of the shear stresses acting on the slip systems during unloading can induce a backward motion of the dislocation pile-ups. The density of these mobile dislocations increases with plastic strain, thereby causing an apparent decrease of the elastic modulus as the plastic pre-strain increases. Kim et al. (2013) stated that the rate of increase of mobile dislocations is relatively high at small pre-strains but low after large pre-strain. Pavlina et al. (2015a) studied the nonlinear unloading behaviour of three different commercial DP780 steels and found that the elastic modulus degradation is greater as the strength ratio between martensite and ferrite increases. It should be noted that this controversial conclusion need further investigation by using more types of DP steels. They also indicated that active strain hardening mechanisms (e.g., TRIP and TWIP effects) affect the unloading behaviour of AHSS (Pavlina, 2015b). Mendiguren et al. (2015) presented that the decrease of the unloading elastic modulus might be related to phase transformation but mainly to dislocation rearrangement. Vrh et al. (2011) experimentally observed that a significantly greater drop in the unloading elastic modulus takes place when sheet metal is pre-strained in the perpendicular direction. This evidence indicates that in some cold-rolled sheet steels, the elastic modulus degradation is strongly strain path dependent.

In the past decade, some researchers have already taken into account the nonlinear elastic behaviour for material constitutive description of elasto-plasticity. Yoshida et al. (2002) proposed an exponential representation of the change of elastic modulus. Similarly, Yu (2009) introduced a polynomial expression of the elastic modulus variation with plastic pre-strain of TRIP steels. Chatti (2013) developed a coupled damage-elasto-plasticity approach based on Yoshida model, which allows the prediction of the elastic modulus evolution starting from a virgin material and finishing at the fracture stage. These models are known collectively as elastic chord modulus. However, the elastic unloading curve after a prescribed pre-strain normally falls below the reloading curve to form a hysteresis loop. This complex stress-strain relationship is ignored in all chord models mentioned above. In order to describe the complex hysteresis loop, Sun and Wagoner (2011) proposed the Quasi-Plastic-Elastic (QPE) model, in which a new type of strain called QPE strain was introduced. The strain is recovered similar to elastic strain and dissipates energy similar to plastic strain. This model was later combined with a homogeneous anisotropic hardening model by Lee et al. (2013) to simultaneously capture the complex unloading and plastic flow behaviours. Böhlke and Bertram (2003) used a phenomenological model for the evolution of the texture-dependent effective elastic properties to predict the corresponding saturation values of polycrystalline copper. The works of Vladimirov and Reese (2010, 2012) contributed to a material constitutive framework of finite strain elasto-plasticity with evolving elastic and plastic anisotropy and combined hardening. The evolution of elastic anisotropy was represented by representing the Helmholtz free energy as a function of a family of evolving structure tensors.

As mentioned above, various constitutive models have been proposed to describe the material behaviour more accurately. However, the coefficients of the above anisotropic constitutive functions commonly need to be optimized explicitly or iteratively from experimental tests. In addition, the majority of commercial finite element codes are not equipped with state of the art constitutive models. For instance, the commercial finite element code (Abaqus, 2011) still lacks a strong non-quadratic anisotropic yield model. Even more, only the classical model of Chaboche is the most advanced built-in hardening model in this software package. The implementation of advanced material models has been completed by other team members. In this work, one of main goals will focus on the applications of advanced constitutive models for improved springback prediction in metal forming processes.

2.2 Springback prediction

Generally, two methods are used for prediction of springback: analytical methods and numerical methods. Both types of methods have been extensively employed by researchers and industrial engineers.

Several analytical solutions have been proposed for prediction of springback. Zhang and Hu (1998) used incremental plasticity theory to analyse the bending process with a large bending curvature. They also attempted to observe the deformation history in order to obtain an accurate calculation of stress distributions. (Tang, 2000) showed the applicability of plastic-deformation theory in calculating stress distributions, the deviation of the neutral axis and the bending moment, which is needed for springback analysis. Buranathiti and Cao (2004) performed an analytical springback prediction of a straight flanging process by calculating the bending moment under plane-strain conditions. They used the model to predict springback for a few parts and compare the predicted results with experimental data. Yi et al. (2008) developed an analytical model based on differential strains after relief from the maximum bending stress for six different deformation patterns. They used each deformation pattern to estimate springback by the residual differential strains between outer and inner surfaces after elastic recovery. Zhang (2007) also developed an analytical model to predict springback in sheets bent in a U-die under plane-strain conditions. They used Hill’s 1948 yield function and took into account the effects of deformation history, the evolution of sheet thickness and the shifting of the neutral surface. Lee et al. (2009) proposed an analytical model for asymmetric elastic–plastic bending under tension followed by elastic unloading. They also compared the calculated springback amounts with the results of physical measurements and showed that their model predicted the main trends of the springback in magnesium alloy sheets reasonably well considering the simplicity of the analytical approach.

Although the use of analytical models is advantageous because of their simplicity, the application of these models is limited to simple geometries. The amount of springback also depends upon many process variables such as friction, temperature, variations in the thickness and mechanical properties of the metal material. Moreover, complex strain histories and highly nonlinear deformation of the material during the forming process increase the difficulty of springback prediction. Therefore, the most widely used method of predicting springback is to carry out computer simulations that rely on advanced material models to compute the stress distribution in the part and the final geometry of the part after elastic unloading. Most researchers have used the finite element method to predict springback.

Finite element (FE) simulation of springback is very sensitive to numerical parameters such as element type, mesh size as well as to the constitutive model that governs the behaviour of the deformable part. Several investigations have been conducted to study the effect of numerical parameters on the accuracy of the predicted profile after springback. Lee et al. (1998) determined the order of significance of each numerical parameter relative to its effect on the prediction of springback angle and radius of curvature. The results of their study show that the mesh size has the strongest effect on the accuracy of springback prediction. Li et al. (2002) simulated the draw-bend test and studied the sensitivity of the simulated springback to numerical parameters. They showed that for small R/t ratios, nonlinear 3D solid elements are required for an accurate prediction of springback. Wagoner and Li (2007) later performed an analytical study of the bending under tension followed by springback. They also performed a numerical analysis of this problem and calculated the relative error as a function of number of integration points (NIP). Larger NIP can always reproduce a continuous stress distribution, and therefore the post-forming bending moment, more accurately, but at the expense of increased computational time (Wagoner et al., 2013). Burchitz and Meinders (2008) developed an adaptive through-thickness integration method which showed negligible difference for NIP larger than 20–25. Zhao et al. (2009) elaborated a three-dimensional elastic-plastic finite element model of rotary draw tube bending process using ABAQUS/Explicit code. The improved model having higher accuracy and computational efficiency of springback prediction was developed by Zhu et al (2012). Li et al (2012) attempted to obtain tube ‘size effect’ related bending behaviours and geometry-dependent springback behaviours.

The coupling effects of the material properties such as Young’s modulus, yield stress, strain hardening exponent and normal anisotropic coefficient on the springback angle were addressed by Jiang et al. (2010). They confirmed that the bending angle, yield stress, and hardening coefficient have positive effects on the springback angle, and Young’s modulus, the hardening exponent, and the thickness anisotropy exponent had negative effects. They also pointed out that the Young’s modulus and the strain hardening coefficient had the greatest influence on the springback of a TA18 tube. Oliveira et al. (2007) investigated the influence of the work-hardening models on springback, and showed that the differences in springback prediction of the NUMISHEET'93 benchmark U-shape channel were not significantly higher than those reported in previous studies. Using the same forming case with different hardening laws, Eggertsen and Mattiason (2010) presented that the degradation in elastic stiffness is probably the constitutive factor that has a greater impact on the predicted springback than that of the hardening law. Kim et al. (2011) studied the effects of a variable elastic modulus on springback predictions in stamping AHSS using a flexible set-up including U-bending, flanging and S-rail stamping tests. They recommended accuracy description of the nonlinear hardening and elastic modulus change as material input data for reliable simulations, particularly for springback prediction of complex part geometry. Nevertheless, so far, the nonlinear elastic behaviour has been ignored in most industrial forming applications, i.e., the elastic modulus has usually been assumed constant. Zhu et al (2013) used the isotropic-hardening, the mixed-hardening models and the Yoshida–Uemori model for springback prediction of thin-walled tube bending, and found out the Yoshida–Uemori model is more suitable than the other two models, especially for large deformation. The HAH model (Barlat et al., 2011) was successfully implemented in a finite element (FE) code (Lee et al., 2012a) and simulations were conducted to predict springback in U-draw bending. The results were found to be in good agreement with the experiments (Lee et al., 2012b).

It is also worth mentioning that some researchers have used a combination of an analytical method and the finite element method to predict springback. These methods usually endeavour to use the advantages of each approach. Zhan et al. (2006) developed a method based on springback angle model derived using an analytical method and simulation results from three-dimensional (3D) rigid-plastic finite element method (FEM). Lee et al. (2007) proposed a simplified numerical procedure to predict springback in a 2D draw bend test that was developed based on a hybrid method which superposes bending effects onto membrane element formulation. This approach was shown to be especially useful to analyse the effects of various process and material parameters on springback.

2.3 Springback control

Springback generally refers to the undesirable part shape change that occurs upon removal of constraints after forming. It consists in dimensional and angular changes that happen during unloading due to the occurrence of primarily elastic recovery in the part. In many cases, the shape deviation caused by springback always brings on quality defects and difficulties during the assembly of components. For the past decades, a lot of work has been carried out to solve this problem. These approaches can be categorized into two types. The first approach is to minimize springback by increasing the plastic deformation and hence reducing the difference of stresses along the sheet thickness. In sheet metal forming, most of them attempt to reduce springback by increasing the tension in the sheet. This can be achieved by increasing the blank holder force, especially at the end of the forming stage or by using draw beads (Hishida and Wagoner, 1993; Cao, 2000; Huang, 2005). In general, a larger tension in the sidewall reduces the stress gradient through the sheet thickness causing less springback. However, the maximum tension in the sheet is limited by the fracture strength of the sheet material. Moreover this stretch forming technique is generally not sufficient to eliminate springback. Some studies also suggest the use of a variable blank holder force during the punch trajectory. In this method, the blank holder force is low from the beginning until almost the end of the forming process and then it is increased at end of the process such that a large tensile stress is applied to the sheet material (Liu et al., 2002). This approach can also be achieved by increasing the restraining forces and providing tensile preloading or post-loading on the deformed part, as conducted by Sunseri et al (1996). The above mentioned approaches do not require the adjustment of the tool shape. However, although high performances for the control systems and devices are requested, they can be not easy to eliminate springback completely.

The second type of approaches is to compensate for springback at die design stage, i.e. regardless of what the springback might be, the die is designed in a way that the final part shape after springback corresponds to the target part shape Some approaches using finite element (FE) simulations with an iterative scheme were proposed. Karafillis and Boyce (1996) developed the ‘‘force descriptor method (FDM),’’ in which a new tool shape is obtained by imposing the sheet with the reversed internal force at the end of the forming stage. However, its application suffers from lack of convergence unless the forming operation is symmetric or has very limited geometric change during springback, and the result is a little conservative. Gan and Wagoner (2004) proposed a displacement adjustment (DA) method, in which the tool shape is adjusted according to the displacement deviation between the unloaded part and the desired one. Other modified DA methods such as "Smooth Displacement Adjustment (SDA)" proposed by Lingbeek et al. (2005) and "Comprehensive Compensation method (CC)" proposed by Yang and Ruan (2011) were developed to improve the accuracy of DA method. These approaches are generally used since they conduct the whole ‘‘trial and error’’ procedures using software but not with physical die sets. However, because most of the compensation methods are based on pure geometrical reversal adjustments, several iterations are required to obtain the right tool shape even for a simple bending case, as verified by Cheng et al. (2007) and Lingbeek et al (2008). Therefore, a significant amount of time is still needed for the FE simulation to complete the iterative process design. Additionally, the compensation results are sensitive to the accuracy of the FE calculations and the errors accumulate rapidly during the iterations (Lingbeek et al., 2005). Lingbeek et al. (2006) reported that 20% inaccuracy of the FE analysis results in 30% error in springback compensation and only 56% final efficiency of the procedure. Therefore, obtaining a desired tool shape for industrial products by FE iterations is still hard task.

Because of the complexity of the springback phenomenon, several trial-and-error iterations are still inevitable to ensure the dimension and shape accuracy of products. In parallel, the development of non-contact 3D measuring technology has provided an on-the-shop-floor method to accurately and fast measure of the shapes of trial stamped parts, as referred by Garcia et al (2002). This information has been widely used for tool design during the trial process because all the different areas where distortion occurs can be quantitatively identified, as stated by Boesemann (2000) and Damoulis (2010). However, the measured displacement deviations cannot be directly used to modify the tool shape. Although some analytic methods for tool design are applicable, such as the work conducted by Xue et al. (1999) and Zhang et al. (2007). However, these models are limited for simple specific problems: Cylinder or U/V bending. Recently, Liao et al. (2013) proposed a discrete curvature adjustment (DCA) strategy based on the plastic bending theory, in which springback calculation and reconstruction of the tool shape are based on curvature. Since any section curve can be described by its curvature along its arc length, this method can be generally applied for both symmetric and asymmetric channel parts with arbitrary profiles. An asymmetric U-shaped part, an industrial blade and a cylindrical part are applied to verify their compensation method. Compared with DA approach, a more accurate tool shapes were obtained after first iteration.

The accuracy of springback prediction is critical to the die face compensation. To obtain a reliable springback prediction, attention should be paid to the factors discussed. Although the springback prediction can only reach 70-80% accuracy for most of automotive parts (Xu et al., 2005), the optimization of forming conditions and tool design based on the FEA prediction can significantly reduce the geometrical deviation induced by springback and help increase the application of aluminium and AHSS in automotive industry.

2.4 Twist springback

The origin of unbalanced elastic deformation and residual stresses which produce the twist springback in metal forming processes can be attributed to many parameters. Here a classification similar to that proposed by Wijskamp (2005) is introduced. Figure 2-2 shows a diagram with the 'input' variables material, geometry and process, and the 'output' residual stress and twist springback on the other. The two branches indicate the origin of stress factors that are present during metal forming and match with the intrinsic and extrinsic classes of stress, respectively. Intrinsic sources relate to material anisotropy, whereas extrinsic sources are mainly process related, including asymmetric geometry, non-linear contact and different loading path response.

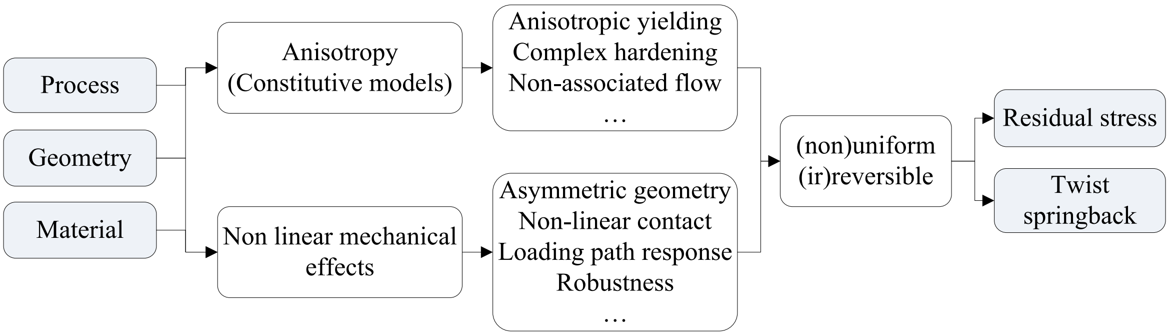

Figure 2-2 Diagram showing the origin of residual stress and twist springback in metal forming processes.

Recently, there has been growing interest in twist springback in metal sheet or tube forming processes. Kim et al. (2000) proposed a one-dimensional theory for the analysis of thin-walled curved rectangular box beams subjected to torsion and out-of-plane bending. A higher-order one-dimensional analysis of the in-plane flexural deformation of thin-walled curved box beams is carried out by Kim et al (2002). The main contribution of their work is to consider an additional degree of freedom accounting for the in-plane distortional deformation of the thin-walled cross section that is accompanied by the in-plane bending deformation. Their works mainly emphasise the mechanics of solids rather than plastic deformation and metal forming process conditions. An analytical generalized expression relating angle of twist to twisting moment and residual angle of twist per unit length for rectangular strips under plastic torsion was obtained by Dwivedi et al. (2002). The resulting formula had been shown to be in good agreement with experimental data for mild steel strips. A comparison between the results obtained for bars of non-linear and linear work-hardening materials loaded under torsion was also made by them. Gangwar et al. (2011) used isotropic hardening described by the modified Ludwik stress-strain, and applied the maximum shear stress theory of failure to determine the stress components at the elastic plastic interface. Being different to twist springback in the occurrence of many metal forming processes, the extrinsic parameter of torsion loading was provided as known condition by Dwivedi et al. (1992 and 2002) and Gangwar et al (2011). In sheet metal stamping, Iyama et al. (2003) attempted to explore the mechanism of occurrence of twist springback in a curved channel sheet. They also investigated the influences of the factors resulting in twist springback such as blank holding force and cushion force. A new evaluation method and compensation method for twist springback of channel-shape sheet model was presented by Ito et al. (2007). Stresses obtained by the FEA were used to calculate the bending moment distribution over the mid surface of the sheet. The shape after springback was predicted by the mechanical relation, which describes the elastic springback deformation process without springback process simulation. Using the Iyama's geometric model, twist torque around the longitudinal axis using the stress distributions from FE simulation could be obtained by Takamura et al. (2011). Through the investigation of twist torque and its transition during the drawing and die removal processes, they found that the negative torque generated by side wall opening occurring in the die removal process was the dominant factor in positive twist. A stroke returning deep drawing (SRDD) method was proposed to control twist springback by Geka et al. (2013). Their results showed twist springback can be reduced by optimising the conditions for two-step SRDD. Higher requirements of equipment and tool conditions such as the hydraulic servo press machine, flexible blank holding force, and multi-action tools are needed. Xu et al. (2005) studied the effect of draw bead on the springback for a HSS automotive part. Their benchmark results showed there was no split and wrinkles without using draw beads along the sides of the panel, but severe twisting occurred and the trimmed panel deviated from the nominal shape by 20 mm. After draw beads were added, especially along the sides at the twisting location, the twisting springback disappeared and the maximum deviation of the trimmed panel was within 1 mm. Lee et al. (2005) numerically studied the twist springback of the double S-rail stamping sheets based on isotropic–kinematic hardening laws and non-quadratic anisotropic yield functions. They then conducted the influences of blank holding force, lubrication and material direction on twist springback by means of simulation and experiments. Simplified one-dimensional plane strain analytical and numerical methods were also developed to better understand the twist springback in forming processes. Li et al. (2012) carried out a parametric study on the twist springback of an industrial rail component made of advanced high strength steels. The effects of work piece design and forming process parameters were conducted through FE analysis and a try-out experiment. Fedorov (2012) investigated the bend-twist coupling effect in composite wind turbine blade structure through experimental and numerical methods. The study emphasizesd the twist springback measurement of an autonomous underwater vehicle (AUV) propeller blade manufactured using cold forging process by Abdullah et al. (2013). Pham et al. (2014) investigated the influence of the blank alignment relative to the tools on twisting magnitude. Their results showed that the change in the section of the sample, specifically the misalignment of the ultra-thin metallic sheet sample with respect to the tools is the main factor that gives rise to twisting. For some samples, aligned or not, twisting is caused by sliding (asymmetric flow of side walls) of one of the two ends of the sample during the draw bending process.

Hence, the above efforts provide insight into how twist springback can be modelled and controlled by means of theoretical analysis, numerical study and process optimisation. The possible links between twist springback prediction and nonlinear parameters such as anisotropic constitutive model, numerical parameter, asymmetric geometry and process condition should be in-depth analysed and discussed as well as the control strategy based on accurate simulation model.

Chapter 3

Material characterization and constitutive modelling

3.1 Materials

3.1.1 Advanced high strength steels (DP steels)

The use of advanced high strength steels (AHSS) is gaining popularity for almost every vehicle maker for their promising higher strength without compromising ductility. However, high strength steels result in large elastic recovery (also called springback) after forming, which hinders their wider application. Pertinent to springback, AHSS, and in particular dual-phase (DP) steels, have several aspects that make them distinct from traditional mild and high strength/low alloy steels:

- Strength-to-modulus ratios similar to aluminium alloys.
- High strain hardening concurrent with high strength.
- Very large plastic work products and thus high temperatures developed during deformation.
- Very large non-isotropic hardening effects after path reversals.
- Very large ‘‘modulus’’ changes when unloading after large plastic strains.

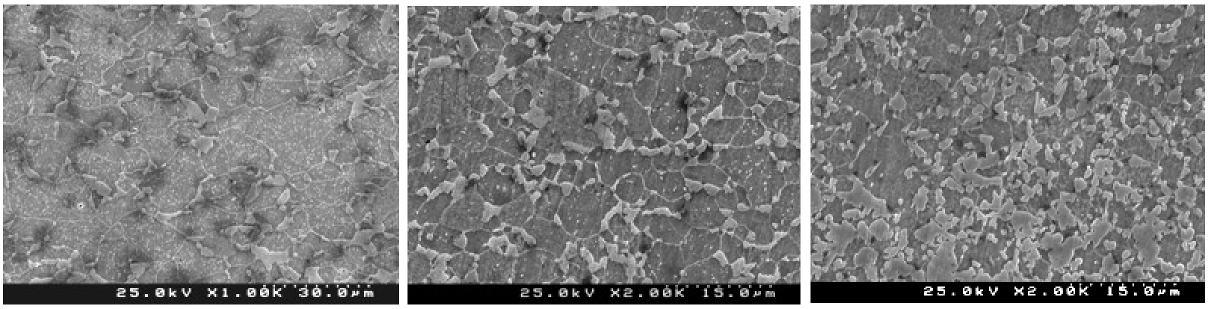

(a) 14% martennsite, D=22μm (b) 21% martennsite, D=10μm (c) 37% martennsite, D=6μm

Figure 3-1 SEM images of the microstructure: (a) DP500 (b) DP600 and (c) DP780.

In this work, three grades of DP steels with the same thickness (0.8 mm) were considered: DP500, DP600 and DP780. The microstructures of these steels observed by SEM are shown in Figure 3-1. DP500 is characterized by the presence of martensite islands and a coarse-grained, 22 μm in average, ferrite phase. A more refined microstructure is observed for DP600 and DP780 in which the average ferrite grain size is 10 and 6 μm, respectively. The volume fraction of martensite in the three steels was measured to about 14%, 21% and

37%, respectively. The chemical composition for each material is listed in Table 3-1. It is of interest to note the addition of a small amount of Nb in DP600 and DP780. This micro-alloying element has a positive effect on production of a more homogeneous and finer grained DP microstructure, resulting in a higher strength and better ductility (Lee et al., 2012).

Table 3-1 Chemical composition of DP steels in weight percent

Steels	C	Mn	Si	P	S	N	Cr	Ni	Cu	Al	Nb	V	B
DP500	0.079	0.65	0.31	0.009	0.003	0.003	0.03	0.03	0.01	0.038	--	0.01	0.0003
DP600	0.089	0.85	0.2	0.014	0.004	0.004	0.03	0.03	0.01	0.049	0.016	0.01	0.0003
DP780	0.138	1.52	0.2	0.011	0.002	0.003	0.03	0.04	0.01	0.038	0.014	0.02	0.0002

3.1.2 Aluminium alloy (AA6060)

In automotive and aerospace industries, aluminium alloys have also been a popular and widely used material because of their relatively light weight and satisfactory strength properties (Esat, 2002). In the past decade, more than 80% of the manufactured extruded aluminium products are based on the AA6xxx series alloys due to its high extrudability (Cai et al., 2004). In particularly, aluminium alloy AA6060 heat treatable series alloys are the most widely used for the production of extruded thin-walled tubes in real applications. The strength of the alloy is dependent on many aspects such as the amount of Mg and Si in solid solution, and the size and distribution of Mg2Si precipitate particles. The chemical composition of AA6060 is provided in Table 3-2.

Table 3- 2 Chemical composition of AA6060 in weight percent [Cheng, 2010]

AA No.	Si	Fe	Cu	Mn	Mg	Zn	Cr	Ti
6060	0.3-0.6	0.1-0.3	0.1	0.1	0.35-0.6	0.15	0.05	0.1

3.2 Mechanical tests

Accurate description of the elastic-plastic behaviour of the material under various loading paths is vital for the industrial forming simulations. In this section, a series of mechanical tests including uniaxial tension, bulge, forward and reverse simple shear, in-plane biaxial and three-point bending with pre-strained sheet tests were conducted to characterize the material properties and identify the parameters in the elastic-plasticity models. The loading-unloading-reloading cycle tests under axial, biaxial and bending loading strategies were performed for the determination of elastic modulus degradation with the increase of plastic strain. The significant effect of loading strategy on the nonlinear elastic behaviour of dual-phase steels is observed and discussed.

3.2.1 Uniaxial tension

Standard uniaxial tensile tests were conducted with a SHIMADZU tensile testing machine (maximum capacity 100 kN). The specimens of DP steels were prepared according to the ASTM E8 standard. In order to determine the strain, a digital image correlation (DIC) system was employed to measure the displacement field. The ARAMIS-5M software was used to analyse the strains from optical images. In order to eliminate the region of inhomogeneous strain gradient, an appropriate area of interest (AOI: 45×10 mm) was selected, in which the deformation is almost uniform as shown in Figure 3-2. The tests were conducted at room temperature with a nominal initial strain rate of 10^{-3}/s. For each material, three tests were repeated to verify the reproducibility of the experimental results.

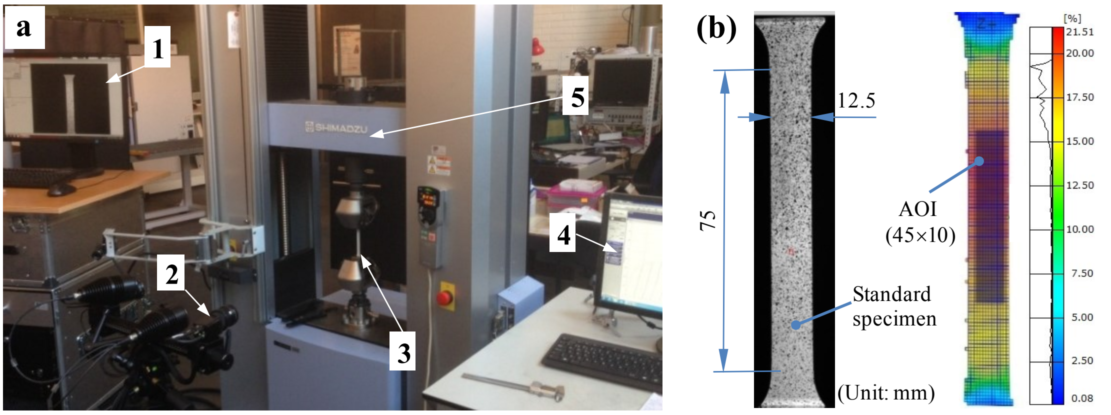

Figure 3-2 (a) Testing equipment: 1=ARAMIS-5M system, 2=DIC camera, 3=specimen, 4= TRAPEIUMX program, 5= universal tensile machine (b) DIC images of specimen and uniaxial deformation for DP steels.

In order to obtain the material anisotropic parameters, uniaxial tensile tests at the angles 0º, 45º and 90º with respect to the rolling or extruding direction would be performed. For the extruded thin-walled tube, the adopted specimen dimension is illustrated in Figure 3-3. To check the size effect of this sub-size tensile specimen on the test results, another tension tests are conducted on standard ASTM E8 specimens along the extrusion direction. The comparison results found that the difference between them is within 2%, which is acceptable for industrial application.

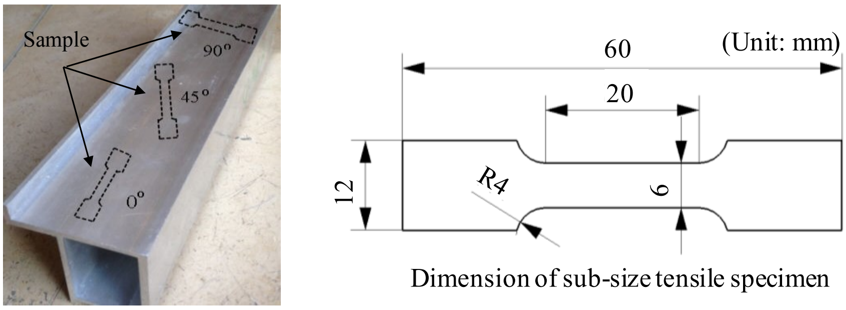

Dimension of sub-size tensile specimen

Figure 3-3 Uniaxial tensile specimen for aluminium alloy thin-walled tube.

The uniaxial loading-unloading-loading (ULUL) cycle tests were conducted for the DP steel analyses of the determination of elastic modulus degradation. It consists of five steps as shown: 1) continuous loading to prescribed pre-strain, 2) interruption by crosshead stop, 3) continuous unloading, 4) interruption to 'zero' stress, and 5) reloading-unloading up to failure. For instance, the true stress-strain curves of the ULUL cycle tests for DP780 are represented in Figure 3-4. It is observed that the cyclic tests are in good agreement with the corresponding monotonic tests, and that DP780 exhibits an obvious hysteresis loop after some pre-strain deformation.

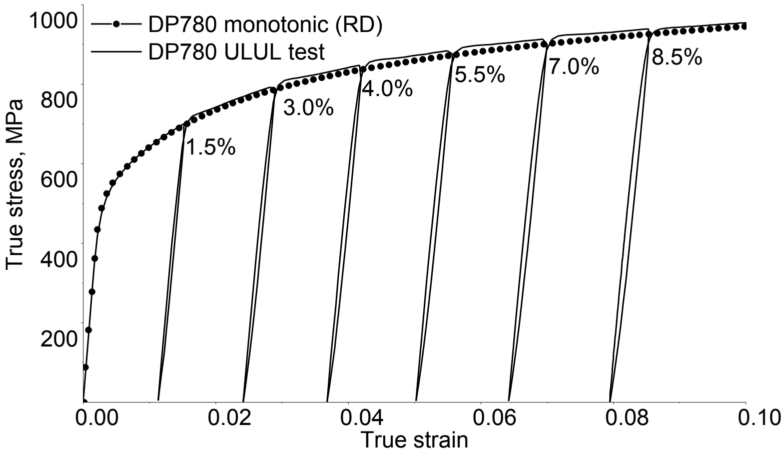

Figure 3-4 The true stress-strain curves of the ULUL cycle tests for DP780 steel.

3.2.2 Bulge test

The balanced biaxial bulge test allows the determination of the flow curve for a higher strain range compared with the uniaxial tensile test. Therefore, for a better mechanical characterization, this test was conducted in a hydraulic bulge test device for each of the three DP steels. The opening diameter of the circular die was 150 mm. Specimen with a diameter of 250 mm was bulged via the die opening, following the experimental procedures illustrated in Martins et al. (2013).

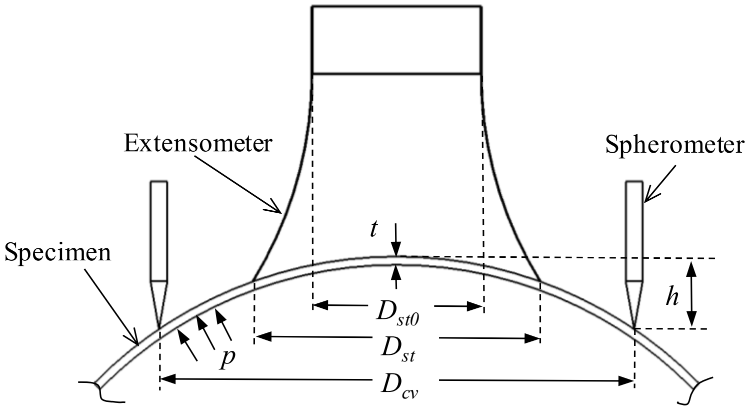

Figure 3-5 Variables used for evaluation of the stress and strain in bulge test.

The stress-strain data determination is based on analysis of measurable parameters and the membrane theory (Atkinson, 1997). Considering the equivalent bulge test, the flow stress can be determined by

$$\bar{\sigma} = \frac{p \cdot \rho}{2 \cdot t} \tag{3. 1}$$

where ρ is the corresponding radius of the curved surface at mid-thickness, p is the measured hydraulic pressure and t is the current sheet thickness at the top of the dome during testing, as shown in Figure 3-5. The curvature radius can be obtained by a simple geometrical construction as follow

$$\rho = \frac{(D_{cv}/2)^2 + h^2}{2 \cdot h} \tag{3. 2}$$

where D_{cv} is the spherometer diameter and h is the dome height, measured from tripod pins as shown in Figure . The current sheet thickness t can be calculated from initial sheet thickness t_0 and the current thickness strain ε_t, *as:*

$$t = t_0 \cdot \exp(-\varepsilon_t) \tag{3.3}$$

By evoking the assumption of material incompressibility, the sheet thickness strain ε_t is given by

$$\varepsilon_t = -(\varepsilon_1 + \varepsilon_2) = -2 \cdot \varepsilon = -2 \cdot \ln\left(\frac{D_{st}}{D_{st0}}\right) \text{ and } t = t_0 \cdot \left(\frac{D_{st0}}{D_{st}}\right)^2 \tag{3.4}$$

where ε_1 and ε_2 are the principal plastic strain components, ε the membrane strain, D_{st0} and D_{st} are the initial and current diameter of the measured circle respectively. From eq. (3.1),

$$\bar{\sigma} = \frac{p \cdot h}{16 \cdot t_0} \cdot \left[\left(\frac{D_{cv}}{h}\right)^2 + 4\right] \cdot \left(\frac{D_{st}}{D_{st0}}\right)^2 \tag{3.5}$$

Above expressions will be used for the calculation of the stress-strain curves presented.

3.2.3 Simple shear and Bauschinger tests

The planar simple shear (SS) test has proved to be a very efficient technique to evaluate the mechanical properties of flat samples (Rauch 1998). Especially, Bauschinger effect can be captured through direct and reverse shear tests. Many advantages offered by this technique were introduced by Vincze (2007) as well as the construction of the previous shear device. A rectangular shear sample is firmly clamped by the two grips, as shown in Figure 3-6a. One of grips is fixed while the other moves along the x-axis. The constant width *h* of the deformation area is maintained during the test. *L* and *Δx* are the current length of the specimen and the relative displacement of the two grips during simple shear deformation, respectively.

Compared to lower strength materials, the main challenge of SS test for high strength steels is to achieve a robust clamping. While a mechanical gripping approach only relying on friction was successful for soft materials such as aluminium alloy, the same method was insufficient in the preliminary trials for the steels with strengths of 600 MPa or higher. Therefore, one of the motivations of the present work was to develop an enhanced device for AHSS. As shown in Figure 3-6b and c, the entire specimen is encapsulated into the serrated groove with specially designed hatching knurling texture. This design of gripping system is able to well prevent the sample slipping. The depth of the groove is 0.6 mm, the length of the groove 35mm, the distance between the left and right grips 3.0 mm and the height of texture is 0.45mm. In order to prevent the rotational rigid motion of the global apparatus in the SS test, the improved shear apparatus with 4-guide structure was developed, as shown in Figure 3-7. The diameter of the guide pillar is 14mm. Note that there were only two guide pillars in the previous shear device.

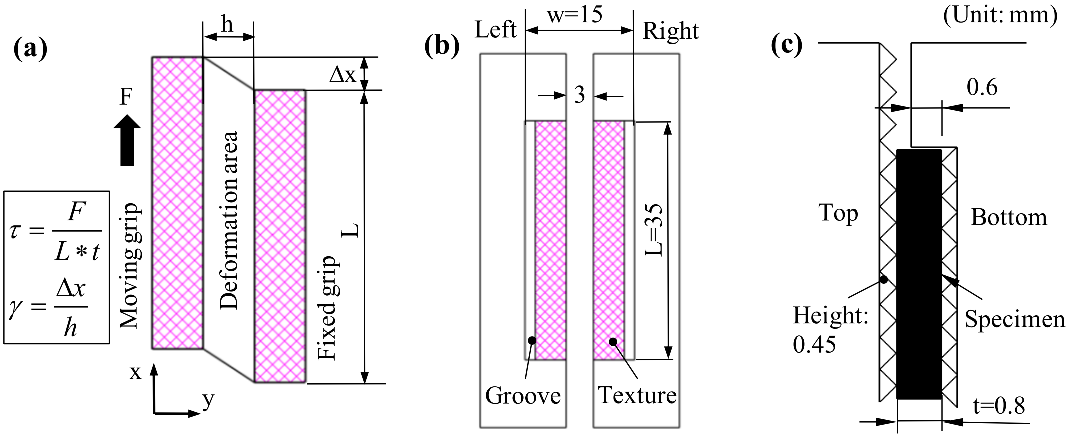

Figure 3-6 Schematic description of the SS test (b) grips with groove and texture design (front view) (c) side view after full clamping.

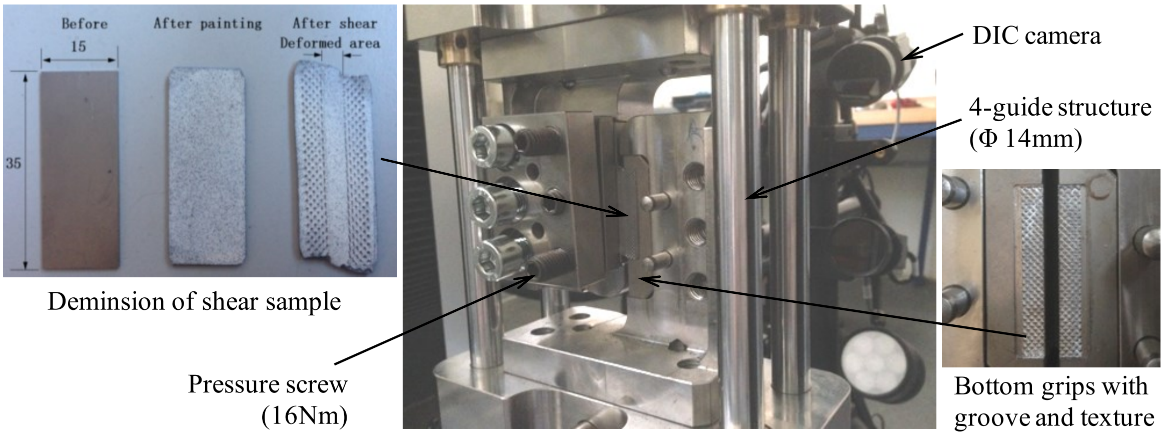

Figure 3-7 Improved shear device for AHSS shear tests.

The simple shear tests were conducted with the universal tensile testing machine SHIMADZU-AG-100kN to characterize the plastic behaviour of material upon reversal loading mode. Monotonic shear test and forward-reverse shear tests with different pre-strain were performed with a strain rate of 10^{-3} s^{-1}. Four samples were performed for each type of tests to check the consistency and one of them was used as representative. The dimension of the initial rectangular shear sample is 35x15x0.8 mm, which has been optimized to achieve a uniform shear strain in the centre area. The shear strain data was acquired via the digital image correlation (DIC) technique, namely the ARAMIS 5M. Due to the buckling impact in the both sides of the sample, only the data in the centre area were used for the strain calculation. An appropriate area of interest (AOI: 12.0 × 2.0 mm) was selected, in which the shear deformation is almost uniform (ranges from 25.5° to 26.5°) as shown in Figure 3-8.

Deformation area

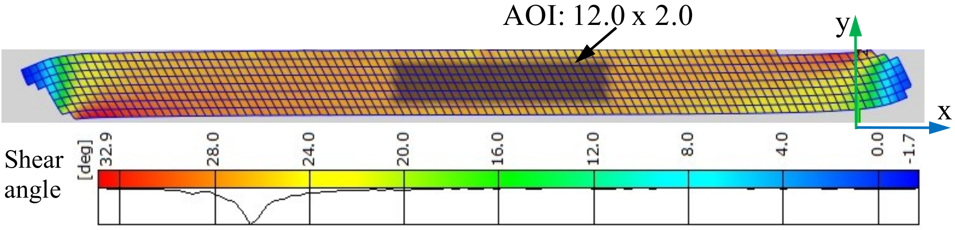

Figure 3-8 DIC images of shear deformation.

3.2.4 In-plane biaxial test with cruciform specimen

The real load state, particularly in a three-dimensional component forming, is characterized by multi-axial loads. Generally, a multi-axial stress state is approximately described with the aid of the uniaxial material parameters through an equivalent stress and strain hypothesis, which can be easily determined. However, it is not possible to exactly describe the material behaviour for all load cases with uniaxial parameters. Nevertheless, the in-plane biaxial stress state is one of special cases of multi-axial loading, which can realistically achieved using cruciform specimens and provide useful information for biaxial loading of a flat sheet.

In this work, biaxial loading-unloading-loading (BLUL) cycle test was employed to measure the elastic modulus degradation and study the effect of the loading strategy on the nonlinear elastic behaviour. Figure 3-9 shows the in-plane biaxial testing apparatus and the geometry of the cruciform specimen, which were originally designed and fabricated by

Kuwabara et al. (2002). The x and y-axes are in the rolling (RD) and transverse directions (TD) of the materials, respectively. Seven slits were fabricated in the arms of the specimens at intervals of 7.5 mm in order to attenuate the effect of the geometric constraint in the centre square gauge section. Uniaxial strain gauges (Tokyo Sokki Kenkyujo, YFLA-2-1L) were attached on the centrelines of specimen for the measurements of the normal strain components, ε_x and ε_y. The distance between each gauge and the specimen centre was 21mm, as shown in Figure 3-9b. The axial forces F_x and F_y were recorded from the load cell signals. The nominal stress ratio chosen for the biaxial tensile test was $\sigma_{Nx} : \sigma_{Ny} = 1:1$. The strain rates during unloading and reloading were $(0.2\text{-}1.5) \times 10^{-3}$/s.

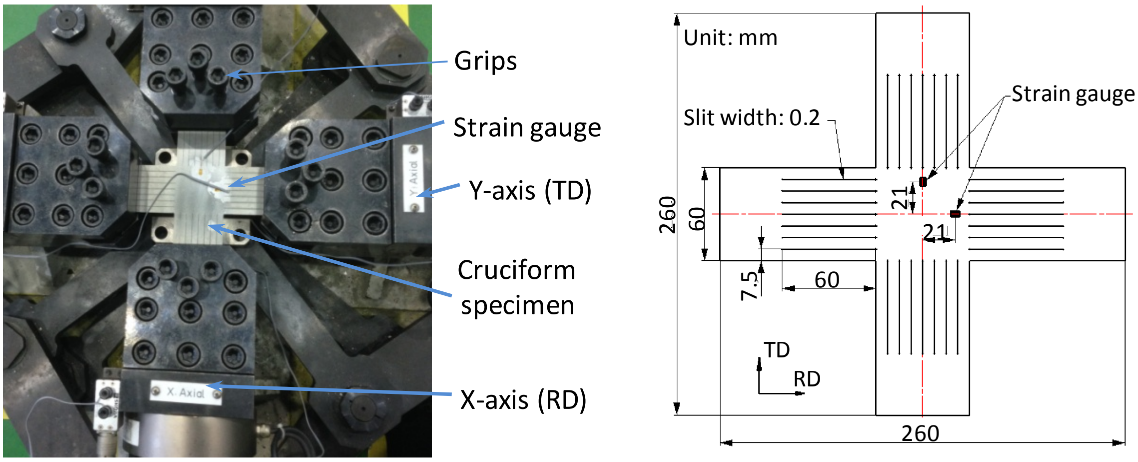

(a) (b)

Figure 3-9 (a) Experimental apparatus used for the in-plane biaxial tensile test (b) geometry of the cruciform specimen.

In this study, one cruciform specimen was used for a monotonic biaxial loading test and three for biaxial loading-unloading-loading (BLUL) cycle tests. At first in the BLUL test, the specimen was initially pre-strained up to a prescribed equivalent plastic strain and then unloaded. After confirming that axial forces F_x and F_y were back zero, the specimen was further deformed (second loading). The specimen was then unloaded and reloaded several times up to fracture. Figure 3-10 shows typical biaxial stress–strain curves of DP600 steel obtained from a BLUL test.

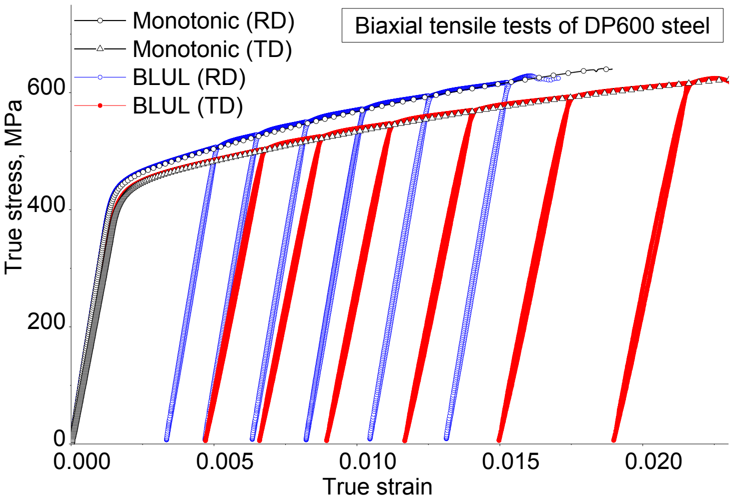

Figure 3-10 Typical biaxial stress–strain curves of DP600 steel obtained from a BLUL cycle test.

3.2.5 Three-point bending with pre-strained sheet

Compared to uniaxial or biaxial tensile tests, the three-point bending test is associated with bending moment and tension-compression state before unloading, which might be more suitable to capture the elastic properties in case of a three-dimensional problem (Alaoui, et al., 2008). Wang et al. (2012) and Zang et al. (2014) used three-point bending with pre-strained sheet to evaluate and verify the corresponding plastic hardening models considering more general loading path change. However, few studies have tended to ultimate this method for the determination of nonlinear elastic modulus degradation. Therefore, the three-point bending with several prescribed pre-strains was proposed to capture the degradation of elastic modulus with the increase of plastic strain. The test consists of four procedures as follow:

1) The initial elastic modulus was determined by means of the standard three-point bending test without pre-strain. More detailed description of the standard three-point bending is presented later in this section.

2) Similar to uniaxial tension, a large dog-bone shape specimen in the rolling direction was prepared and pre-strained up to a prescribed elongation δ, and then unloaded. Generally, this step is called pre-strain test.

3) A rectangular specimen was cut from the pre-strained sheet. The dimensions of large tensile and three-point bending specimens are presented in Figure 3-11.

4) The elastic moduli of the prescribed pre-strained sheets with different prescribed

plastic strains were measured by the standard three-point bending test.

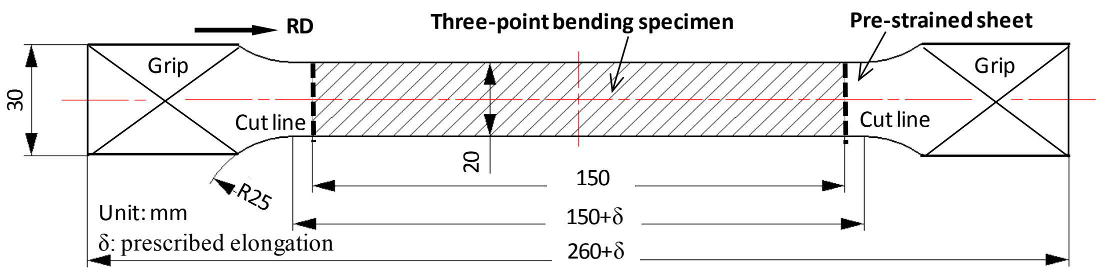

Figure 3-11 Dimensions of large uniaxial pre-strained sheet and subsequent three-point bending specimen.

In this work, the standard three-point bending test was conducted with the universal tensile testing machine SHIMADZU-AG-100kN. The device and dimensions of the three-point bending test are illustrated in Figure 3-12. A load force at middle span is applied by the displacement or stroke (S) of the pushrod with a deflection rate equal to 5.0 mm/min. The method has not only the advantages of simple specimen preparation and convenient loading device of the traditional three-point bending test, but also high precision in the static mode.

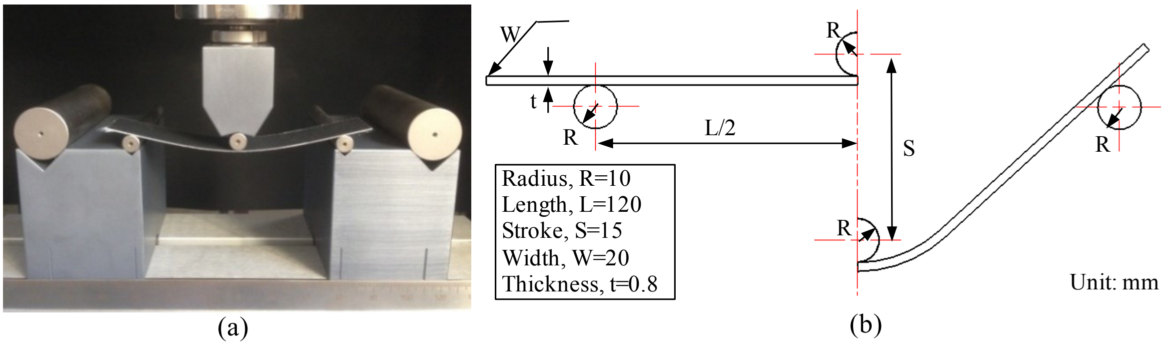

Figure 3-12 Standard three-point bending test: (a) device (b) dimensions.

3.3 Constitutive modelling

Current academic research in the area of constitutive modelling for various metals is focused on multi-scale modelling. The main idea is to use a homogenization scheme to correlate the mechanical behaviour observed at macroscopic scale with the microstructure evolution observed at microscopic scale. However, the computing time and the need of data storage for multi-scale models would be gigantic for practical problems. For forming simulations the use of macroscopic models is currently the only realistic alternative (Barlat et al., 2005). The subjects of material constitutive modelling mainly involve several issues such as nonlinear elastic behaviour, anisotropic yield criterion and hardening law. Each of these items requires a separate and careful consideration to improve accuracy and reliability of industrial metal forming simulations.

3.3.1 Apparent elastic modulus degradation-Yoshida chord model

The application of the QPE model, which can better capture the unloading stress-strain behaviour, is likely to achieve higher prediction accuracy but also more complex for twist springback prediction. Due to its high computing cost and added difficulty in its use, the QPE model is not convenient so far for real forming applications. In addition, the evolving elastic anisotropy of the used DP steels is not obvious by means of the experimental observation of ULUL results in different directions in Section 4.5.2. It means that the assumption of elastic isotropy is acceptable and makes less effect on the springback prediction. In this work, an analytical expression proposed by Yoshida et al. (2002) was used:

$$E_{chord} = E_0 - (E_0 - E_a)[1 - \exp(-\zeta \bar{\varepsilon}_p)] \tag{3. 6}$$

where E_{chord} denotes the unloading elastic modulus, E_a represents the chord modulus obtained for an infinitely large plastic pre-strain $\bar{\varepsilon}_p$ and ζ is a material parameter that determines the decrease rate of E_{chord}.

3.3.2 Anisotropic yield criteria

3.3.2.1 Hill 1948 yield criterion

von Mises is known as one of most commonly used yield criterion for isotropic materials. However, metallic sheets exhibit anisotropic behaviour developed during the rolling process. Hence, in 1948, Hill anisotropic yield criterion, which exhibits three orthogonal symmetry planes, was considered. The yield criterion is expressed by the quadratic function (Hill, 1948)

$$\phi = F(\sigma_{22} - \sigma_{33})^2 + G(\sigma_{33} - \sigma_{11})^2 + H(\sigma_{11} - \sigma_{22})^2 + 2L\sigma_{23}^2 + 2M\sigma_{31}^2 + 2N\sigma_{12}^2 = \bar{\sigma}^2 \tag{3. 7}$$

here ϕ is the yield function, *F*, *G*, *H*, *L*, *M* and *N* are constants specific to the anisotropy state of the material, and 1, 2, 3 refer to the principal anisotropic axes. For relatively thin-walled circular tubes, a state of plane stress is usually adequate. In terms of plane stress ($\sigma_{33} = \sigma_{31} = \sigma_{23} = 0$; $\sigma_{11} \neq 0$; $\sigma_{22} \neq 0$; $\sigma_{12} \neq 0$), the yield criterion becomes

$$(G+H)\sigma_{11}^2 - 2H\sigma_{11}\sigma_{22} + (H+F)\sigma_{22}^2 + 2N\sigma_{12}^2 = \bar{\sigma}^2 \tag{3.8}$$

where *F*, *G*, *H* and *N* are material coefficients which can be calibrated with normalized stresses or the r-values along different directions. Parameters *L* and *M* are fixed as 1.5.

3.3.2.2 Yld2000-2D yield criterion

The non-quadratic plane stress yield function Yld2000-2d is given by (Barlat et al., 2003)

$$\phi = \left[\frac{1}{2}\left(\left|\tilde{s}_1' - \tilde{s}_2'\right|^a + \left|2\tilde{s}_2'' + \tilde{s}_1''\right|^a + \left|2\tilde{s}_1'' + \tilde{s}_2''\right|^a\right)\right]^{1/a} \tag{3.9}$$

where *a* is a material coefficient associated to the crystal structure, $\tilde{s}_i'$ and $\tilde{s}_i''$ (i=1, 2) are the principal values of $\tilde{\mathbf{s}}' = \mathbf{L}'\boldsymbol{\sigma}$ and $\tilde{\mathbf{s}}'' = \mathbf{L}''\boldsymbol{\sigma}$, which are written in tensor notation with the stress deviator $\mathbf{s}$ and the stress tensor $\boldsymbol{\sigma}$. $\mathbf{L}'$ and $\mathbf{L}''$ contain a total of eight anisotropy coefficients α_k obtained by corresponding experiments.

$$\begin{gathered}
\left[\mathbf{L}'\right] = \begin{bmatrix} L_{11}' & L_{12}' & 0 \\ L_{21}' & L_{22}' & 0 \\ 0 & 0 & L_{66}' \end{bmatrix} = \frac{1}{3}\begin{bmatrix} 2\alpha_1 & \text{-}\alpha_1 & 0_1 \\ -\alpha_2 & 2\alpha_2 & 0 \\ 0 & 0 & 3\alpha_7 \end{bmatrix}, \\
\left[\mathbf{L}''\right] = \begin{bmatrix} L_{11}'' & L_{12}'' & 0 \\ L_{21}'' & L_{22}'' & 0 \\ 0 & 0 & L_{66}'' \end{bmatrix} = \frac{1}{9}\begin{bmatrix} 8\alpha_5 - 2\alpha_3 - 2\alpha_6 + 2\alpha_4 & 4\alpha_6 - 4\alpha_4 - 4\alpha_5 + \alpha_3 & 0 \\ 4\alpha_3 - 4\alpha_5 - 4\alpha_4 + \alpha_6 & 8\alpha_4 - 2\alpha_6 - 2\alpha_3 + 2\alpha_5 & 0 \\ 0 & 0 & 9\alpha_8 \end{bmatrix}
\end{gathered} \tag{3.10}$$

Eight input material data including the yield strength and r-value of the sheet in the rolling, transverse and diagonal directions and equi-biaxial stress state are required to identify these constants.

3.3.3 Anisotropic hardening models

3.3.3.1 Combined isotropic and kinematic hardening model

A yield surface of first-order homogeneous function is expressed as (Chung et al., 2005; Tang et al., 2010)

$$\phi(\boldsymbol{\sigma}-\boldsymbol{\alpha})-\bar{\sigma}_{iso}=0 \tag{3. 11}$$

Here, the back stress $\boldsymbol{\alpha}$ represents the translation of yield surface from the initial position, and the effective yield stress $\bar{\sigma}_{iso}$ measures the size of yield surface. The evolution of $\boldsymbol{\alpha}$ can be expressed by the non-linear kinematic hardening model:

$$d\boldsymbol{\alpha}=C\frac{d\bar{\varepsilon}^p}{\bar{\sigma}}(\boldsymbol{\sigma}-\boldsymbol{\alpha})-\gamma\boldsymbol{\alpha}d\bar{\varepsilon}^p \tag{3. 12}$$

where $\boldsymbol{\sigma}$ and $d\bar{\varepsilon}^p$ denote the Cauchy stress tensor and the equivalent plastic strain, $\bar{\sigma}$ is the effective stress and C and γ are material parameters. C, $\bar{\sigma}$ and γ determine the plastic hardening rate following an abrupt change of loading path.

During cyclic loading, there also exists the effect of isotropic hardening, e.g., the Swift law:

$$\bar{\sigma}=K(\varepsilon_0+\bar{\varepsilon}^p)^n \text{ with } \varepsilon_0=\left(\frac{\sigma_0}{K}\right)^{1/n} \tag{3. 13}$$

The material parameters *K, n* and ε_0 are evaluated from best approximation of a uniaxial or biaxial flow curve.

3.3.3.2 Homogeneous anisotropic hardening (HAH) model

A yield function is defined as a combination of a conventional yield function ϕ_s (isotropic or anisotropic) and a fluctuating component ϕ_f. A homogeneous, asymmetric yield function Φ is described by the following equation (Barlat et al., 2011)

$$\Phi(\mathbf{s})=\left(\phi_s^q+\phi_f^q\right)^{\frac{1}{q}}=\left[\phi_s^q+f_1^q\left|\hat{\mathbf{h}}^{\mathbf{s}}:\mathbf{s}+\left|\hat{\mathbf{h}}^{\mathbf{s}}:\mathbf{s}\right|\right|^q+f_2^q\left|\hat{\mathbf{h}}^{\mathbf{s}}:\mathbf{s}-\left|\hat{\mathbf{h}}^{\mathbf{s}}:\mathbf{s}\right|\right|^q\right]^{\frac{1}{q}}=\sigma(\bar{\varepsilon}) \tag{3. 14}$$

where q is a constant exponent. The tensor, $\hat{\mathbf{h}}^{\mathbf{s}}$ called the microstructure deviator, determines the direction of the yield surface distortion. $(\hat{\cdot})$ denotes a traceless normalized deviator to memorize the previous deformation history, e.g.,

$$\hat{\mathbf{h}}^{\mathrm{s}} = \frac{\mathbf{h}^{\mathrm{s}}}{\sqrt{\frac{8}{3}\mathbf{h}^{\mathrm{s}} : \mathbf{h}^{\mathrm{s}}}} \tag{3. 15}$$

f_1 and f_2 are two functions of the plastic state variables g_1 and g_2, defined by the relationship

$$f_k = \left(\frac{1}{g_k^q} - 1\right), \ k = 1, \ 2 \tag{3. 16}$$

At the first plastic increment, $\mathbf{h}^{\mathrm{s}}$ is initialized to the corresponding stress deviator $\mathbf{s}$ and kept constant as long as the loading direction is not changed. When the loading is changed so that $\mathbf{h}^{\mathrm{s}} \neq \mathbf{s}$, $\mathbf{h}^{\mathrm{s}}$ evolves as described below

If $\hat{\mathbf{h}}^{\mathrm{s}} : \mathbf{s} \geq 0$:

$$\frac{dg_1}{d\bar{\varepsilon}} = k_2\left(k_3 \frac{\bar{\sigma}_0}{\bar{\sigma}(\bar{\varepsilon})} - g_1\right) \tag{3. 17}$$

$$\frac{dg_2}{d\bar{\varepsilon}} = k_1 \frac{g_3 - g_2}{g_2} \tag{3. 18}$$

$$\frac{dg_4}{d\bar{\varepsilon}} = k_5\left(k_4 - g_4\right) \tag{3. 19}$$

$$\frac{d\hat{\mathbf{h}}^{\mathrm{s}}}{d\bar{\varepsilon}} = k\left(\hat{\mathbf{s}} - \frac{8}{3}\hat{\mathbf{h}}^{\mathrm{s}}(\hat{\mathbf{h}}^{\mathrm{s}} : \mathbf{s})\right) \tag{3. 20}$$

If $\hat{\mathbf{h}}^{\mathrm{s}} : \mathbf{s} < 0$:

$$\frac{dg_1}{d\bar{\varepsilon}} = k_1 \frac{g_4 - g_1}{g_1} \tag{3. 21}$$

$$\frac{dg_2}{d\bar{\varepsilon}} = k_2\left(k_3 \frac{\bar{\sigma}_0}{\bar{\sigma}_0(\bar{\varepsilon})} - g_2\right) \tag{3. 22}$$

$$\frac{dg_4}{d\bar{\varepsilon}} = k_5\left(k_4 - g_3\right) \tag{3. 23}$$

$$\frac{d\hat{\mathbf{h}}^s}{d\varepsilon} = k\left(-\hat{\mathbf{s}} + \frac{8}{3}\hat{\mathbf{h}}^s(\hat{\mathbf{h}}^s : \mathbf{s})\right) \tag{3. 24}$$

The constants *k and* $k_{1\text{–}5}$ are material coefficients. The variables g_3 and g_4 are introduced to represent the material behaviour in case of permanent softening, that is, when the flow stress after load reversal does not recover the level of the monotonic curve even after large strains. Note that these systems reduce to the case without permanent softening when k_4 or k_5 =0 and g_3=g_4=1.

3.4 Partial conclusion

In this Chapter, two widely used lightweight materials, DP steels and AA6060, were introduced. Several mechanical tests including uniaxial tension, forward-reverse shear, hydraulic bulge, in-plane biaxial test with cruciform specimen and the proposed three-point bending with pre-strained sheet tests were performed to accumulate sufficient material data for the identification of the constitutive parameters. The theoretical descriptions of the anisotropic yield criteria and hardening models were presented as well as the introduction of the apparent elastic modulus degradation.

Chapter 4

Identification of material parameters

4.1 Basic mechanical properties

4.1.1 DP steels

The uniaxial and bulge stress-strain curves for all the DP steels are depicted in Figure 4-1. The corresponding standard mechanical properties are summarized in Table 4-1. The strength of the steel increases with the grade of the DP steel, but the uniform elongation tends to decrease. The higher strength is ascribed to the larger volume fraction of hard martensite phase (Zhang et al., 2015). A simple way to explain the decrease of elongation for DP780 is, the plastic deformation is predominantly localized in the ferrite, while the martensite remains, in a first approximation plastically un-deformed (Bergström et al., 2010). Hence, the local strains in the ferrite are much larger than that recorded globally for the whole material in a conventional tension test.

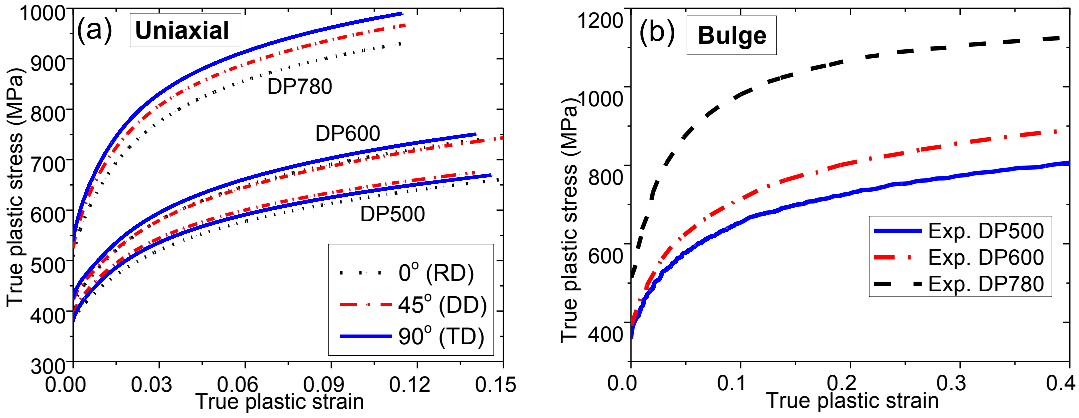

Figure 4-1 (a) Standard uniaxial tensile tests for DP steels at different directions (b) bulge tests.

Table 4- 1 Basic mechanical properties of the DP steels.

Material	Loading direction	Yield stress, $\sigma_{0.2}$ (MPa)	Tensile strength, σ_T (MPa)	Uniform elongation, e (%)
DP500	0°	390	660	15.2
	45°	409	674	14.3
	90°	398	669	14.8
DP600	0°	424	742	14.9
	45°	435	744	15.4
	90°	433	750	14.3
DP780	0°	535	932	12.0
	45°	555	967	11.9
	90°	572	990	11.8

Figure 4-1 also indicates that the flow stress anisotropy of DP780 is more prominent than that of DP500 or DP600. The strain anisotropy of the tensile specimens expressed by the R-value, defined as the ratio of the width-to-thickness strains for the different loading direction, is presented in Figure 4-2.

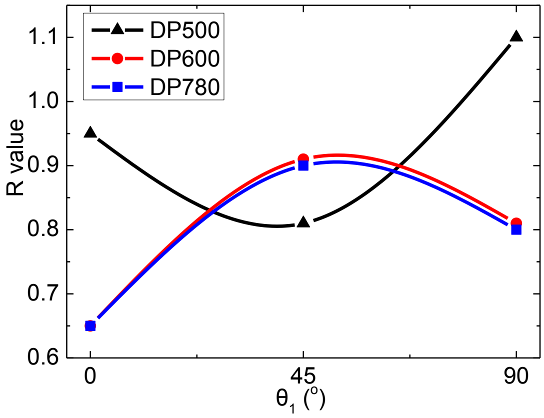

Figure 4-2 Plastic strain ratio (R) of DP500, DP600 and DP780 for tensile loading at different directions from RD.

4.1.2 AA6060-T4

The uniaxial true stress-strain curves along the 0°, 45°, 90° directions from the extrusion direction are plotted in Figure 4-3. It shows that the initial yield stress in the 45 degree directions is about 20% lower than that in the extrusion direction. The anisotropy of this material is obvious and should be taken into account in the material modelling. The material properties and anisotropic data of this material are listed in Table 4-2 and Table 4-3, respectively.

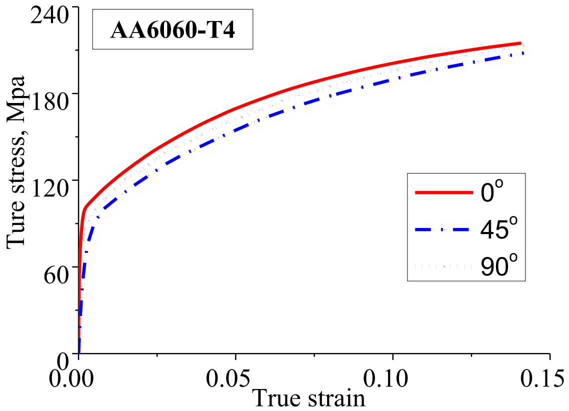

Figure 4-3 The true strain-stress curves of uniaxial tensile tests along three orientations from the extrusion direction of AA6060 tube.

Table 4-2 Material properties of the AA6060-T4 tube

Elastic modulus E (GPa)	Density ρ (kg/m^3)	Poisson' ratio υ	Initial yield stress $\sigma_{0.2}$ (MPa)	Ultimate strength σ_b
64	2700	0.33	99.6	243

Table 4-3 Material anisotropic data of the AA6060-T4

σ_0 / σ_0	σ_0 / σ_{45}	σ_0 / σ_{90}	σ_b / σ_0	r_0	r_{45}	r_{90}	r_b
1	0.843	0.929	1	0.492	0.367	1.277	0.353

The value of r_b was calculated with Yld96 (Barlat et al., 2003).

4.2 Material parameters for yield functions

4.2.1 DP steels

For plastic anisotropy and the identification of the yield condition, the coefficients were determined using two different approaches with Hill'48 model. The classical approach accounts mainly for the r-values from three uniaxial tension tests (0°, 45° and 90° from the RD) and leads to the model labelled 'Hill 48-R'. Alternatively, the second approach resorts to a set of three yield stresses from uniaxial tension tests, which was labelled by 'Hill 48-S'. For the studied material DP500 steel, the input data and the coefficients corresponding to Hill 48-R and Hill 48-S are listed in Table 4-4.

Table 4-4 Material parameter identification of DP500 for anisotropic yield criteria.

Label	Y_0	Y_{45}	Y_{90}	Y_b	r_0	r_{45}	r_{90}	r_b	
Anisotropy	1	1.026	1.015	1.053	0.95	0.81	1.1	0.843	
Label	F	G	H	N					
Hill 48-R	0.4429	0.5128	0.4872	1.252					
Hill 48-S	0.4363	0.4656	0.5344	1.449					
Label	α_1	α_2	α_3	α_4	α_5	α_6	α_7	α_8	α
Yld2000-2d	0.9882	0.9829	0.8889	0.9616	0.987	0.9079	0.9461	1.0497	6

The values of Y were determined at a specific plastic work.
The value of r_b was calculated with Yld96 (Barlat et al., 2003).

The determination of the material coefficients for the Yld2000-2d model requires 3 uniaxial tension tests and an equi-biaxial stress state (bulge), which leads to four yield stress ratios Y_0, Y_{45}, Y_{90}, Y_b and four r-values r_0, r_{45}, r_{90}, r_b. In this work, the r_b value, i.e., $r_b = d\varepsilon_{TD} / d\varepsilon_{RD}$, was calculated using another yield condition, namely Yld96 (Barlat, et al., 2003). Note that the stress ratios Y were not the values at yield but those determined at a specific plastic work of 80MPa, which leads to a behaviour that is more representative of the global deformation range (Yoon et al., 2006). The resulting Yld2000-2d coefficients for DP500 steel are listed in Table 4-4. Note that the exponent *a* of the Yld2000-2d model for BCC materials is set to 6.0.

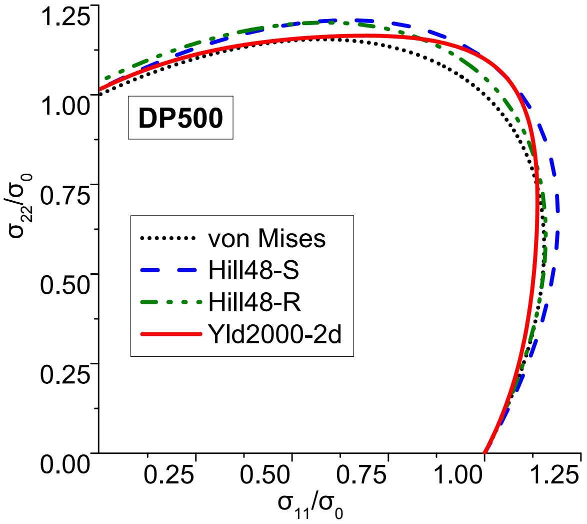

Figure 4-4 Predicted yield surface contours for DP500 with von Mises, Hill'48 and YLD-2000-2d.

The yield loci predicted with the different models considered in this study are plotted in Figure 4-4. The normalized yield stresses and r-values predicted with the different yield functions are compared with the corresponding experimental data in Figure 4-5.

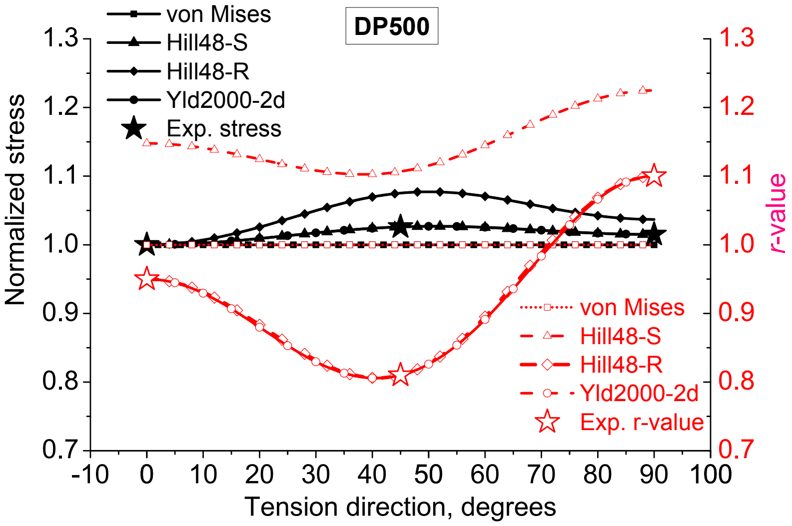

Figure 4-5 Experimental and calculated variations of the normalized yield stress and r-value as a function of the tension angle with respect to rolling direction.

It can be observed that Yld2000-2d exactly captures both yield stresses and r-values. The Hill 48-R yield criterion captures the r-value very well but slightly overestimated the yield stresses at 45º and 90º. In contrast, Hill 48-S is able to capture the anisotropy of the yield stress but obviously overestimated the r-value. That means, the Hill's 48 model is not able to describe the anisotropies of the yield stress and r-value simultaneously. For DP600 and DP780 steels, the resulting anisotropic coefficients for the yield criteria are listed in Table 4-5 and Table 4-6, respectively.

Table 4-5 Material parameter identification of DP600 for anisotropic yield criteria.

Label	Y_0	Y_{45}	Y_{90}	Y_b	r_0	r_{45}	r_{90}	r_b	
Anisotropy	1	0.995	1.014	1.032	0.65	0.91	0.81	0.774	
Label	F	G	H	N					
Hill 48-R	0.4863	0.6061	0.3939	1.5403					
Hill 48-S	0.4558	0.4832	0.5168	1.5507					
Label	α_1	α_2	α_3	α_4	α_5	α_6	α_7	α_8	α
Yld2000-2d	0.935	0.968	0.89	0.981	1.017	0.939	0.987	1.072	6

Table 4-6 Material parameter identification of DP780 for anisotropic yield criteria.

Label	Y_0	Y_{45}	Y_{90}	Y_b	r_0	r_{45}	r_{90}	r_b	
Anisotropy	1	1.034	1.057	1.086	0.65	0.9	0.8	0.712	
Label	F	G	H	N	L	M			
Hill 48-R	0.4924	0.6061	0.3939	1.5379	1.5	1.5			
Hill 48-S	0.3715	0.4764	0.5236	1.4467	1.5	1.5			
Label	α_1	α_2	α_3	α_4	α_5	α_6	α_7	α_8	α
Yld2000-2d	0.973	0.879	0.864	0.948	0.999	0.86	0.949	1.030	6

4.2.2 AA6060-T4

The anisotropic coefficients of Hill'48-R yield function are listed in Table 4-7, which are calculated based on the three r-values, r_0, r_{45}, r_{90}. The material characterization for the Yld2000-2d model requires 3 tensile tests and a test for the equi-biaxial stress state. Since the equi-biaxial experiment is not available for the thin-walled tube, the uniaxial stress along the extrusion direction was arbitrarily used instead. Note that the exponent *a* in the Yld2000-2D model for FCC materials is taken to be equal to 8.0. The input data of stresses were not the values at yield but those determined at a specific plastic work of 15 MPa.

Table 4-7 Material parameters of AA6060-T4 for anisotropic yield criteria.

Label	F	G	H	N				
Hill 48-R	0.258	0.670	0.330	0.805				
Label	α_1	α_2	α_3	α_4	α_5	α_6	α_7	α_8	α
Yld2000-2d	0.766	1.266	0.751	0.975	1.052	1.070	0.871	1.592	8

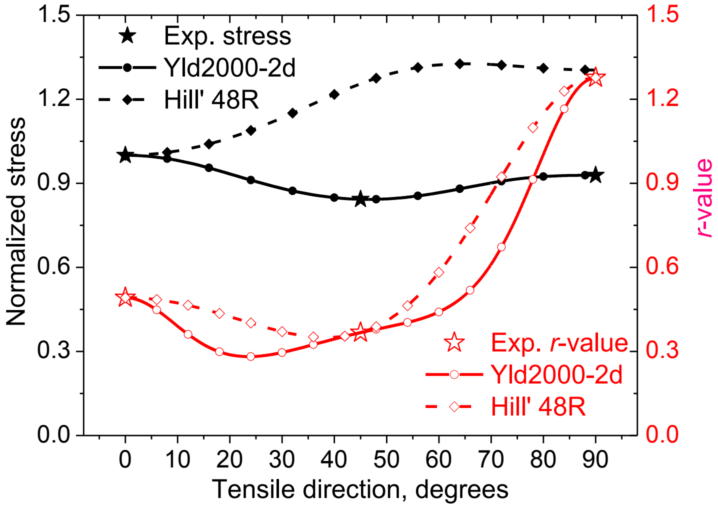

Figure 4-6 Experimental and calculated variations of the normalized yield stress and r-value as a function of the angle between extrusion and tensile direction for AA6060-T4 tube.

A comparison of the predicted normalized yield stresses and anisotropy coefficients by the two anisotropic yield criteria, i.e. Yld2000-2d and Hill’48, are shown in Figure 4-6. It can be noticed that the Yld2000-2d exactly captures both yield stress and r-values while the Hill’48R yield criterion captures the r-value very well but overestimates the yield stresses. It also shows that the Hill’s model is limited to describe the anisotropy of stress and strain simultaneously.

4.3 Material parameters for hardening models

4.3.1 DP steels

In this work, the anisotropic hardening behaviours have mainly been described by the distortional hardening model HAH. The parameter identifications of this model and the reference isotropic hardening model were uncoupled. The parameters of the reference isotropic hardening model, i.e., the Swift law, were determined by a best approximation of the stress-strain curve from the bulge stress-strain curves. The six parameters k , k_{1-5} , control the evolution of state variables for the reverse loading, i.e., the forward-reverse shear test. In this procedure, the multidimensional optimization method Nelder-Mead simplex was used to minimize the error. The corresponding calculating code was provided by Ha et al. (2013). For comparison purposes, the traditional isotropic hardening (IH) model and the combined isotropic and kinematic hardening (IHKH) model were also adopted for the representation of the hardening behaviour of the materials. All the three hardening models are integrated with the Yld2000-2d yield function. The parameters of the adopted hardening models are summarized in Table 4-8.

Table 4-8 Coefficients of the adopted hardening models for the DP steels.

	Material	q	k	k_1	k_2	k_3	k_4	k_5
HAH	DP500	2	14	80	33.4	0.48	0.83	7
	DP600	2	44	65	16.1	0.31	0.75	4
	DP780	2	45	50	26.2	0.3	0.8	5
	Material	K	ε_0	n				
Swift law	DP500	896	0.0044	0.161				
	DP600	1033.5	0.004	0.171				
	DP780	1298.2	0.0015	0.151				
IHKH	Material	K(MPa)	ε_0	n	C	γ		
	DP500	712	0.0634	0.211	3995.5	26.4		
	DP780	744	0.0016	0.061	7990.7	26.0		

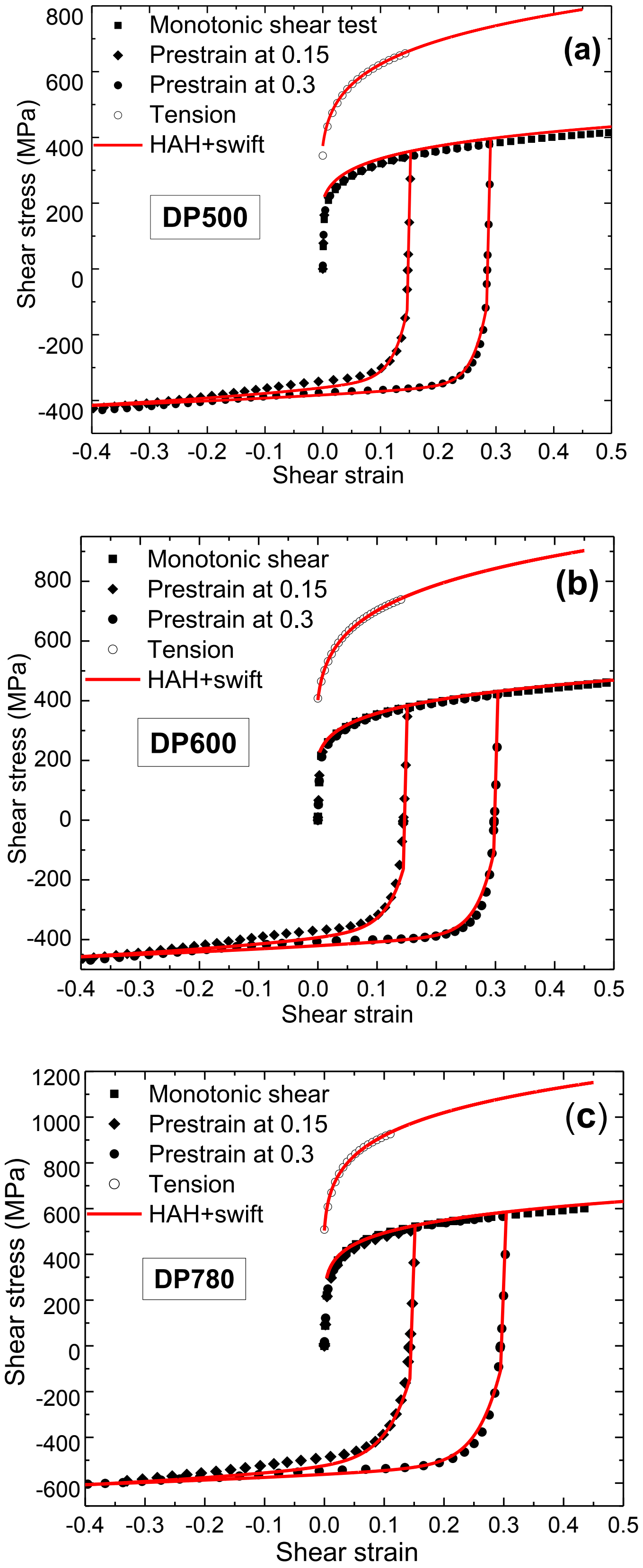

Figure 4-7 Comparison of stress-strain relations between experimental and predicted results based on the HAH model: (a) DP500 (b) DP600 (c) DP780.

The comparison of the experimental strain-stress curves and the calculated results based on the HAH model is shown in Figure 4-7. Three simple shear tests were conducted: monotonic and with reversals at 15% and 30%. It can be observed that the hardening model captures well the Bauschinger effect, transient hardening with high rate and permanent softening.

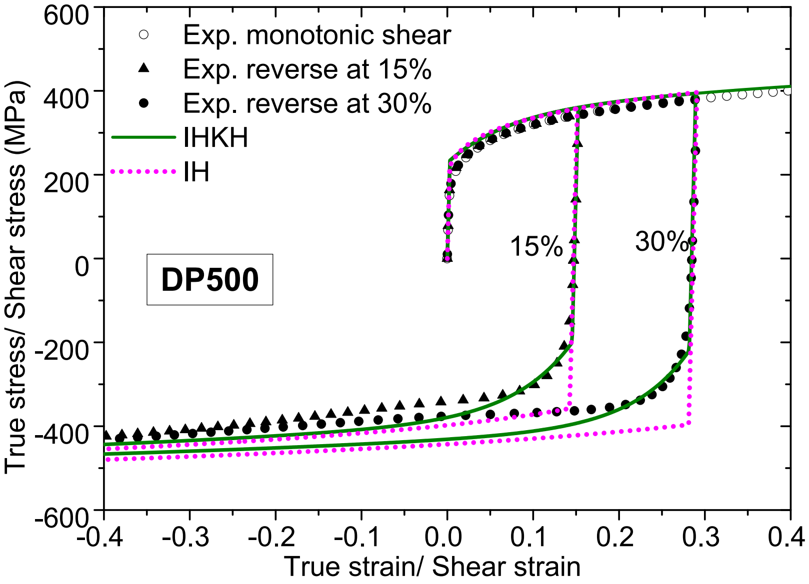

Figure 4-8 Comparison of stress-strain relations between experimental and predicted results based on the IH and IHKH models for DP500.

Figure 4-8 illustrates the comparison results calculated with the IHKH model, IH model and those of the experiments for DP500 steel. The experiment of forward-reverse shear test shows that the material exhibits strong transient Bauschinger effect just after reverse loading. Work hardening stagnation and permanent softening are also observed for this material. For the modelling results, it can be observed that the IH model always overestimates the stress after load reversals. The difference is especially huge at the onset of load reversals. In contrast, the IHKH model captures the transient Bauschinger effect, thus it give a better description of the flow stress under load reversal than the IH model. However, it still cannot reproduce the work hardening stagnation and the permanent softening.

4.3.2 AA6060-T4

For this tube sample, it is not available to conduct a hydraulic bulge test. Therefore, the uniaxial stress-strain behaviour measured along the extrusion direction was used to express the hardening of the material using Voce law.

$$\bar{\sigma} = \begin{cases} E\bar{\varepsilon} & \bar{\varepsilon} \le \varepsilon_0 \\ \sigma_0 + Q[1 - \exp(-b\bar{\varepsilon}^p)] & \bar{\varepsilon} > \varepsilon_0 \end{cases} \tag{4.1}$$

where σ_0 is the initial yield stress, ε_0 is the initial yield strain, *Q* and *b* are the material parameters. For this material, the Voce model reproduces the experimental strain-stress curve better than the Swift model. The model parameters of the IHKH model with von Mises, Yld2000-2d and Hill’48-R yield criteria are identified by analytic method and then calibrated by numerical testing. The resulting parameters of the IH and IHKH models are listed in Table 4-9.

Table 4-9 Material parameters of the adopted hardening models for AA6060-T4.

IH	σ_0 *(MPa)*	*Q (MPa)*	*b*			
	99.6	143.9	14.7			
IHKH	Yield criterion	σ_0 *(MPa)*	*Q (MPa)*	*b*	*C (MPa)*	γ
	von-Mises	92.6	126.5	8.37	2058.1	45.9
	Hill'48R	85.76	139.1	6.47	3338.8	59.9
	Yld2000-2d	86.4	137.5	6.74	3221.2	59.6

In the previous work, Liao et al. (2014) showed that the Yld2000-2d yield criterion always leads to the lowest errors for a given hardening law. The identification results for all criteria are very similar and only the results for the Yld2000-2d criterion with or without kinematic hardening are presented. As shown from Figure 4-9, the identified curves show good agreement on anisotropy for tensile and shear test simulations for both models, albeit the monotonic shear stress has some scatter in large deformation. It should be worth noting that evident difference of the hardening laws occurs in the forward and reverse shear tests. After the load reverse, the IHKH model reproduces the Bauschinger effect and transient behaviour of this material very well whereas the IH model captures neither of them. Although some discrepancies are found in reproducing the curve crossing response (Rauch et al., 2007) by the IHKH model, the whole predicted results by the IHKH model are acceptable.

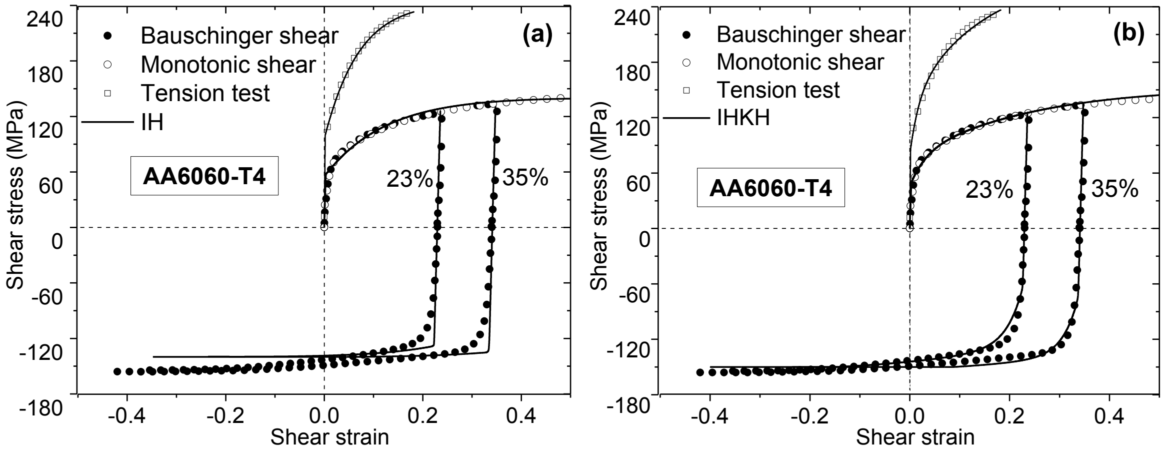

Figure 4-9 Forward and reversal shear stress-strain curves predicted by the Yld2000-2d yield criterion and (a) IH model (b) IHKH model.

4.4 Determination of elastic modulus for DP steels

Although considerable research has been devoted to the explanation and constitutive description of nonlinear elastic behaviour, rather less attention has been paid to appropriate measurement technique under different loading strategies. The elastic modulus is generally determined in uniaxial loading-unloading-loading (ULUL) cycle tensile test (Govik et al., 2014; Chen et al., 2016). This uniaxial resulting data may not be applicable to multi-axial forming processes such as deep drawing. Hence, there is an increasing interest in planar biaxial tensile test with various types of cruciform specimens (Leotoing et al., 2015; Liu et al., 2015), in order to consider the biaxial stress conditions that exist in real sheet forming (Hanno, 2008). One of the most reliable biaxial tensile tests conducted on a cruciform specimen was developed by Kuwabara et al. (1998, 2002). It was successfully employed to study the biaxial loading-unloading-loading (BLUL) elastic behaviour of AHSS (Andar et al., 2010). The other efficient method for measuring the elastic modulus is the three-point bending (TPB) with a rectangular specimen (Yoshihara et al., 2006; Xue et al., 2015b)). Although the TPB has been extensively used for the calculation of the initial elastic modulus of various materials (Alaoui et al., 2008; Sousa et al., 2015), it has never been further developed for the determination of the nonlinear elastic modulus associated with pre-strained sheet material. The above-described efforts provide a good insight into how different loading strategies can affect the nonlinear elastic modulus evolution.

4.4.1 Uniaxial tension

The initial elastic modulus under uniaxial tension denoted as E_0^U was determined by using the linear regression fitting method. The range of linear fitting was taken to be from approximately 50 MPa up to half of the apparent yield stress, as shown in Figure 4-10. This is because the early stage of the loading was not sufficiently stable, even at a low strain rate due to the inevitable noise of the tensile machine. For the pre-strained sheet specimens, the slope of a straight line drawn through the two stress-strain endpoints at a prescribed plastic strain was defined as the corresponding elastic modulus.

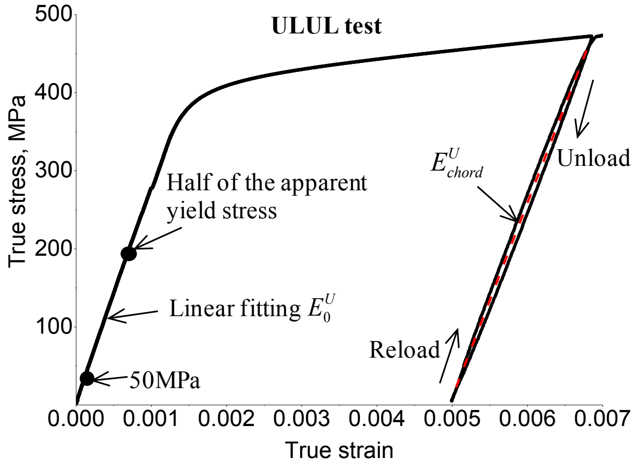

Figure 4-10 A schematic illustration of the elastic moduli under uniaxial tensile loading

The mechanically-measured data and the fitting evolution of the elastic modulus degradation for DP500, DP600 and DP780 are represented in the Figure 4-11a, b and c respectively. Three measurements for each material were performed in order to emphasize the repeatability of the results. Since the results for each specimen are practically identical, only one of them is represented on the figures. It can be seen that the decrease of the elastic modulus for DP500 is 18.9% of its initial value at a pre-strain of 0.13. Further plastic strain (i.e., larger than 0.13) did not resulted in more degradation of the elastic modulus, leading to a saturation value of 160.56 GPa. The degradation of the elastic modulus for DP600 is 19.6% at a pre-strain of 0.127 and the saturation value is 160.73 GPa. DP500 and DP600 exhibit a similar unloading elastic behaviour. For DP780, the decrease of the elastic modulus is 24.0% of its initial state at a pre-strain of 0.09 while the saturation value is 157.42 GPa. DP780 was pre-strained up to only 0.09 although a uniaxial uniform elongation of DP780 is 0.14. This is because buckling occurs during reloading for pre-strain larger than 0.09. Although the pre-strain of DP780 is not high, it can be observed that the degradation of elastic modulus already tends to saturate.

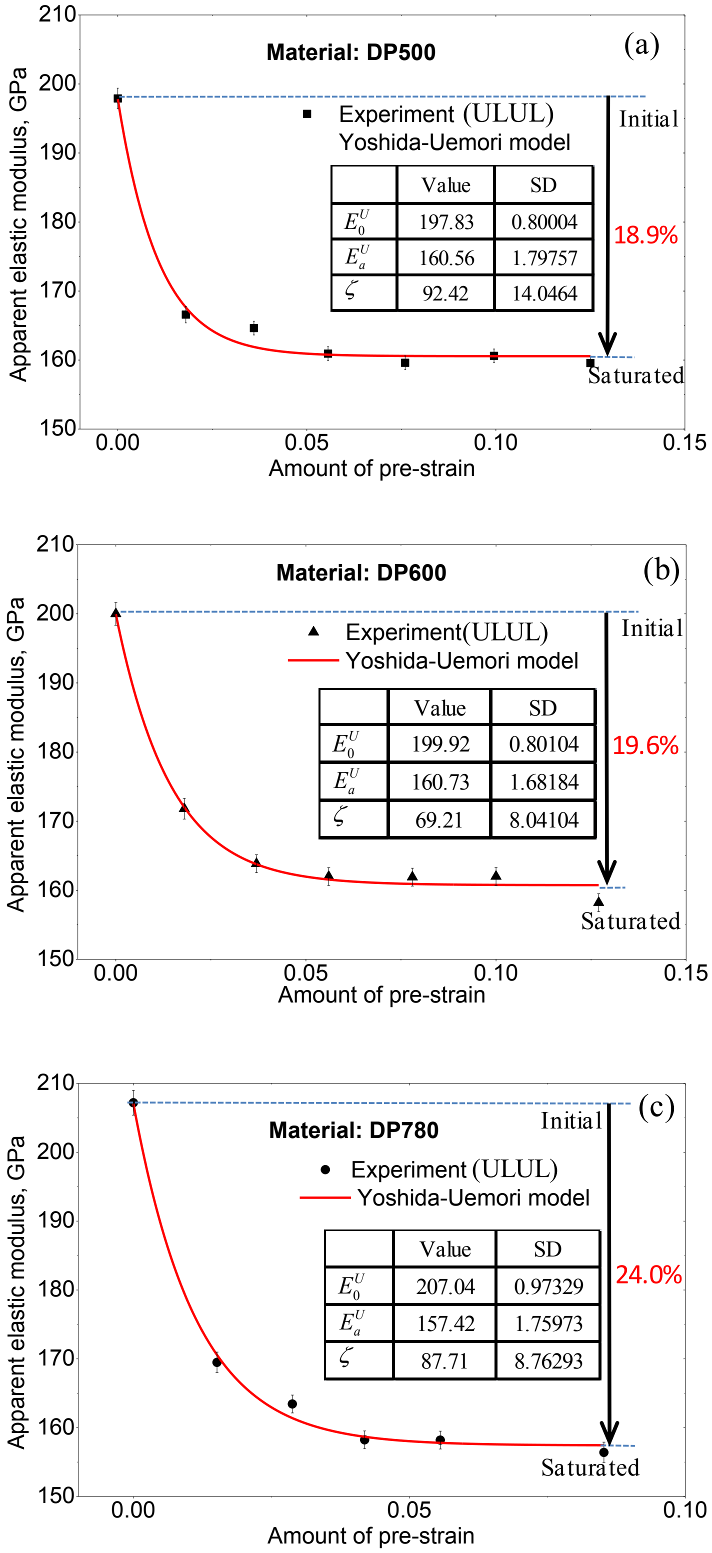

Figure 4-11 The degradation of uniaxial elastic modulus with pre-strain: (a) DP500 (b) DP600 (c) DP780.

4.4.2 In-plane biaxial tension

Generally, a biaxial tensile stress system has a tensile stress state in two directions and a shear stress. True stress components (σ_x^B, σ_y^B) were determined by using the measured loads F_x and F_y. The measured values of the biaxial plastic strain components ($\varepsilon_x^B, \varepsilon_y^B$) were obtained from the current cross-sectional area of the gauge region. Due to equi-biaxial tension and the symmetry of the experimental set-up with the cruciform specimen, the shear stress was ignored. In addition, the effects of elastic anisotropy were neglected when calculating the average unloading elastic modulus with pre-strain. Since the elastic stress-strain relationship for biaxial loading is linear with a constant compliance matrix, the increments of strains can be calculated from the increments of applied stresses by

$$\begin{bmatrix} \Delta\varepsilon_x^B \\ \Delta\varepsilon_y^B \end{bmatrix} = \begin{bmatrix} \dfrac{1}{E_{equi}^B} & \dfrac{-\nu}{E_{equi}^B} \\ \dfrac{-\nu}{E_{equi}^B} & \dfrac{1}{E_{equi}^B} \end{bmatrix} \cdot \begin{bmatrix} \Delta\sigma_x^B \\ \Delta\sigma_y^B \end{bmatrix} \tag{4. 2}$$

where E_{equi}^B and ν denote the equivalent elastic modulus under biaxial loading and Poisson's ratio respectively. The equivalent elastic modulus can be calculated by averaging the elastic moduli in the rolling (E_x^B) and transverse (E_y^B) directions, which can be separately obtained from the BLUL experimental data and Eq. (4.2)

$$E_{equi}^B = E_{avg}^B = \frac{E_x^B + E_y^B}{2} \tag{4.3}$$

In this method, it is not necessary to estimate the equivalent stress to describe the material behaviour (equivalent true stress-strain curve) under biaxial loading. The thickness strain ε_t^B in the centre area of the cruciform specimen can be considered to be equal to the equivalent total plastic strain from plastic work equivalence, and calculated by evoking the assumption of material incompressibility, that is

$$\varepsilon_{equi}^B = -\varepsilon_t^B = \varepsilon_x^B + \varepsilon_y^B \tag{4.4}$$

where ε_x^B and ε_y^B are the plastic strain components in the rolling and transverse directions respectively.

Table 4-10 The elastic modulus evolution of DP steels with plastic strain by BLUL tests.

Materials	Unloading	ε_x^B	E_x^B	ε_y^B	E_y^B	ε_{equi}^B	E_{chord}^B	ΔE^B
DP500	Initial	0	220.05	0	190.20	0	205.13	14.46%
	1st	0.0049	204.39	0.0068	174.86	0.0117	189.62	15.58%
	2nd	0.0064	206.57	0.0091	169.26	0.0155	187.91	19.86%
	3rd	0.0083	206.92	0.0118	172.13	0.0201	189.52	18.36%
	4th	0.0106	207.20	0.0153	169.86	0.0259	188.28	19.80%
	5th	0.0133	207.10	0.0192	169.54	0.0325	186.82	19.90%
DP600	Initial	0	218.22	0	187.26	0	202.75	15.28%
	1st	0.0048	202.53	0.0068	172.69	0.0116	187.61	15.90%
	2nd	0.0063	201.39	0.0092	169.50	0.0155	185.44	17.20%
	3rd	0.0082	196.14	0.0110	168.11	0.0192	182.12	15.40%
	4th	0.0102	191.66	0.0140	168.21	0.0242	179.94	13.04%
	5th	0.0125	191.10	0.0180	163.73	0.0305	177.42	15.42%
	6th	0.0150	191.80	0.0215	163.80	0.0365	177.80	15.74%
DP780	Initial	0	218.03	0	187.86	0	202.94	14.86%
	1st	0.0045	201.08	0.0062	173.29	0.0107	187.19	14.84%
	2nd	0.0051	201.11	0.0070	173.03	0.0121	187.07	15.02%
	3rd	0.0060	199.15	0.0082	171.71	0.0142	185.43	14.80%
	4th	0.0069	198.99	0.0096	170.70	0.0165	184.84	15.30%
	5th	0.0080	193.84	0.0110	173.18	0.0190	183.51	11.26%
	6th	0.0092	194.60	0.0129	166.81	0.0221	180.71	15.38%
	7th	0.0106	193.37	0.0150	167.30	0.0256	180.33	14.46%

$\Delta E^B = (E_x^B - E_y^B) \times 100\% / (E_0^B)$.

In order to determine the unloading elastic moduli from BLUL tests, the Yoshida chord model was adopted again. Some key measured data associated with the elastic modulus evolution are listed in Table 4-10. It can be seen that all the deviation amplitude (ΔE^B) of the current elastic moduli in the rolling and transverse directions are in a range of 10 to 20%. It indicates that the existing anisotropy of elastic behaviour of the DP steels is not obvious. The biaxial elastic moduli are plotted as a function of the equivalent pre-strain in Figure 4-12a, b and c for DP500, DP600 and DP780 respectively. It can be observed that the degradations of the elastic modulus for the three materials are 8.5, 14.0 and 13.3% of the initial value, respectively. The modulus degradation as a function of the equivalent plastic strain for DP500 saturated earlier than that of the other two materials.

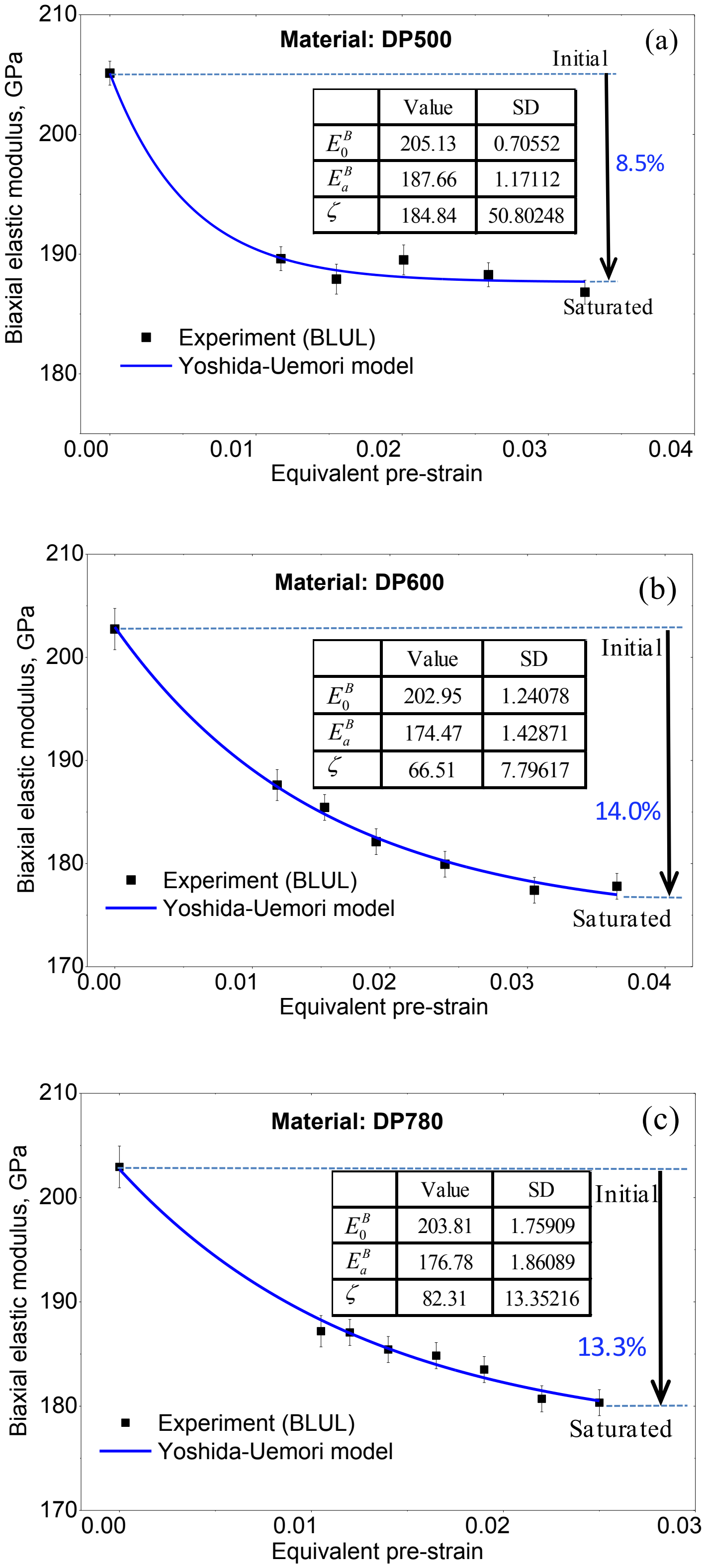

	Value	SD
E_0^B	205.13	0.70552
E_a^B	187.66	1.17112
ζ	184.84	50.80248

	Value	SD
E_0^B	202.95	1.24078
E_a^B	174.47	1.42871
ζ	66.51	7.79617

	Value	SD
E_0^B	203.81	1.75909
E_a^B	176.78	1.86089
ζ	82.31	13.35216

Figure 4-12 The degradation of biaxial elastic modulus with pre-strain: (a) DP500 (b) DP600 (c) DP780.

In addition, a maximum pre-strained of only 0.04 was achieved in this test because of geometric constraints. The central specimen area is under a biaxial stress state while the arms are under uniaxial stress. Note that the plastic deformation before rupture is much less for biaxial or multi-axial tension than that for uniaxial tension (Young and Budynas, 2002). As a result, the strains in the arms are higher than in the central part. When the stress in the arms reaches a plateau after the yield point, very large deformations are produced in the arms for small increments of stress. Meanwhile, the strain in the central part remains almost unchanged or slightly increases. This leads to the occurrence of the final fracture in the arms of the cruciform specimen, as shown in Figure 4-13. In short, the unbalanced deformation in the arms and central part of the cruciform specimen leads to premature fracture.

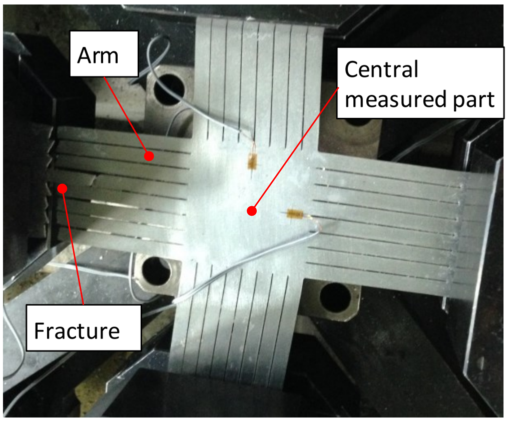

Figure 4-13 The occurrence of fracture in the arms of the cruciform specimen.

4.4.3 Three-point bending (TPB)

To calculate the elastic modulus of a sheet from the three-point bending test, an improved elementary beam theory was introduced (Kourtis, 2014). It relies on assumptions including homogenous, isotropic material properties and cross sections remain plane after bending. Dynamic effects can be also ignored due to the low deflection rate of three-point bending test. The elastic modulus in the longitudinal direction (also rolling direction) obtained from this test (denoted E_p^T) can be calculated from the following equation:

$$E_p^T = \left(\frac{F \cdot L^3}{48 \cdot S \cdot I} \right) \cdot \left[1 + \frac{12 \cdot k \cdot I \cdot (E_L / G_T)}{A \cdot L^2} \right] \tag{4. 5}$$

with

$$E_L / G_T = 2 \cdot (1 + \upsilon) \tag{4.6}$$

and where F is the load applied by the central loading ram, L the span length between the outer supports, S the stroke at mid-span, I the inertia moment of the section with respect to sheet normal direction, k a parameter that depends on the cross-sectional shape of the beam, E_L the elastic modulus in the longitudinal plane, G_T the shear modulus in the transverse plane and A is the cross sectional area. In Eq. (4.5), the second term within the brackets is the additional contribution due to transverse shear. For the proposed three-point bending configuration, the influence of the transverse shear stress on deformation is very small and can be ignored since the sheet thickness is far smaller than the span (t/L=0.0067). Therefore, the calculation of E_p^T can be simplified to following relation:

$$E_p^T = \left(\frac{F}{S}\right) \cdot \frac{L^3}{48 \cdot I_p} \tag{4.7}$$

where

$$I_p = \frac{W_p t_p}{12} \tag{4.8}$$

In Eq. (4.7), $\left(\frac{F}{S}\right)$ is the slope of the tangent to the initial straight-line portion of the load-stroke curve, I_p the inertia moment of the section after pre-straining, and W_p, t_p are the average width and thickness of pre-strained specimen respectively.

In this work, large uniaxial tensile specimens, as shown in Figure 3-11, were pre-strained to several values, i.e., 0.02, 0.04, 0.06, 0.08 and 0.10. Subsequently, the pre-strained sheet was cut according to the requirement of standard three-point bending test. A more detailed experimental procedure was described in Section 3.2.5. Table 4-11 lists the key elements for the calculation of the elastic modulus using TPB-P tests. It can be seen that the values of the initial elastic modulus along the rolling direction obtained from the standard TPB tests are a slightly different for the three materials. The linear fitting range for the force and the slope of the load-stroke curve was taken to be from 20N up to approximately half of the apparent yield force (50N). The experimental data at the early stage of the loading was removed due to the lack of stability. The inevitable noise might result from the contact between specimen and tools. The standard deviation (SD) of the linear fitting slope is less than 0.003, which indicates that the selected experimental data were satisfactory.

Table 4-11 Key elements for calculating elastic modulus by TPB with pre-strained sheets.

Materials	E_0^T (GPa)	Pre-strain	W_p (mm)	t_p (mm)	F/S (N/mm)	SD of F/S	E_p^T (GPa)
DP500	210.07	0.02	19.85	0.785	3.995	0.00244	177.90
		0.04	19.65	0.778	3.840	0.00115	177.49
		0.06	19.45	0.765	3.597	0.00240	176.67
		0.08	19.25	0.758	3.414	0.00220	174.17
		0.10	18.95	0.748	3.219	0.00145	174.13
DP600	208.04	0.02	19.85	0.782	3.983	0.00206	174.96
		0.04	19.80	0.770	3.687	0.00249	174.27
		0.06	19.72	0.765	3.584	0.00295	173.62
		0.08	19.40	0.758	3.380	0.00283	171.10
		0.10	19.25	0.750	3.248	0.00147	171.03
DP780	212.70	0.02	19.90	0.785	3.899	0.00132	173.23
		0.04	19.75	0.775	3.625	0.00201	168.64
		0.06	19.45	0.765	3.406	0.00220	167.30
		0.08	19.30	0.760	3.350	0.00163	169.20
		0.10	19.20	0.755	3.250	0.00152	168.22

E_0^T : Initial elastic modulus without pre-straining obtained from TPB test.

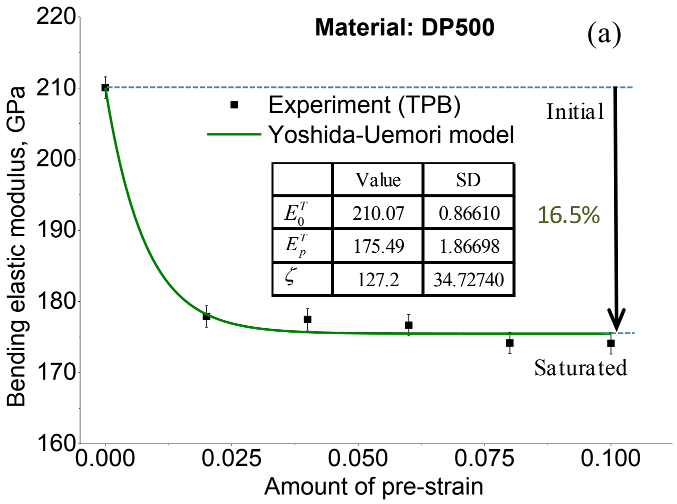

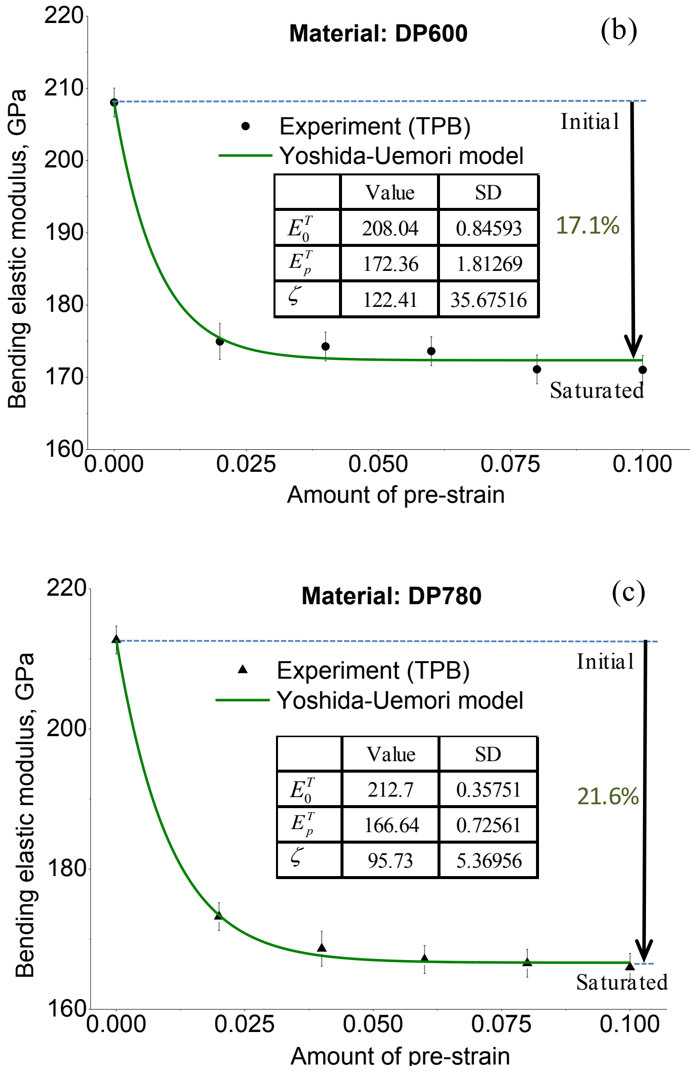

Figure 4-14 The degradation of bending elastic modulus with pre-strain: (a) DP500 (b) DP600 (c) DP780.

Figure 4-14 shows the evolution of bending elastic modulus with the increase of pre-strain. The decrease of the elastic modulus for DP500, DP600 and DP780 were respectively 16.5%, 17.1% and 21.6% from the initial to the saturated value. All the degradations reached the saturated state at an early stage before a plastic strain 0.04, although a large strain can be achieved for the TPB-P test.

4.5 Loading strategy dependence on the determination of elastic modulus

4.5.1 Comparative analysis

Figure 4-15 compares the elastic modulus obtained by the different loading strategies. It is clear that the loading strategy has an effect on the determination of the nonlinear elastic modulus. Figure 4-15a shows that the three-point bending (TPB) test leads to the highest initial elastic modulus compared to the other methods while uniaxial tension leads to the lowest. This might be due to the low force and high deflection in the TPB test, which ensure almost all the deformation within the elastic range. However, Figure 4-15b indicates that the largest modulus decrease occurs in uniaxial tension while the lowest occurs in biaxial tension.

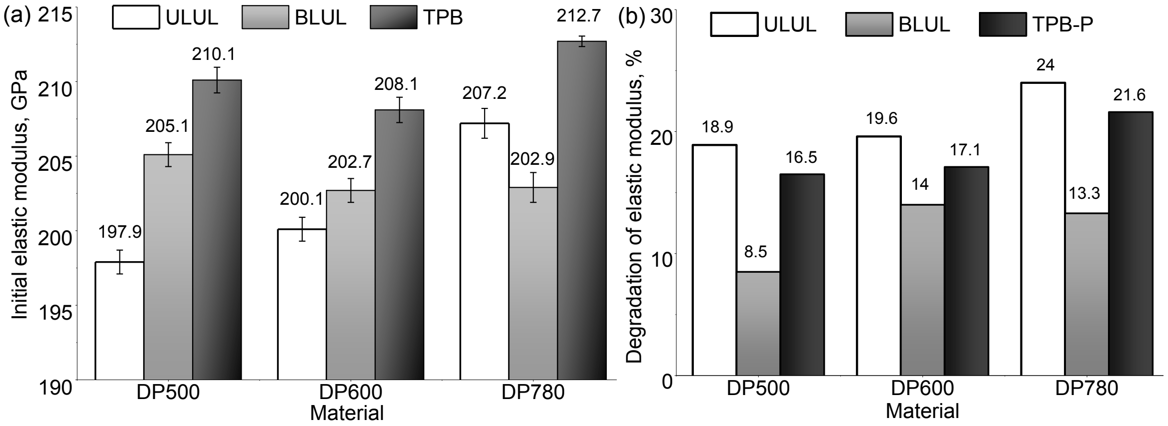

Figure 4-15 Comparison of elastic moduli under different loading path tests: (a) initial elastic modulus (b) degradation of elastic modulus at saturation.

For the different materials, it seems that both initial and degradation of elastic modulus of DP780 steel are a slightly higher than the other two steels under uniaxial and TPB-P loading strategies, except for biaxial loading, which might be due to the limited strain gauge. One of possible reasons is the small difference of microstructure of dual-phase steels, i.e., the DP780 steel has lower average ferrite grain size or the higher volume fraction of martensite than DP500 and DP600. At early material production stage, the austenite to martensite transformation generates large tension residual stresses in the phase interfaces, which is more easily released and generate plastic deformation during uniaxial tension compared to under multi-axial loading strategies such as biaxial deformation and bending. However, it is difficult to further interpret the difference affecting the changes of elastic modulus by microstructural observation.

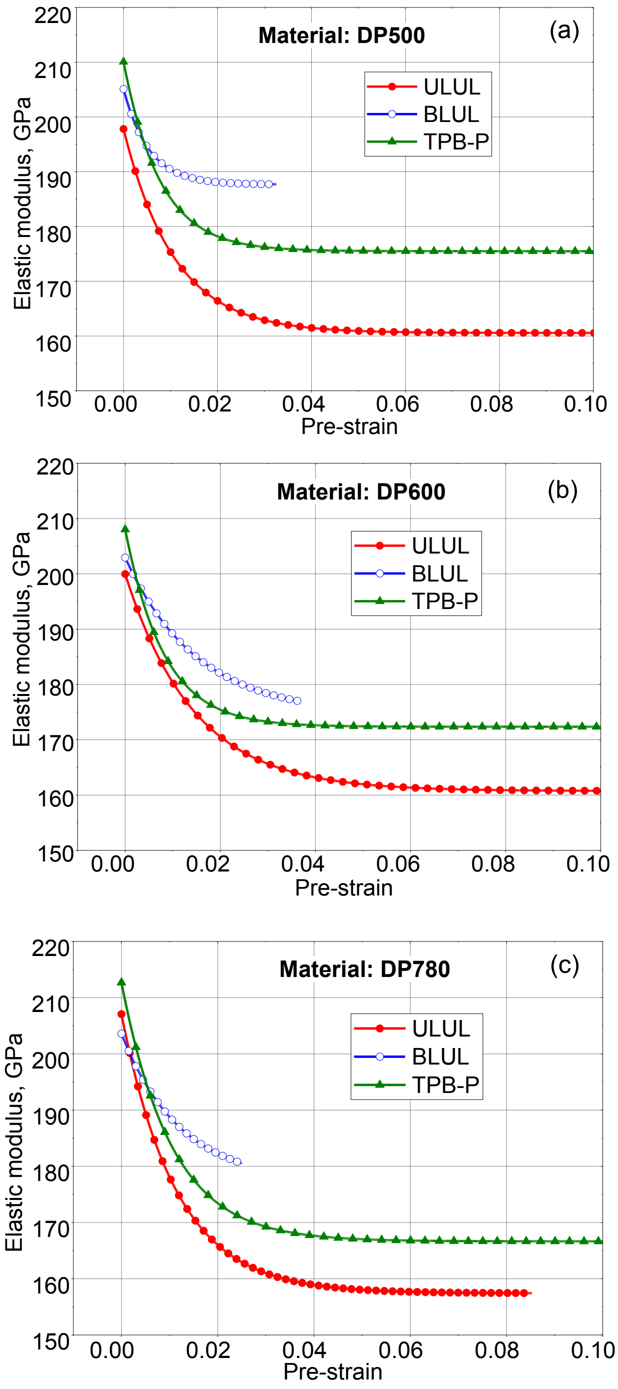

Figure 4-16 Comparison of the evolution of elastic modulus degradation under different loading strategies: (a) DP500 (b) DP600 (c) DP780.

Figure 4-16 compares the evolution of the elastic modulus degradation of DP steels under different loading strategies, i.e., the fitting curves according to experimental data using

Yoshida chord model. It is observed that all degradations reach a saturated value at a pre-strain of about 0.04. DP500 under the biaxial loading strategy and DP600 under TPB-P seem to reach a saturated state earlier than the other cases, as shown in Figure 4-16a. Table 4-12 lists all coefficients for the Yoshida chord model under different loading strategies. These parameters can be introduced into a finite element analysis.

Table 4-12 Coefficients for Yoshida chord model under different loading strategies.

Loading	DP500			DP600			DP780		
type	E_0	E_a	ζ	E_0	E_a	ζ	E_0	E_a	ζ
ULUL	197.83	160.56	92.42	199.92	160.73	69.21	207.04	157.42	87.71
BLUL	205.13	187.66	184.34	202.95	174.47	66.51	203.81	176.78	82.31
TPB-P	210.07	175.49	127.20	208.04	172.36	122.41	212.70	166.64	95.73

4.5.2 Cycle effect and evolving elastic anisotropy

Although the degradation of the elastic modulus is mainly related to the plastic strain, it is still necessary to study the effect of loading-unloading cycle test. In this work, DP780 steel, which exhibits the most obvious elastic modulus degradation, was selected for ULUL tests with different cycles. The prescribed pre-strains up to a value of 0.085 through 1, 4 and 16 cycles were imposed as shown in Figure 4-17. The three unloading and reloading curves after different cycles seem overlap closely, and the standard error of the saturated chord moduli was only 1.085. Therefore, it can be made out that there is almost no cycle effect on the variation of elastic modulus degradation at macroscopic measurement and normal loading rate.

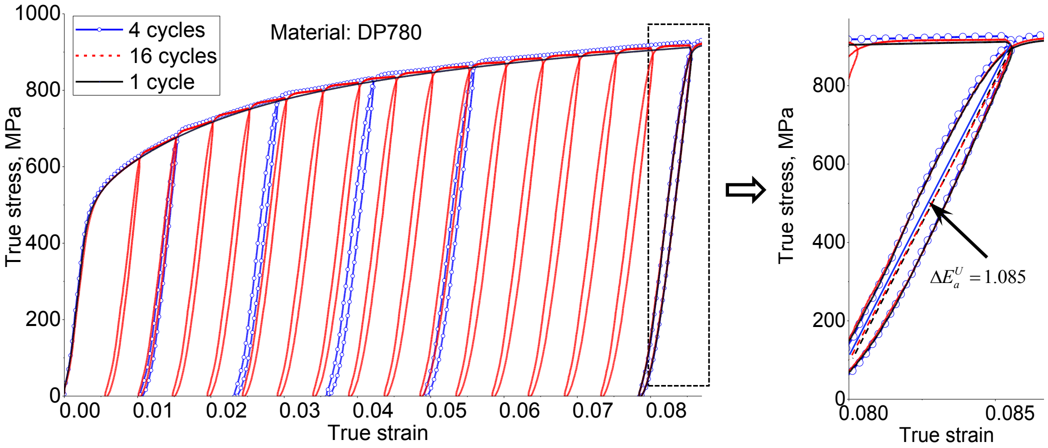

Figure 4-17 Effect of cyclic test on the degradation of elastic modulus.

In order to characterize and evaluate the elastic anisotropy of the analysed DP steel sheets, the experimental tests (ULUL) by using the uniaxial tension specimens in the 0 º, 45º and 90º with the rolling direction have been performed to characterize the material elastic anisotropy. As shown in Figure 4-18, the evolving elastic anisotropy of the analysed DP780 steel with the increase of plastic deformation is not obvious. The standard deviation of elastic anisotropy for initial sheet material without plastic deformation has only 4.189GPa or 2%. For the saturated state, it has only 0.55GPa after a pre-strain of 0.06. Therefore, in this work, the assumption of elastic isotropy is acceptable and makes less effect on the springback prediction.

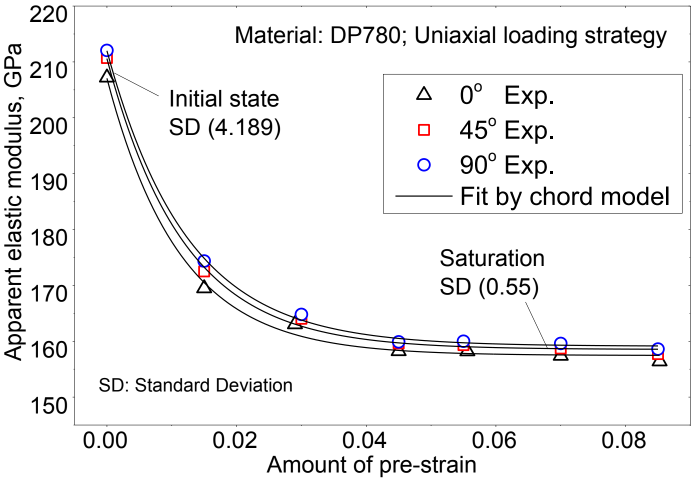

Figure 4-18 Experimental results of evolving elastic anisotropy with the increase of plastic deformation.

4.5.3 Application case: springback of curved-flanging test (CFT)

The above experimental analyses have shown that nonlinear elastic modulus degradation is sensitive to the loading strategy. Thus, it is important to know what test correctly measures the elastic modulus. Springback prediction is a possible indirect method for this assessment since the variation of the elastic modulus has a considerable effect on the numerical prediction of the elastic recovery. In this work, an experimental benchmark with a relatively simple and well-studied geometry, namely curved-flanging test (CFT), was introduced to validate the effects of degradation of the elastic modulus on the springback prediction. The CFT test is characterized by a velocity field and loading history, which involves multi-axial stress states, bending, strain path change and other non-uniaxial and non-linear behaviours.

4.5.3.1 Case description: forming simulation

Figure 4-19 illustrates the initial blank position and geometry of the three-dimensional CFT benchmark and experimental parts after springback associated with different DP steels. In this forming process, the blanks were fully lubricated on both sides with high viscosity mineral oil (viscosity: 40W80). The experimental investigation of the influence of lubrication on forming quality and the inverse identification of the friction coefficient using the digital image correlation technique is detailed in next section or a previous publication (Xue et al., 2016). Table 4-13 lists the main forming conditions and key numerical techniques under which the simulations were performed. After forming and springback, a coordinate-measuring machine (Aberlink 3D CMM system) was used to measure the central section coordinates of the part.

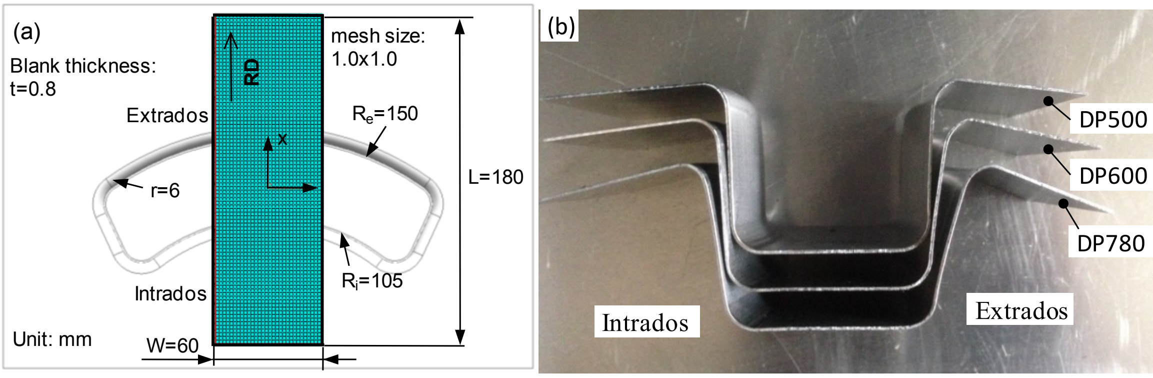

Figure 4-19 (a) An illustration of the location and geometry of initial blank (b) deformed experimental parts after springback.

Table 4-13 Main forming conditions and key numerical techniques

Main forming conditions		**Key numerical technology**	
1. Initial blank holder force, kN	60	1. Name of FEM code	Abaqus 6.11-PR3
2. Maximum holder force, kN	84	2. Basic formulations	Standard and explicit
3. Friction coefficient	0.066	3. Mesh number/elements	2700/ S4R
4. Drawing velocity, mm/min	10	4. Section integration point	11
5. Die clearance ratio	1.125	5. Contact property model	Surface-to-Surface
6. Total stroke, mm	40	6. Friction formulation	Coulomb (Penalty)

The FE-simulations of the forming process and springback were performed with the commercial code ABAQUS. In order to accurately capture the anisotropic hardening behaviour of DP steels, the yield criterion Yld2000-2d integrated into the homogeneous anisotropic hardening (HAH) framework was adopted. Previous efforts have already confirmed that this distortional hardening approach is appropriate to reproduce the Bauschinger effect and the associated transient hardening behaviour under strain path changes (Lee et al., 2012a; Ha et al., 2013). The Swift law was adopted as the reference isotropic hardening description of the analysed DP steels. The constitutive models mentioned above were successfully implemented into the FE code ABAQUS and applied to springback predictions in case of U-draw/bending by Lee et al. (2012b). The user-material subroutine code of the HAH model in this work was also provided by them.

The adopted material constitutive models were very efficient for the simulation of this forming process due to their ability in predicting complex material behaviour. Although the three materials exhibit similar results, the experimental observations indicate that the springback for DP780 steel is slightly higher. The detailed experimental and predicted springback results are listed in Appendix Table A.1. In this Section, the analysis pertaining to DP780 springback only is presented.

4.5.3.2 2D Springback analysis

For the comparison between the experimental and predicted springback profiles in measured central section (see Figure 4-20a), the sidewall curl (R_e and R_i) and angular springback (sidewall opening angle, θ_e^s, θ_i^s, and flange tip angle, θ_e^f, θ_i^f) on the intrados and extrados sides were defined as shown in Figure 4-20b.

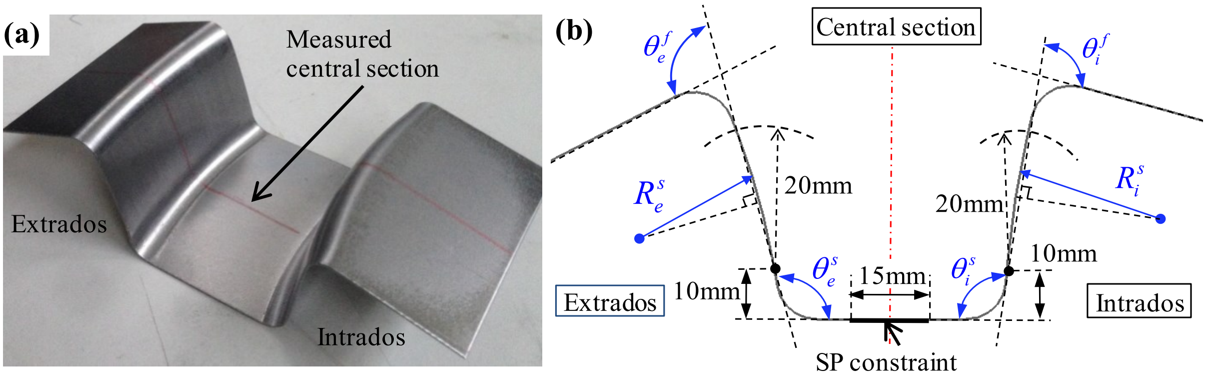

Figure 4-20 (a) Schematic measurement of central section (b) definition of measured springback parameters.

Figure 4-21 compares the experimental springback with the predicted results based on initial constant and decreasing elastic moduli, which were obtained from TPB tests. It can be seen that the springback prediction was underestimated by initial constant elastic modulus, especially for sidewall curl. The accuracy of prediction was improved considerably by considering the degradation of the elastic modulus.

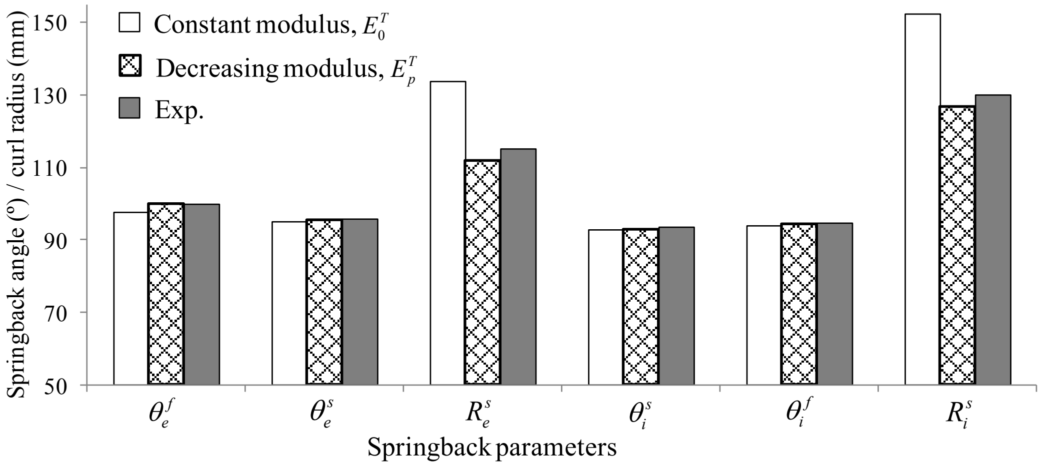

Figure 4-21 Comparison of the experimental springback and the predicted results based on constant and decreasing elastic moduli.

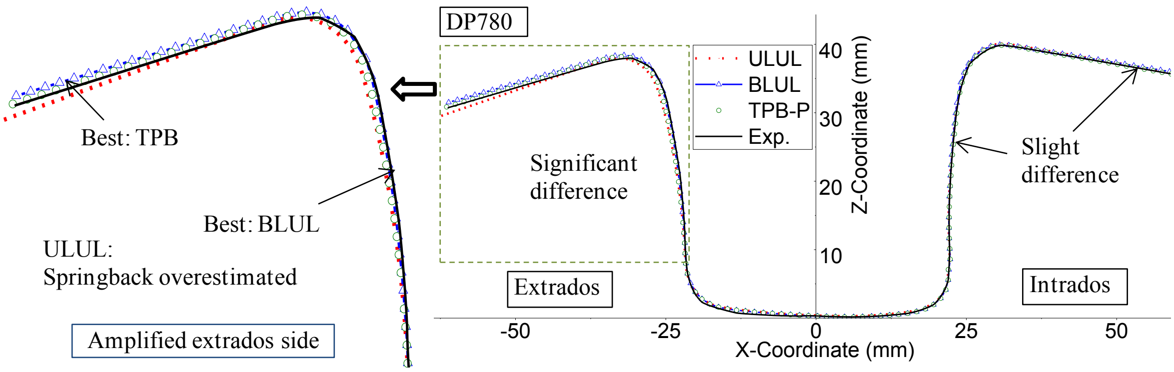

Figure 4-22 Comparison of the measured section shape and the predicted results based on different elastic modulus degradation.

Figure 4-22 shows the experimentally measured central sectional shapes of the DP780 curved-flanging channel after springback as well as the different predictions based on the elastic modulus measurement type. In the extrados side, the TPB-P loading strategy appears to be the best for angular springback prediction and BLUL best for sidewall curl. It is clear that there is a significant difference between the predictions in the extrados side but only slight in the intrados. This might be because the scattered stress field distribution (shrink) in the extrados side after forming process but centralized stress field (stretch) in the intrados side, as shown in Figure 4-23. The scattered stress distribution indirectly induces the springback and should be more sensitivity and complicate to prediction compared to the centralized stress field.

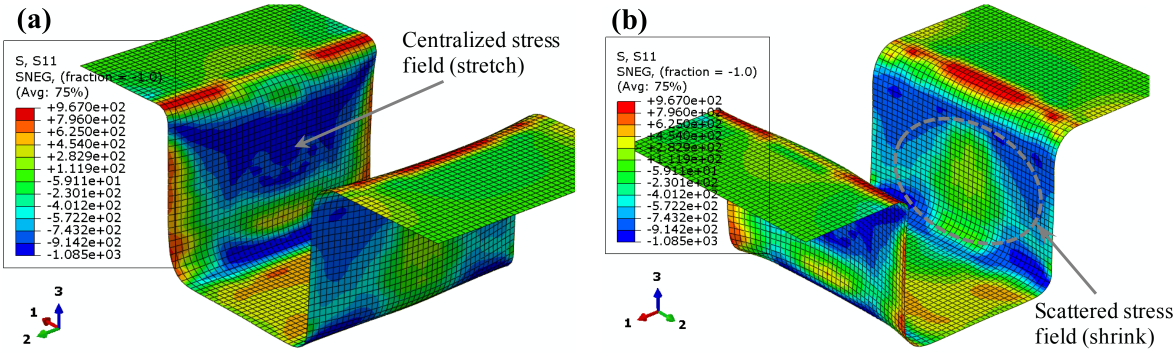

Figure 4-23 Transverse stress field distribution after forming process: (a) intrados side (b) extrados side.

Figure 4-24 compares the detailed experimental springback angles and sidewall curls with the predicted results based on different elastic modulus degradations obtained from the different loading strategies. In the extrados side, as shown in Figure 4-24a, the uniaxial loading strategy (ULUL) overestimates the angular springback but significantly underestimates the sidewall curl. BLUL and TPB-P seem to very well capture the angular springback and the former better predicts the sidewall curl. For the intrados side, as shown in Figure 4-24b, all the loading strategies lead to predicted springback angles and sidewall curls in good agreement with each other and with the experimental measurements, although the sidewall curls based on ULUL and TPB-P are slightly underestimated.

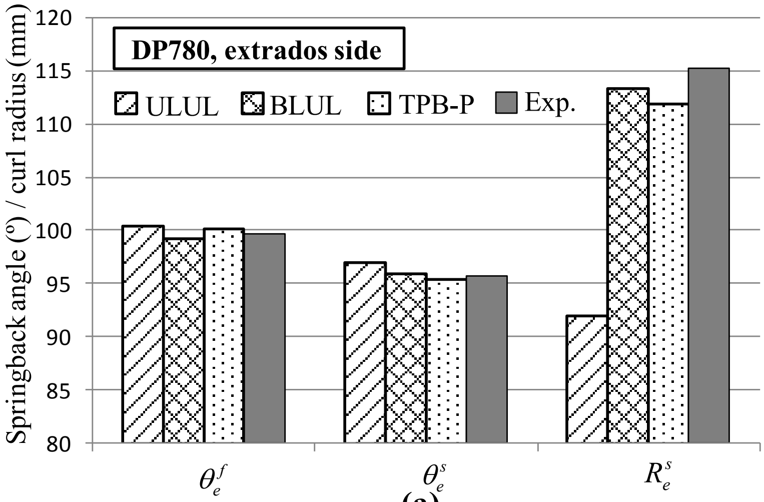

(a)

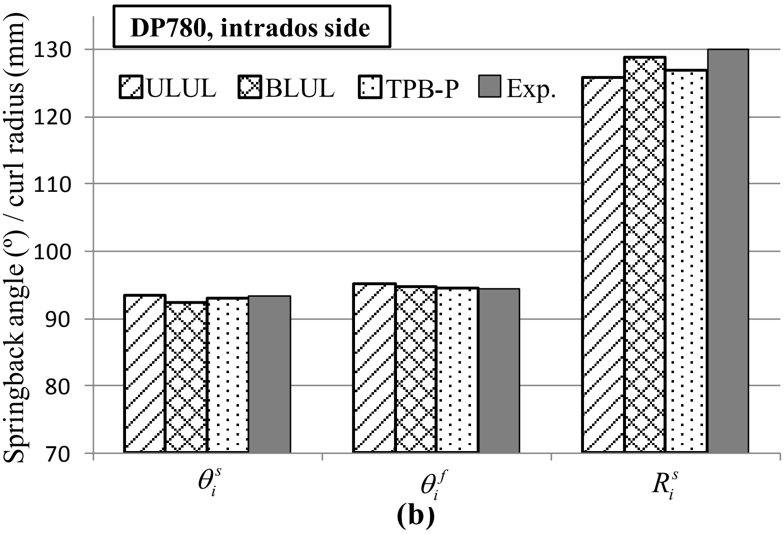

Figure 4-24 Experimental and predicted angular springback and sidewall curl of DP780 curved-flanging part: (a) extrados side (b) intrados side.

As demonstrated in Section 4.5.1, the determination of the elastic modulus degradation is sensitive to the loading strategies. However, it is difficult to deconvolute the coefficients describing the modulus degradation. The reason is that the relationship between springback and elastic modulus degradation is not simply proportional because it is affected by the nonlinear geometry of the part, material complexity, strain path changes, friction and other factors. For example, the frictional behaviour was simplified in numerical simulations by adopting the classical Coulomb's law in this work. But in fact, the frictional behaviour is very complicated, as it is influenced by many factors such as the tools and lubricant properties, process condition and environment. Therefore, it is important and necessary to further study the sensitivity analyses of various factors on springback prediction.

4.6 Partial conclusion

In this Chapter, the identifications of material parameters for basic mechanical properties, yield functions and hardening models are performed as well as the calibration and verification of the constitutive models. In order to identify ways to improve the description of nonlinear elastic behaviour of DP steels under different loading strategies, three mechanical tests, i.e., the uniaxial and biaxial loading-unloading-loading cycle tests, and the proposed three-point bending tests with prescribed pre-strained sheets, are used to determine the elastic modulus degradation with the increase of plastic strain. The springback of the curved-flanging test is adopted to evaluate the determination of the elastic modulus degradation. The main conclusions are as follows:

- The yield function Yld2000-2d accurately captures both yield stress and r-value directionalities in uniaxial tension while the other yield criterion Hill'48 is limited to describe the anisotropy of stress and strain simultaneously.
- The HAH model captures well the complex material behaviours including the Bauschinger effect, transient hardening with high rate and permanent softening. The IH model always overestimates the stress after load reversals, particularly at the onset of load reversals. The IHKH model captures the Bauschinger effect, giving a better description of the flow stress under load reversal than the IH model. However, it still cannot reproduce the permanent softening.
- The mechanical measurements of the nonlinear elastic modulus degradation of the DP steels are sensitive to the loading strategy as well as the determination of the initial elastic modulus. Among the three test methods considered, the highest elastic modulus degradation was obtained with the uniaxial loading strategy and the lowest with the biaxial loading strategy. The three-point bending test leads to the highest initial elastic modulus.
- The effect of cycling, which occurs at regular pre-set values of plastic strains, has virtually no influence on the decrease of the elastic modulus.
- The general uniaxial loading strategy leads to overestimated angular springback and underestimated sidewall curl in case of curved-flanging test (CFT). The biaxial loading strategy is associated with a better sidewall curl prediction compared to the other methods. The proposed TPB-P appears to be a good alternative method to determine the nonlinear elastic material behaviour since it leads to good predictions of the springback angles.

Chapter 5

Metal forming processes: Experiments and simulations

5.1 Introduction

The shape change after the forming process is driven by the release of the stored elastic energy during the tool removal. Compared to mild steel, AHSS and AA are more prone to this geometrical deviation because of the relatively high level of elastic deformation during the forming process. Recently, there has been growing interest in twist springback, which is considered as more complex compared to 2D springback (e.g., angular change and side wall curl).

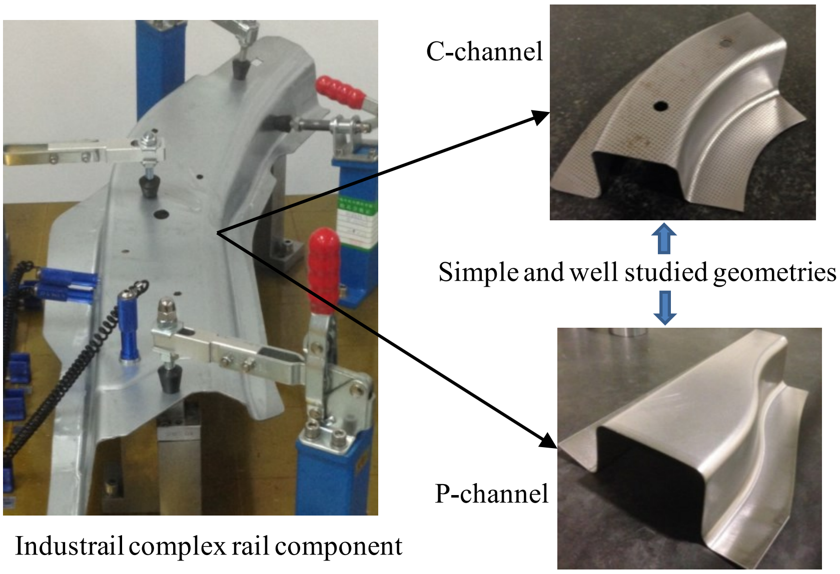

Figure 5-1 Simple and well-studied geometries for industrial channel components with complex shape.

In this work, in order to reduce the complexity in multivariate data structures, as shown in Figure 5-1, two characteristic experimental benchmarks in deep drawing of dual-phase steel sheet, which lead to particularly pronounced twist springback characteristics, were developed as well as their numerical models. Their geometries are relatively simple and well-studied but representative enough of more complex drawn parts in the automotive industry. In addition, an industrial automotive structure (see Figure 1-3b), i.e., a typical asymmetric aluminium alloy thin-walled tube, also having evident twist springback phenomenon after multi-stage bending, was addressed as one of the study subjects.

5.2 Deep drawing of DP steel sheet

5.2.1 Torsion moment-twist angle relationship for open-sectional channels

Twist springback is caused by torsion moments within the cross-section of the part, and the logical consequence is the different rotations of two cross-sections along their axes (Dezelak, et al., 2014). Torsion moment is induced by unbalanced plane residual stresses in the flange, side wall and web of the part. In the work of Takamura et al. (2011), the torsion moment and twist angle relationship for a sheet, subjected to curved channel deep drawing processes, has been analysed and discussed. By means of the numerical-analytic method, the calculation of the torsion moment T is given by

$$T = \sum_i \tau_{LC,i} \cdot \rho_i \cdot A_i \tag{5.1}$$

where i is the index of the quadrilateral domain generated by cutting the brick elements by the cross section, $\tau_{LC,i}$ is the stress component in the section local coordinate system shown in Figure 5-2, with L and C denoting the longitudinal and circumferential directions, respectively. The radial direction is defined to be that of the vector from the centroid of the cross section to a point in the material. ρ_i the distance between the quadrilateral domain and the centroid, and A_i is the cross-sectional area of the quadrilateral domain.

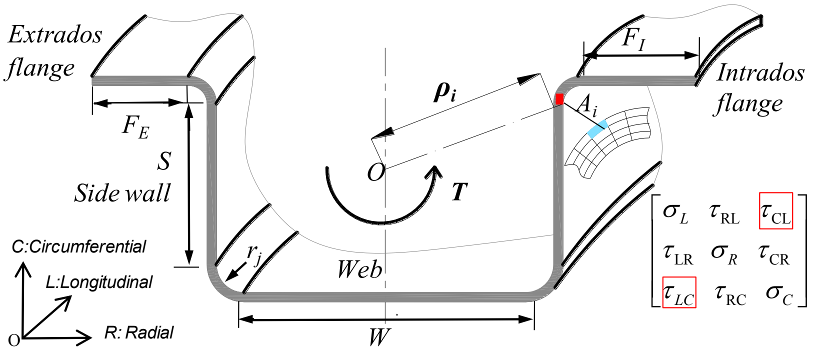

Figure 5-2 Physical quantity used for the calculation of torsion moment.

For the present open section structure in this work, the twist rate $d\varphi/d\theta=\varphi'(\theta)$ is assumed to be the same for all sections and linked to the portion of torque taken by each through the stiffness relation

$$\varphi'(\theta) = \frac{T_i}{G_i J_{i,\theta}},\ i = 1,\cdots n, \tag{5.2}$$

where G and J are shear modulus and torsion constant, respectively. In the case of C-channel, the torsion constant of a particular cross section can be decomposed into two parts: J_E and J_I taken by the extrados stretching part and the intrados shrinking part, respectively. The torsion constants are given by

$$J = \alpha\left(F + S + \frac{1}{2}W\right)t^3 + \sum_j \beta \frac{\pi}{2} r_j t^3 \quad \text{in which} \begin{cases} F = F_I \Rightarrow \mathrm{J}_I \\ F = F_E \Rightarrow \mathrm{J}_E \end{cases} \tag{5.3}$$

where F_E, F_I represent length of extrados and intrados flange respectively. S, W, r_j, t denote side wall length, web length, radii and thickness, as shown in Figure 5-2. α and β are dimensionless functions of the aspect ratio between wall length and thickness. For sheet metals, the value generally should be close to 1/3 when this ratio is larger than 10. In this case, α and β values can be set to 1/3 and 0.3, respectively. According to eq. (5.3), the difference of torsion constant depends primarily on the flange length. This is due to the non-uniformed metal flow between extrados stretching and intrados shrinking.

Using the assumption of constant twist rate and eq. (5.2), the ratio of the torsion moment ratio for extrados stretching part to that of intrados shrinking, η, is given by

$$\frac{T_E}{T_I} \simeq \frac{J_E}{J_I} = \delta, \quad \begin{cases} \delta \in (1, +\infty),\ \text{Positive twist} \\ \delta = 1,\ \text{no twist} \\ \delta \in (0,1),\ \text{negative twist} \end{cases} \tag{5.4}$$

In the case of $\delta_r \in (1, +\infty)$, the extrados total torsion moment is larger than the intrados total torsion moment, and positive twist will occur in the section. Similarly, negative twist will occur for $\delta_r \in (0,1)$. For the case of $\delta_r = 1$, the extrados and intrados metal flow lead to a moment balance. This means that there is no additional torsion moment and no twist after forming.

5.2.2 Definition of twist springback

According to Pham et al. (2014) and Bernert et al. (2010), the twist intensity is characterized by the ratio of the angle made between the end sections to their distance. The angle between the bottom edges of the end sections was considered. This means that the twists of the side wall and flange were ignored. In addition, for irregular shaped products with asymmetric or more complex cross sections such as the multi-step and multi-curvature sections, it is difficult to define a unique and objective rotating angle to indicate the twist distortion between two sections because of the global shape change of the whole product. For example: the springback of propeller blade. Therefore, in this work, a more comprehensive evaluation of twist springback with respect to the direction of the central principal inertia axes in a longitudinal cross-section is proposed, since this evaluation represents a global shape change of the whole cross section. Moreover, it can be a universal twist evaluation suitable for different complex products such as multi-curvature products.

The global twist angle is defined by the rotation angle of the principal axis of inertia for the cross-section before and after springback. It can be given by

$$\varphi = \cos^{-1}\left(\frac{\mathbf{i}\cdot\mathbf{j}}{|\mathbf{i}||\mathbf{j}|}\right) \tag{5. 5}$$

where **i**, **j** are the principal axis of inertia for the cross-section before and after springback, as shown in Figure 5-3. The rotation of vectors clockwise in the coordinate system is considered as the positive direction. For the calculation of the section properties, the thickness changes of the drawn part are neglected due to the relative small changed value. In other words, the section thickness is assumed to be constant after forming.

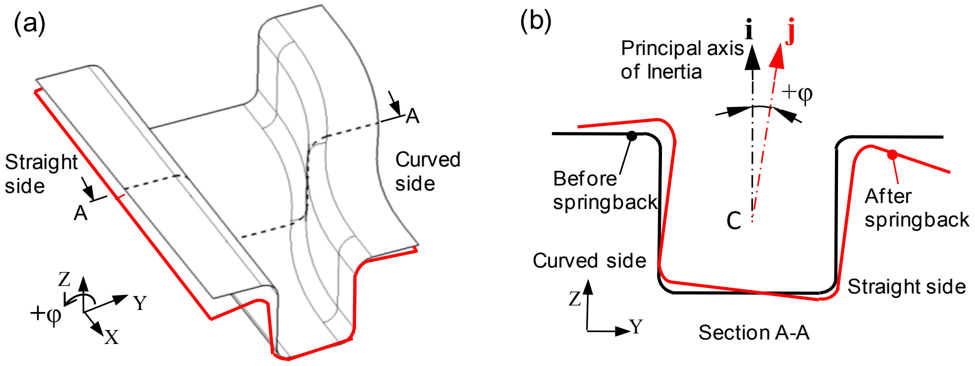

Figure 5-3 Definition of the global twist angle.

The relative twist angle is calculated by comparing the global twist angles of selected section with respect to the reference section. It can be given by

$$d\varphi_i = \varphi_i - \varphi_r \tag{5. 6}$$

where φ_i and φ_r are the global twist angles of selected cross section and the reference cross section respectively.

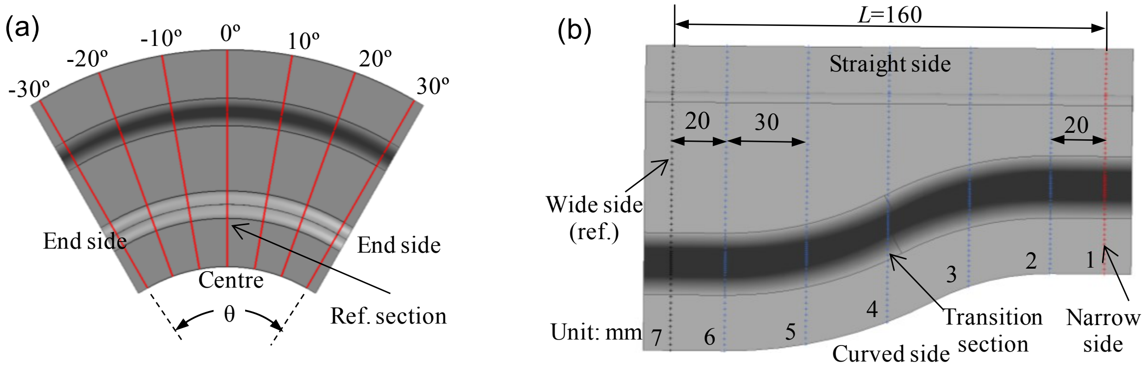

Figure 5-4 Measurement of cross-sections: (a) C-channel (b) P-channel.

The representative measured cross sections for the C-channel and the P-channel are illustrated in Figure 5-4. They were cut along the curvature of the longitudinal direction for C-channel and along the straight longitudinal direction for P-channel. The central section (0°) and the wide section (No. 7) were selected as the reference for the calculation of relative twist angle of C-channel and P-channel, respectively.

5.2.3 The experimental benchmark design

5.2.3.1 Design of experimental die set and forming conditions

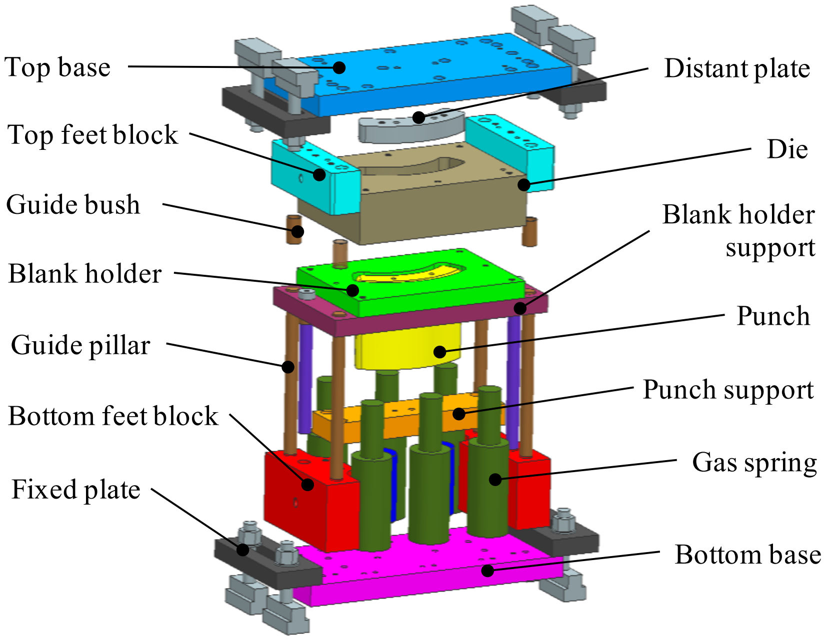

Figure 5-5 Illustration of designed experimental die set.

The experimental die set, as shown in Figure 5-5, was designed with almost all the basic characteristics of industrial tools. In order to obtain the smallest possible blank holder force variation during the deep drawing process, nitrogen gas springs are used. More detailed information on process parameters are shown in next Section. The die set is a flexible and universal design, which may support a series of benchmarks corresponding to similar deep drawing outline geometries.

5.2.3.2 Forming conditions

The forming equipment is a SHIMADZU universal tension-compression machine with a maximum capacity 1000 kN. The forming parameters are listed in Table 5-1. Inverse-install moving die-set was employed to reduce the vibration of the blank holder. In order to ensure accurate and robust value of blank holding force, nitrogen gas springs with the initial/maximum force of 90/144kN were used.

Table 5-1 Main process parameters of deep drawing.

No.	Parameters	Values
1	Total stroke of deep drawing, mm	40
2	Drawing velocity, mm/min	10
3	Amount of lubricant, g/m^2/side	10-12
4	The quantity of nitrogen gas spring	6
5	Initial/maximum blank holder force, kN	90/144
6	Final press contact pressure, MPa	10
7	Die clearance ratio	1.125

In sheet metal forming, the friction between two surfaces in relative motion can be reduced by lubricating the surfaces. The most common lubrication type in deep drawing of AHSS sheet is mixed lubrication, in which the lubricating media thickness allows contact between the peaks of the tool roughness and the work-piece surface. In order to obtain a uniform lubrication and analyse the effect of lubrication on springback, several types of lubricant condition were employed under the same process configuration. More detailed descriptions can be seen in next Chapter, Section 6.3.1.3. In this work, mineral-base semisolid grease (penetration at 25ºC: 265-295) is mainly employed. The amount of lubricant is about 10-12 g/m^2/side listed in Table 5-1.

5.2.3.3 C-shaped channel (C-channel)

A non-axisymmetric deep drawing benchmark, namely C-channel, can be obtained by sweeping a constant U-channel section along a curved guide. The geometry of the curved channel employed in this study is schematically shown in Figure 5-6. The central curved area has a radius of 125 mm with an angle of 60 degree. The drawing height is 40 mm, and the shoulder radius is 6 mm.

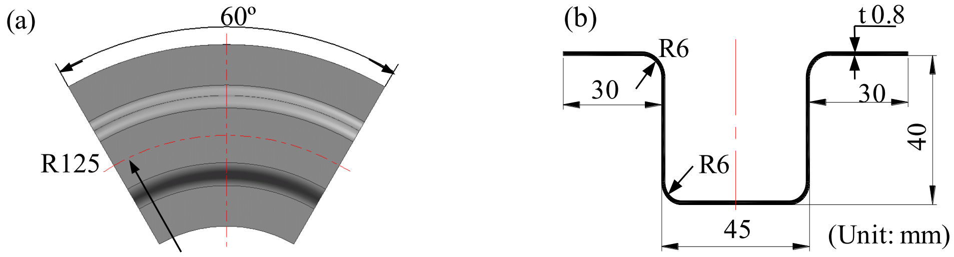

Figure 5-6 Geometry of C-channel model: (a) longitudinal-section (b) circumferential-section.

The design of pierced parts to control the initial blank position is presented. This feature allows the possibility of adding two pilot holes in the punch (see Figure 5-7), which can be used as reference points for blank positioning and boundary constraint point for initial blank determination.

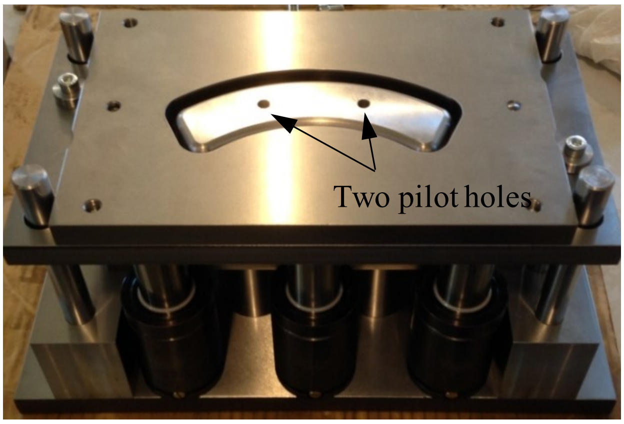

Figure 5-7 Experimental lower die set with the punch and two pilot holes for C-channel.

Twist springback commonly occurs in this type of channel due to the unbalanced stress distribution in the intrados and extrados of this part when forming the curvature along the longitudinal direction.

5.2.3.4 P-shaped channel (P-channel)

An asymmetric deep drawing benchmark with a variable cross-sectional shape, which also leads to a particularly pronounced twist springback characteristics, was developed. The main geometry of P-channel is shown in Figure 5-8. It is designed as a U-shaped channel with varied width sweeping along the longitudinal direction. The section widths are different and kept constant in the both ends but varied through a smooth transition in the middle. Forming this type of channel normally result in considerable twist springback due to its asymmetric geometry and residual stress distribution.

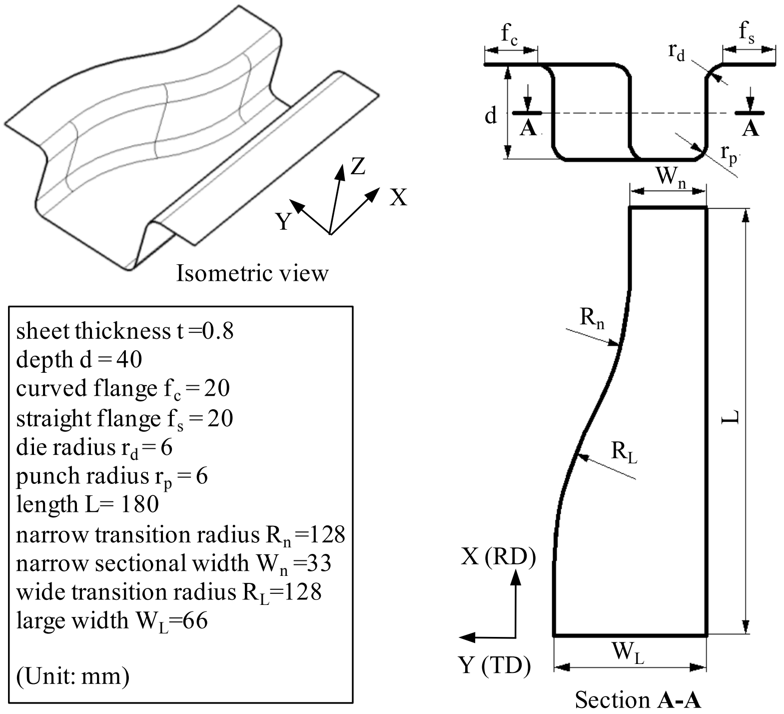

Figure 5-8 The geometries of P-channel.

Figure 5-9 Experimental lower die set with punch for P-channel.

Figure 5-9 shows the experimental lower die set with punch. Generally, tools with high hardness are required for cold working application to prevent the tool wear. A high hardness tool is also vital to minimize tool deformation during the forming process. A drawback of a high hardness level is that the tool material becomes more brittle. In this work, the material of the forming tools (for the die, punch and blank holder) is Vanadis 4 Extra with 290HB hardness. This means that the tool wear or tribological condition of the tools can be relatively consistent and the wear of tools can be ignored.

5.2.4 Digital image correlation (DIC) technique

In this work, a non-contact optical measuring system (also known as digital image correlation DIC), was used to obtain the geometry and deformation of the formed part. The DIC technique is important to assess the deformation of the drawn parts, such as the distribution of minor and major strain, thickness reduction, and shape deviation. It also provides an efficient method to compare simulation and experimental results. For example, the deformation path of selected trace grid points can be obtained using this technique for the identification of the friction coefficient in the simulation model.

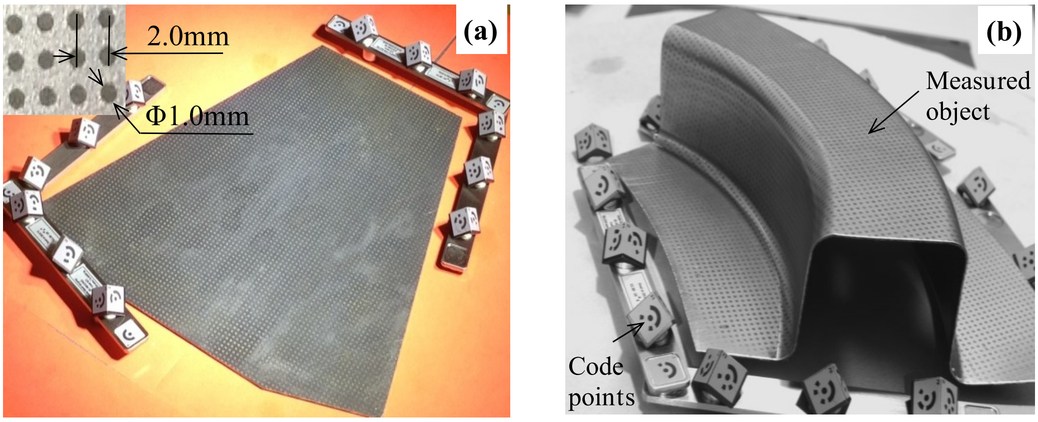

Figure 5-10 The application of digital image correlation technique: (a) Measurement of regular point pattern on the initial blank surface (b) measurement of deformed part with grids.

Grid pattern marking can be created using electrolytic method. Prior to forming, a regular grid pattern was marked on the surface of the initial blank by this process. As shown in Figure 5-10a, standard grid distance of 2.0 mm and grid diameter of 1.0 mm were used in this work. After the forming process of the measuring object, several images were recorded with the ARGUS 5M system, in order to acquire the points positioning from different angles. For the automatic spatial orientation of the individual images, calibrated objects with coded points were positioned close to (or on) the measuring object, as shown in Figure 5-10b. The 3D reconstruction of the final measuring object was then obtained/computed using the photogrammetric methods included in the ARGUS software.

5.2.5 Finite element modelling

5.2.5.1 Numerical simulation

FE-simulations of the forming process and springback were performed with the commercial code ABAQUS. The dynamic-explicit time integration scheme (see Figure 5-11a) was used for the simulation of the forming process, and implicit time integration for springback. The elastic-plasticity constitutive models described in the previous sections were implemented into ABAQUS through the user subroutines VUMAT/UMAT. The implementation algorithm and procedure of the HAH model is referred to Lee et al., 2012a. The blank was discretized with an average size of 1.0×1.0mm quadrilateral shell element (S4R), with 11 integration points through the thickness. A convergence study yielded that this spatial discretization was sufficient. The 4-node 3-D bilinear quadrilateral discrete rigid elements (R3D4) were selected to describe the discrete dies. The tool radii were discretized with a minimum of 6 elements along the radius. It is noted that the strain rate effects on mechanical behaviours of DP steels were ignored. The virtual forming velocity was scaled to 400 mm/s in FE model to improve the computing efficiency. The influence of this scaling was negligible since the kinetic energy was at most 1% of the internal energy for the whole model, as shown in Figure 5-11b.

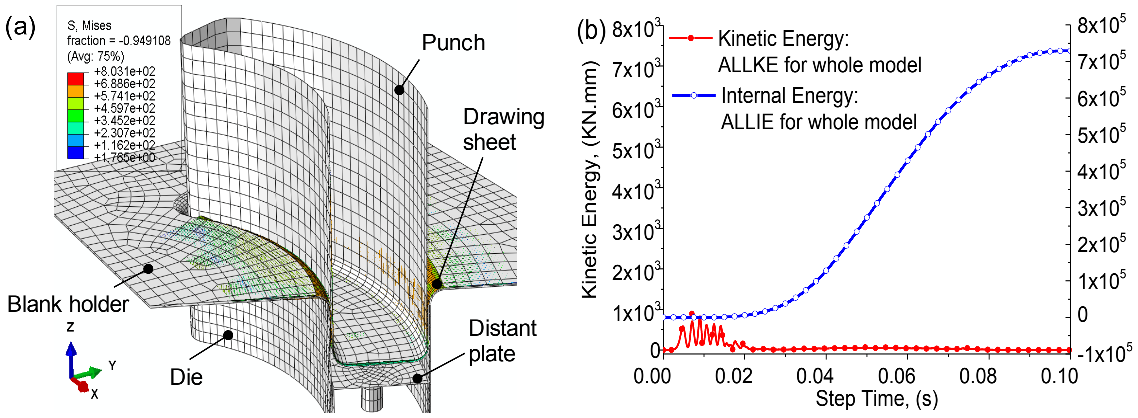

Figure 5-11 (a) Finite element model of C- channel rail benchmark (b) The internal and kinetic energy of history output during the forming process.

The springback process was performed in only one step. All the tools are removed simultaneously and let the blank sheet to attain equilibrium. The stress and internal variables were imported from the end of the forming stage. Implicit global time integration with the UMAT subroutine was used to simulate the springback process.

5.2.5.2 Determination of initial blank shape

Up to now, many initial blank design methodologies have been proposed in the literature to determine optimum initial blank shape profiles for diverse constraints and objective functions. These methods include ideal forming (Chung, et al., 2000), backward tracing methods (Ku et al., 2001) and so on. One-step formability analysis, also known as Inverse Approach (IA), is an inverse forming procedure, as opposed to traditional incremental finite element method (FEM) which simulates the resulting shapes starting from a blank. As shown in Figure 5-12a, the positions of material points in the initial flat blank are determined by an iteration procedure. The first estimation can be obtained simply by a vertical projection of the nodes onto the horizontal plane, and then an implicit Newton–Raphson algorithm is used to modify the initial nodal positions in order to satisfy equilibrium in the final work piece. The deformation theory of plasticity based on the assumption of proportional loading is used to obtain an integrated constitutive law. The actions of the tools are replaced by total (but unknown) nodal forces without taking into account the time dependent contact conditions. The kinematic relations should be briefly described based on some assumptions (Li, et al., 2010). As shown in Figure 5-12b, the initial and final position vectors of a material point q can be expressed, with respect to point p on the mid-surface of C, by a generalized Kirchhoff assumption. The whole process can be described as follows:

1) The geometry and the mesh of final work piece C including mesh element type, mesh size and its variation are given;
2) The basic material property parameters, e.g., elastic modulus, yield stress, hardening exponent, strength coefficient, anisotropy coefficients and thickness t_0 of initial sheet blank, are used as input;
3) The forming conditions such as drawing direction, blank-holder force (BHF) and friction parameters, are established;
4) The boundary constraints, i.e., springback match points and point to point

constraints, are created;

5) The nodal positions in the initial flat blank C_0, and the distributions of thickness, strain, stress, etc., are calculated in the final work piece.

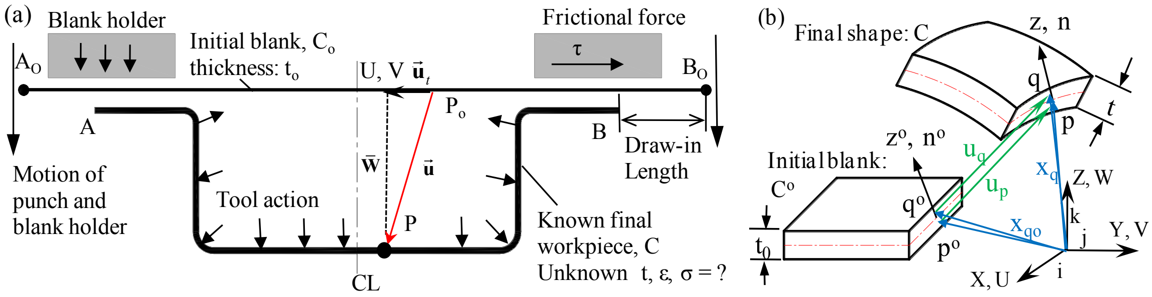

Figure 5-12 Illustration of one-step formability analysis: (a) general description in sheet metal forming (b) kinematic description of thin shell.

Li et al. (2010) showed that a deformable body in equilibrium state must satisfy the principle of virtual work (abbreviated as **PVW**) as the necessary and sufficient condition for the stress field. Therefore, the discrete form of energy equation can be described as

$$W=\sum_{i=1}^{n}\left(\int_{V^e}\left\langle\varepsilon^*\right\rangle\{\sigma\}dV-\int_{V^e}\left\langle u^*\right\rangle\{f\}dV\right)=0 \tag{5.7}$$

where $\left\langle\varepsilon^*\right\rangle$ and $\left\langle u^*\right\rangle$ are the virtual strain and virtual displacement, $\{\sigma\}$ the Cauchy stress and $\{f\}$ the equivalent nodal force which is caused by the force between die and roughcast interaction through the friction resistance.

The kinematic relations should be briefly described based on some assumptions. As shown in Figure 5-12b, the initial and final position vectors of a material point q can be expressed, with respect to point p on the mid-surface of C, by a generalized Kirchhoff assumption. The inverse Cauchy–Green left tensor can be obtained as

$$dX_q^0=F^{-1}dX_q \quad \text{with} \quad F^{-1}=F_0^{-1}F_Z^{-1} \tag{5. 8}$$

and let

$$B^{-1}=F^{-T}F^{-1}=\begin{pmatrix} a & \mathrm{b} & 0 \\ \mathrm{b} & \mathrm{c} & 0 \\ 0 & 0 & \lambda_3^{-2} \end{pmatrix} \tag{5. 9}$$

The eigenvalue of B^{-1} gives the two principal plane stretches λ_1, λ_2 and their direction transformation matrix *M*. Then, the thickness stretch λ_3 is calculated by the incompressibility assumption. Finally, the logarithmic strains are obtained by

$$[\varepsilon]=M\begin{pmatrix}\ln\lambda_1 & 0 & 0\\ 0 & \ln\lambda_2 & 0\\ 0 & 0 & \ln\lambda_3\end{pmatrix}M^T \tag{5.10}$$

In the one-step formability analysis, only the initial and the final configuration are compared. Therefore the elastic–plastic deformation is assumed to be independent on the loading path and a total constitutive law is obtained,

$$\begin{pmatrix}\sigma_{xx}\\ \sigma_{yy}\\ \sigma_{xy}\end{pmatrix}=\frac{2\bar{\sigma}(2+\bar{r})}{3\bar{\varepsilon}(1+2\bar{r})}\begin{pmatrix}1+\bar{r} & \bar{r} & 0\\ \bar{r} & 1+\bar{r} & 0\\ 0 & 0 & 1\end{pmatrix}\begin{pmatrix}\varepsilon_{xx}\\ \varepsilon_{yy}\\ \varepsilon_{xy}\end{pmatrix} \tag{5.11}$$

where $\bar{\varepsilon}$ and $\bar{\sigma}$ are the total equivalent strain and equivalent stress. The mean planar r-value $\bar{r}$ is obtained from three anisotropy coefficients: $\bar{r}=(r_0+2r_{45}+r_{90})/4$.

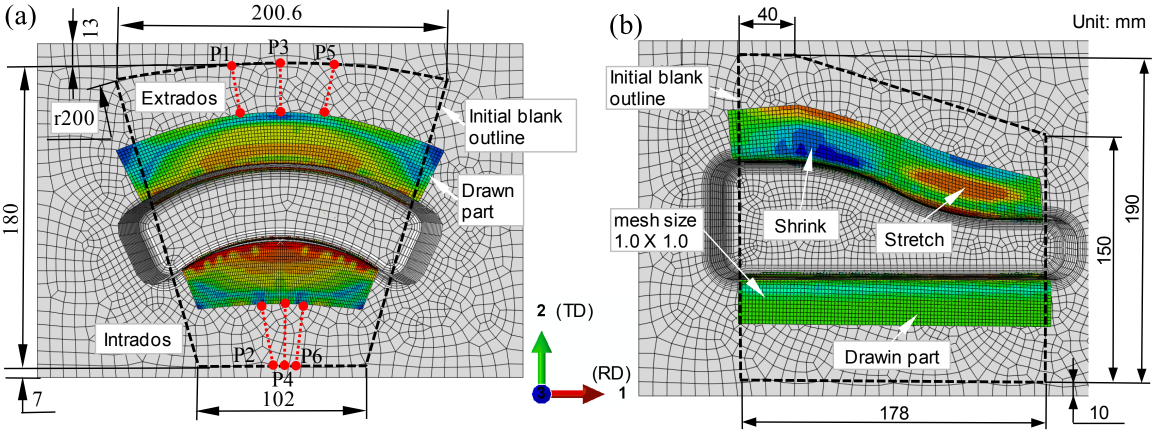

Figure 5-13 The location and geometry of initial blank shape: (a) C-channel (b) P-channel.

One-step formability analysis considering the springback match points and boundary constraint points to estimate the initial blank shape is fast and convenient, hence it is an attractive technique to reduce trial-and-error time and cost. In this work, the curved sides of the ideal initial blank shape were simplified to straight lines within the allowed forming and measurement criteria. The location and geometry of initial blank shape after simplified cutting is shown in Figure 5-13, in which the longitudinal 1-coordinate is along the rolling direction of the initial blank sheet.

5.2.5.3 Friction coefficient identification

As the authors previously have discussed, interfacial friction between blank and tools has a very significant effect in sheet metal forming. Indeed, industrial simulations mainly rely on the simple Coulomb frictional law, in which the frictional force is proportional to the normal force, and where the proportionality constant is the friction coefficient μ. The selection of friction coefficient is generally based on experience, or when experimental results are available, it can be used as a fitting parameter to obtain e.g. a correct draw-in length or punch force (Eggertsen, et al., 2012).

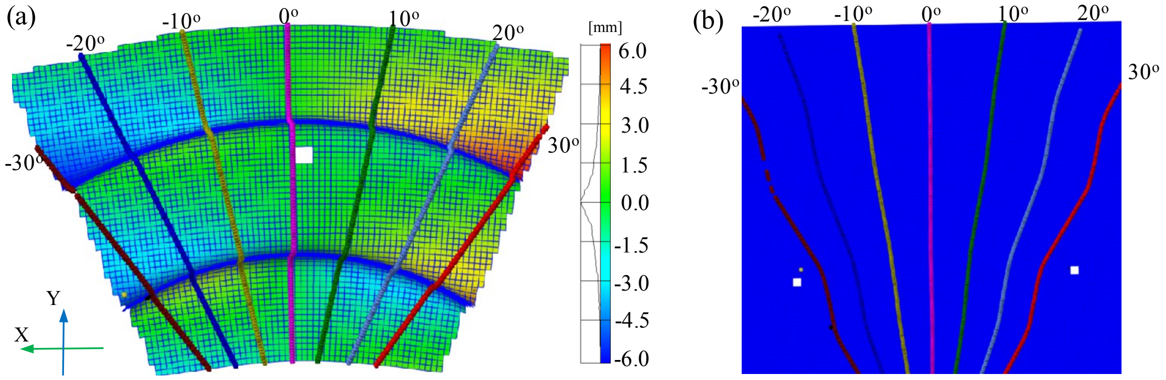

Figure 5-14 (a) Displacement distribution of grid points in X direction from experimental non-contact optical measurement (b) The shape of cross sections prior to deformation.

In this work, the friction coefficient was determined by correcting draw-in length of selected trace points. Figure 5-14a shows the displacement distribution of whole grids in X direction from experimental non-contact optical measurement. The maximum value was close to 6mm in the side sections. This means that the grids in the side sections have complex deformation path during the drawing process. It also can be observed that the shape of the cross sections at -30º, -20º, 20º and 30º is obvious non-linear evolution prior to deformation, as shown in Figure 5-14b. It can be more difficult to trace these section points and calculate the draw-in length. Therefore, the points at the end of sections -10º, 0º and 10º were chosen as trace points for draw-in length measurement, since they had an approximate linear deformation path, as shown in Figure 5-15a.

In the absence of any information about the true friction conditions, it is a important to perform an analysis in order to understand how sensitive the forming operation is to variations in the friction conditions. The current rail was analysed with friction coefficients of 0.05, 0.10, and 0.15, which are accepted values for similar steel-steel interfaces with lubrication (Emil et al., 2001).

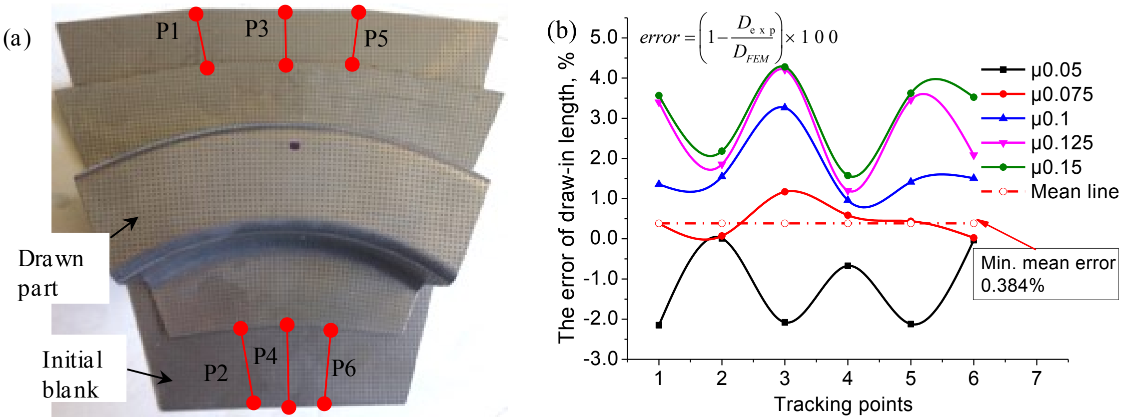

Figure 5-15 (a) Illustration of draw-in length of experimental parts (b) The error of draw-in length with tracking points under different friction coefficients.

The experimental and predicted results of draw-in length of selected trace points are listed in Appendix Table. B1. Compared to experimental results, the error of draw-in length under different friction coefficients are shown in Figure 5-15b. It can be observed that the friction coefficient leads to a significant effect on the forming results. The draw-in lengths of the selected trace points computed with a friction coefficient of 0.075 were the closest to the corresponding experimental results. The value of the minimum mean error was 0.384%. The logarithmic regression equations of the mean error for the draw-in length can be written as:

$$y = 3.471\ln(x) + 9.411 \quad (\mathrm{R}^2{=}0.996) \qquad (5.\ 12)$$

The friction coefficient leading to no mean error of the draw-in length was 0.066, which was set as the optimum friction coefficient for numerical modelling.

In order to analyse the sensitivity of yield function on friction coefficient identification, the draw-in lengths of the selected trace points computed with different yield functions were compared, as shown in Figure 5-16. No remarkable deflection was observed, and the value of maximum deflection was only 1.63% at the trace point 5. Therefore, the yield function does not seem to affect this kind of results.

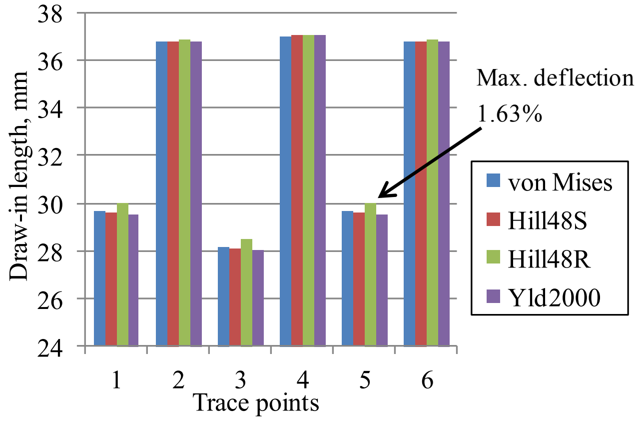

Figure 5-16 Comparison of draw-in lengths computed with different yield functions.

5.2.6 Experimental validation of numerical models

By means of the digital image correlation (DIC) technique, the experimental data can be compared easily with the numerical simulation results, in particular, the maximum in-plane principal strain and the twist springback angle. All simulation results were obtained by using the anisotropic constitutive models, i.e., the Yld2000-2d and the HAH model, and the nonlinear elastic modulus determined by the ULUL tests. The sensitivity of material constitutive model on the corresponding simulation results would be analysed and discussed in the next chapter.

5.2.6.1 In-plane strain

Figure 5-17 indicates that the experimental and predicted results of the maximum in-plane principal strain field of DP500 C-channel are in good agreement. Both results of the largest strain field are on the intrados sidewall close to the end section sides. All the locations of in-plane strain are on the outer layer in the thickness, i.e., the deformable sheet surface contacting with die surface. It is the same with the measured surface of DIC technique.

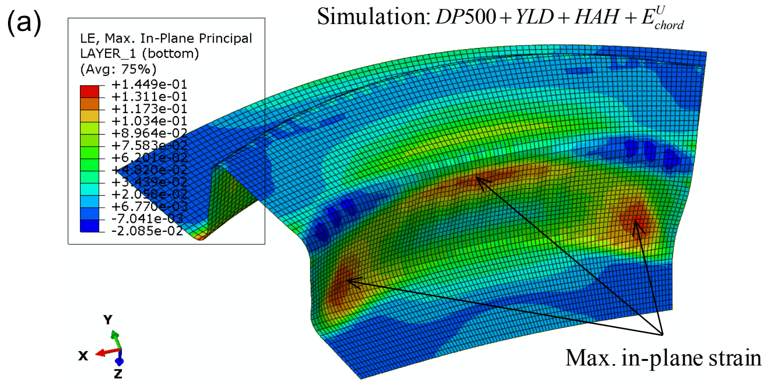

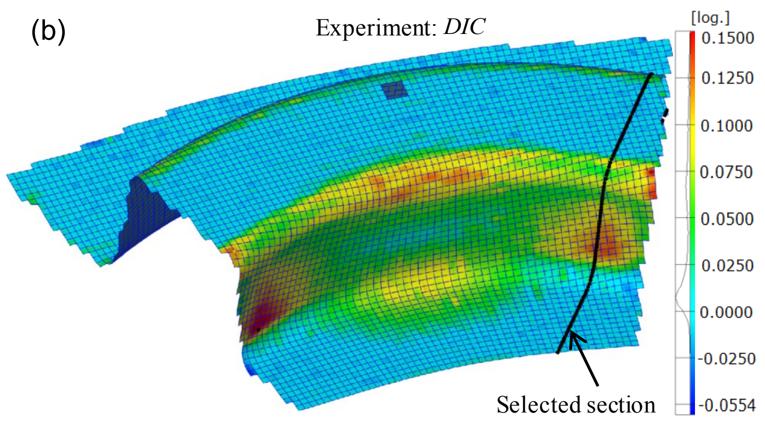

Figure 5-17 Comparison results of the maximum in-plane principal strain distribution of C-channel: (a) simulation (b) experiment.

The experimentally evaluated major strain distributions at the end section side and the corresponding predicted results are showed in Figure 5-18. The major strain seems to be well predicted by using the selected material constitutive models, although globally the numerical results are lower than the experimental result.

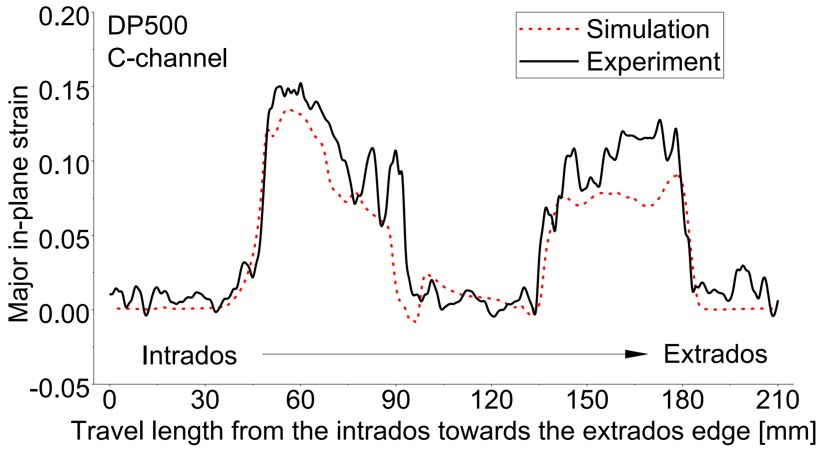

Figure 5-18 Comparison of the in-plane strain field of the selected cross section by DIC measurement and numerical prediction for DP500 C-channel.

Similarly, for DP780 P-channel, the comparison of the measured maximum in-plane strain field of the selected central cross section and predicted result are shown in Figure 5-19. The predicted in-plane strain seems slight underestimation compared to the DIC experimental results.

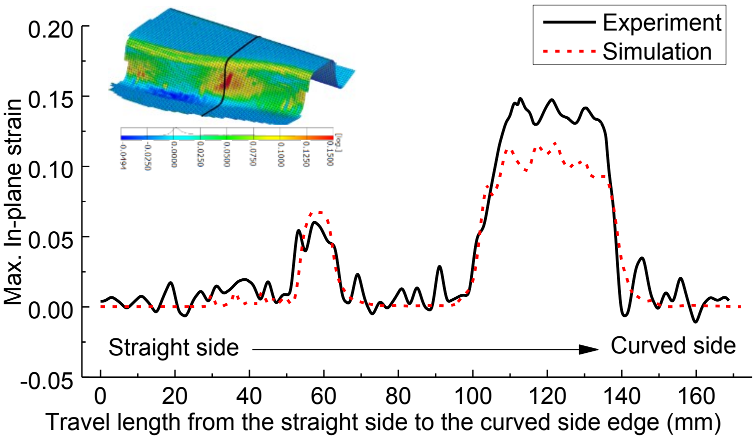

Figure 5-19 Comparison of the in-plane strain field of the selected cross section by DIC measurement and numerical prediction for DP780 P-channel.

Even though the simulated results for material flow are in reasonable agreement with the experiments, some significant differences exist between the computed and measured strain fields. For example, the discrepancy between the strains at the punch corner is remarkable, as shown in Figure 5-17. This might be due to the point pattern of the measured object and the lack of fitting accuracy of the deformed circles because of the severe strain variations. It also might be due to the deviation of the material description implemented into the simulation code. These discrepancies should be reduced or eliminated with the development of advance deformation measurement technology and more comprehensive material constitutive models.

5.5.6.2 Twist springback

For C-channel, as shown in Figure 5-20, the comparison of the simulated and experimental global twist springback angles in the longitudinal direction is in a good agreement. The maximum deviation of the global twist angle is 0.31° while it is 0.28° at the end section sides and 0.1° at the centre, as shown in Figure 5-20a. The maximum deviation of relative twist angle is 0.51° while it is 0.38° at the end section sides, as shown in Figure 5-20b. The twist springback from the centre to the end section side decreases slightly first and then increases gradually. Generally, the relative twist angle is enough to demonstrate the twist evolution among cross sections. Due to the global twist deformation of central section of the presented C-channel benchmark in the global coordinate system, the global twist angle was also applied to evaluate the global twist evolution. The choice is dependent on the geometric model of forming conditions and the measurement reference.

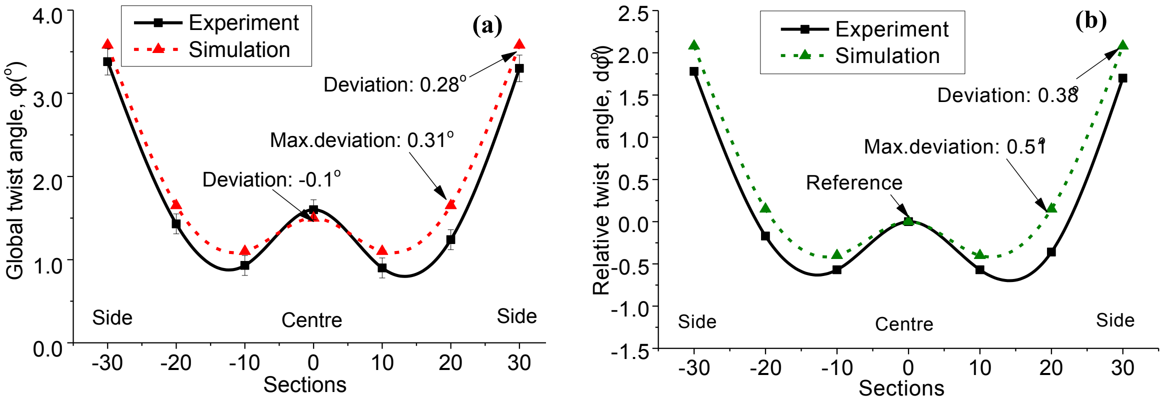

Figure 5-20 Comparison of twist springback of DP500 C-channel: (a) Global twist angle (b) relative twist angle.

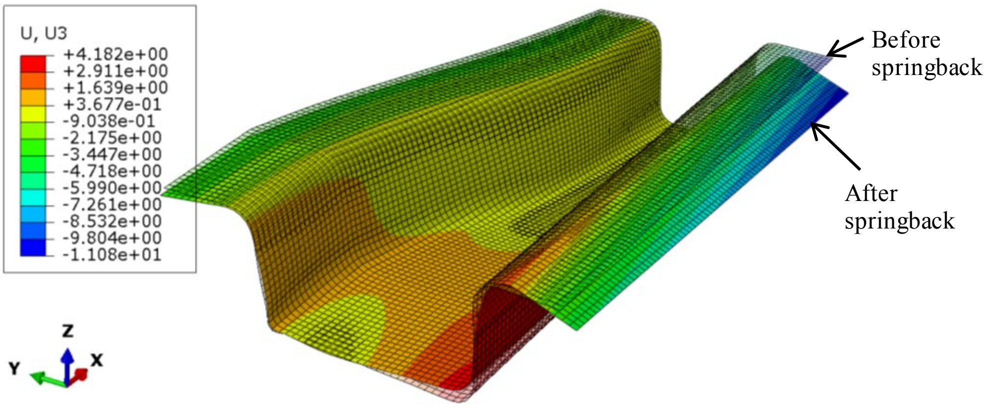

Figure 5-21 One predicted displacement springback distribution along the Z-direction.

For P-channel, DP780 steel sheet was selected to validate the prediction accuracy of twist springback by the developed FE model. Figure 5-21 shows one of the predicted results, i.e., displacement springback distribution along the Z-direction or 3-direction (U3). It is observed that the displacement of the flange along the straight side has a significant variation while that along the curved side is almost stable, indicating the occurrence of the twisting. The comparison of the predicted relative twist springback and experimental results is shown in Figure 5-22. The relative twist angle decreases fast initially in the narrow sections, then it starts slightly fluctuating in the sections located in the transition region, where the width of the cross section varies. After the transition region, it starts decrease again in the wide sections. The evolution of the predicted relative twist springback agrees well with the experiment. Although the predicted discrepancies still exist, e.g., the maximum deviation is 0.73° at the section 2, the validity of the finite element model is acceptable for the analysis of twist springback characteristics.

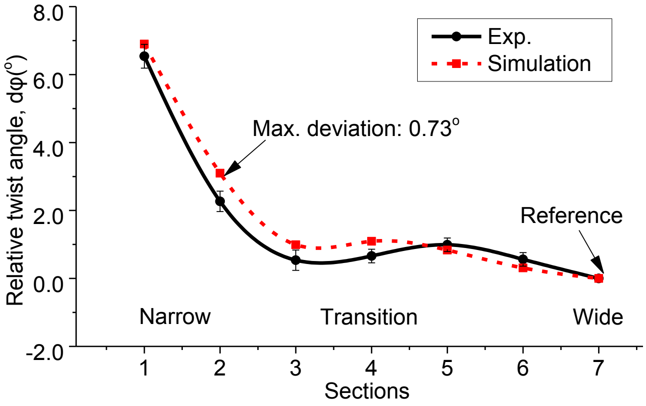

Figure 5-22 Comparison of the measured relative twist angle of the DP780 P-channel and simulation results.

5.2.7 In-plane stress analyses

In this section, special attention is paid to the in-plane stress analyses for the occurrence of twist springback caused by the release of the residual stress.

5.2.7.1 C-channel

In order to explore the source of twist springback, the analysis of in-plane stress state after forming was performed by slitting the flanges and side walls on the intrados and extrados. The stress states of some selected key positions on the flanges and side walls at top layer are illustrated in Figure 5-23. σ_1, σ_2 represent the stress in the longitudinal and transverse directions, respectively.

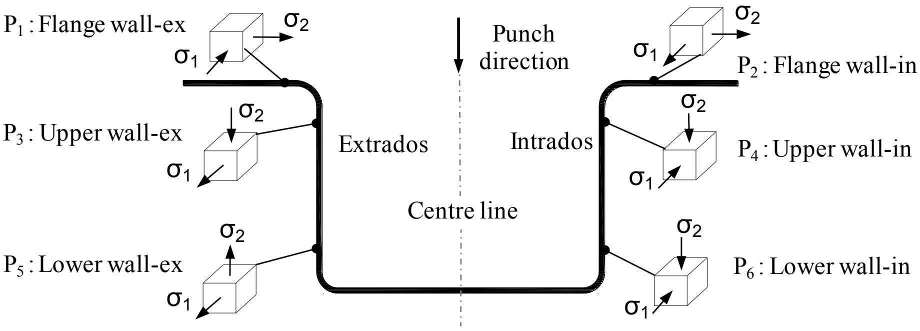

Figure 5-23 In-plane stress analysis of flange and side wall deformations for C-channel (top layer).

Figure 5-24a shows the global in-plane stress distribution of DP500 along the longitudinal direction (S11) on the top layer of the sheet thickness. The longitudinal stress on the whole locations of thickness are logically consistent. It can be observed that the extrados flange tends to shrink, inducing the compressive in-plane stresses, while the extrados side wall induces conspicuous tension stresses. This means that the loading path reverses through the extrados die radius. Similarly, a loading change also occurs on the intrados with the opposite stress distribution compared to the extrados, i.e., tension in the flange and compression in the wall. The global in-plane stress distribution in the transverse direction (S22) is shown in Figure 5-24b. In contrast to the longitudinal stress distributions, the transverse stress distributions on the extrados and intrados flanges and side walls are almost the same at the corresponding positions. It is approximately symmetric in light of the section centre line. The transverse stress field of the bottom and side wall near punch radius have weak influence on the analyses for twist springback due to its slight and discontinuous stress field, even if they are not the same and symmetric. The historic loading paths of side wall tracing points P3 and P4 (see Figure 5-23) in the longitudinal and transverse directions are shown in Figure 5-25a and Figure 5-25b, respectively.

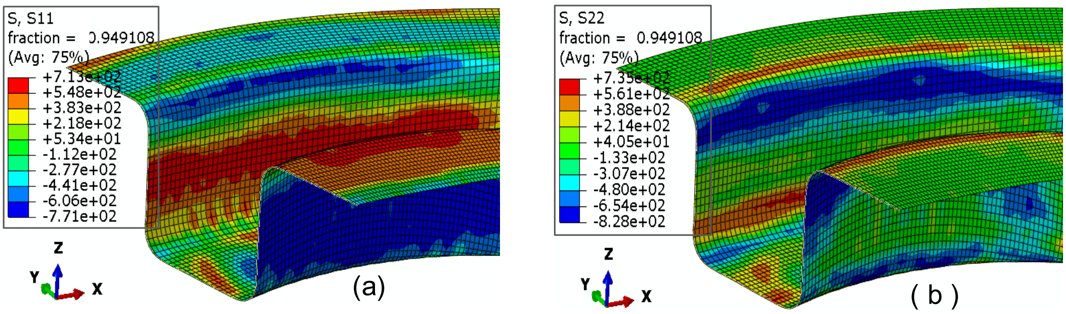

Figure 5-24 Global in-plane stress distribution of DP500 (top layer): (a) in the longitudinal direction (b) in the transverse direction.

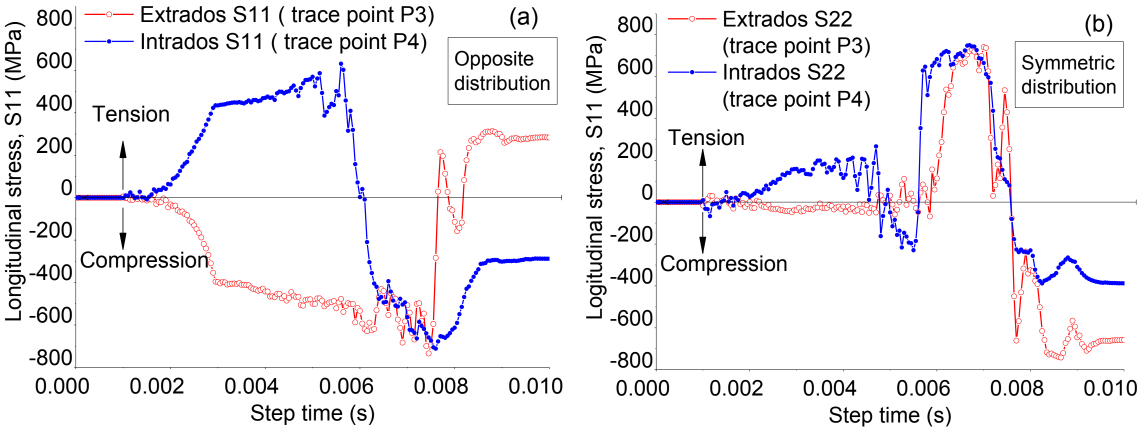

Figure 5-25 Historic loading paths of sidewall tracing points: (a) S11 in the longitudinal direction (b) S22 in the transverse direction.

5.2.7.2 P-channel

Compared to the asymmetric in-plane longitudinal stress distribution on the extrados and intrados sides of C-channel, the main asymmetric stress occurs in the curved side of P-channel. At the end of forming stage, the stress states of some selected key positions on the flanges and side walls at top layer are illustrated in Figure 5-26. σ_1, σ_2 represent the stress in the longitudinal and transverse directions, respectively. It can be observed that the transverse stress (S22) distribution has not changed from wide section to narrow section, and is symmetric in light of the section centre line. However, the longitudinal stress field on the curved flange and sidewall make a reversal from narrow section to wide section. For example, Figure 5-27 shows the global in-plane longitudinal and transverse stress distributions of DP780 on the top layer of the sheet thickness. The longitudinal stress distribution is significantly asymmetric on the curved transition sections.

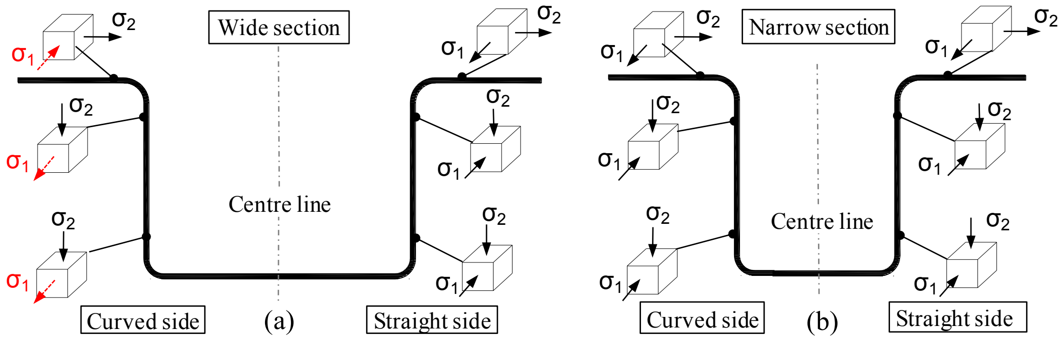

Figure 5-26 In-plane stress analysis of flange and side wall deformations for P-channel (top layer): (a) Wide section (b) narrow section.

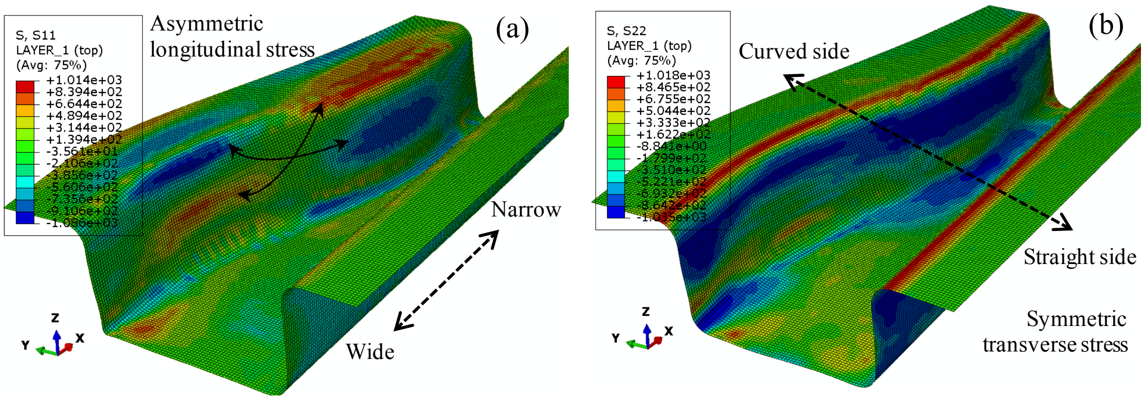

Figure 5-27 The global in-plane stress distribution of DP780 (top layer): (a) in the longitudinal direction (b) in the transverse direction.

5.2.8 Deformation analyses

5.2.8.1 C-channel

According to the above in-plane stress analysis, the longitudinal stress field S11 have a dominant influence on the twist occurrence. Meanwhile, the longitudinal stresses on the extrados and intrados side walls were considered, and those on the flanges were ignored since they make little effect on twist deformation. In this section, the bending moment for twist springback was analysed based on the longitudinal stress field of side walls. It was inspired by work of Tang et al. (2000) on the plastic-deformation analysis in tube bending. The springback analysis of C-channel deep drawing is similar to that of thin-wall tube bending, although they are different forming processes. Here, the analysis of bending moment for twist springback was performed by slitting the side walls on the intrados and extrados. Before springback, the extrados side wall induces the tension longitudinal stress since it relatively tends to stretch. This tension stress field are dominantly released and produce the reversal compressive stress field during the springback process. Therefore, the extrados side induces a positive bending moment (Me) due to the compressive longitudinal stress field. On the contrary, the intrados side induces a negative bending moment (Mi) due to the tension longitudinal stress field, as shown in Figure 5-28.

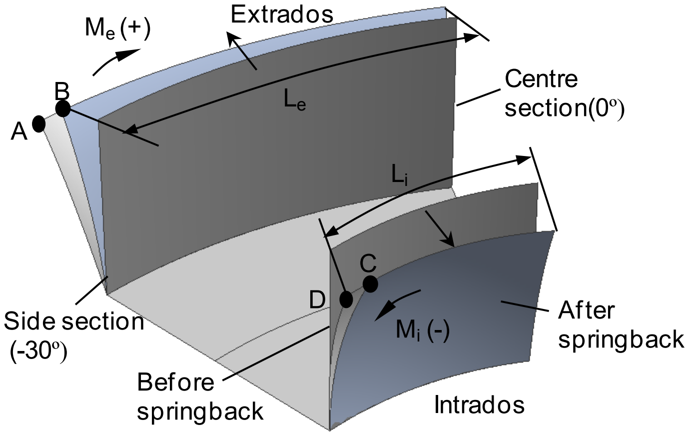

Figure 5- 28 Mechanism of twist springback occurrence.

Meanwhile, both side walls open outward and the circumferential curved lengths vary when the bottom web is assumed to be fixed. The circumferential length increases on the extrados and decreases on the intrados. However, the extension and contraction deformations do not occur on the extrados and intrados, respectively. In other words, the curve lengths, L_e and L_i, should be consistent before and after springback. Simultaneously, at the side sections, displacements occur from point A to B on the extrados and from point C to D on the intrados. These displacements may induce twist deformation. In addition, the different bending moments on the extrados and intrados intensify the twist deformation, because the positive bending moment on the extrados makes the decrease of the curvature of extrados side wall. And the negative bending moment on the intrados makes the increase of the curvature of intrados side wall. It can be validated by the curvature change of side walls measured in the experimental tests, as shown in Figure 5-29.

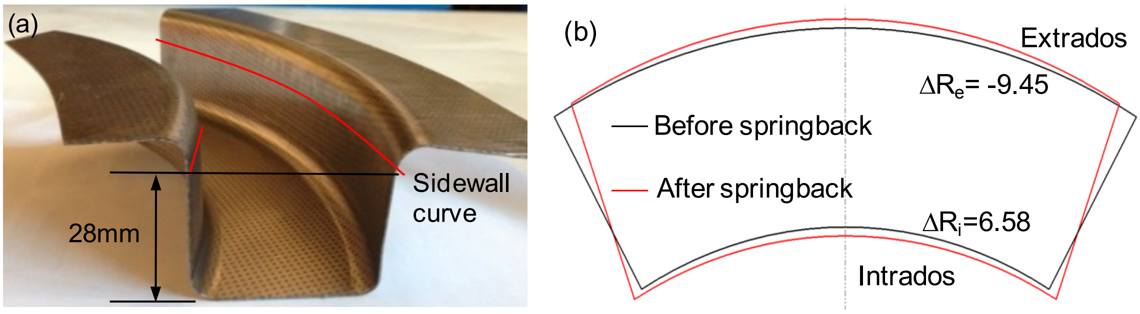

Figure 5-29 Side wall curvature change after springback: (a) the selected side wall position (b) the curvature radius variation.

The side wall curvature radius changes were obtained by DIC experimental tests and best-fit algorithm for curvature calculation. They were -9.45mm and 6.58mm on the extrados and intrados respectively. This evolution of the curvature adheres to the mechanism of twist springback. Therefore, the unbalance bending moments on the extrados and intrados and the incompatible geometric deformation caused by the springback of the side walls are the sources of twist springback in the proposed C-channel benchmark.

5.2.8.2 P-channel

Elastic recovery of torsion moment by uneven in-plane residual stress caused by the stretch and shrink flange and sidewall in the curved side of the P-channel is the main source of twist springback. According to the in-plane longitudinal stress distribution after forming (see Figure 5-27a), the twist tendency created from the release of the flange and sidewall residual stresses is illustrated in Figure 5-30.

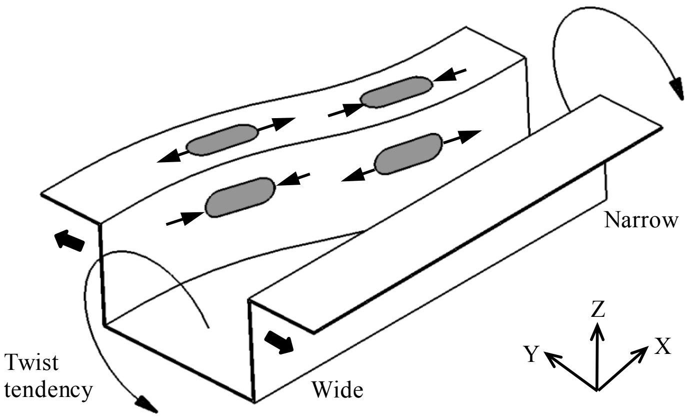

Figure 5-30 The twist tendency created from the release of the flange and sidewall residual stresses for the proposed P-channel

Figure 5-21 shows that the flange displacement along the straight side has a significant variation while along the curved side is almost stable, indicating the occurrence of the twisting. The global twist springback of the P-channel mainly occur at the narrow side, rather than the wide side. This is because the torsion stiffness or torsion constant of the wide section is larger than the narrow section. It means that the narrow section is less resistant to initiate twist than the wide section under the same torsion moment.

The magnitude of twist in an asymmetric channel will be determined by the relationship between unbalance stress on the part and the stiffness of the part in the direction of the twist. For example, the long, thin parts with low torsional stiffness have higher tendencies to twist.

5.3 Tube bending of asymmetric AA6060 thin-walled tube

In the last decade, the number of tubular aluminium frame components for automotive application has increased significantly due to its weight reduction and corresponding improvements in fuel consumption (Miller et al., 2001 and 2003). The aluminium tube components are best produced by extrusion, then cold formed to the required shape and finally are assembled to form a space frame. Among the types of tube forming processes, rotary draw bending is a very common, useful and flexible bending method due to its low production cost, variety of tooling options and process automation (Liu et al, 2012). However, a big technical hurdle in bending aluminium tube is the serious springback after release of the forming loads since its elastic modulus is much smaller than for steel

(Laurent et al., 2009). Moreover, in the case of tubes with open or asymmetric section, twist deformation often occurs during the bending process and it significantly affects the dimension accuracy of the product.

5.3.1 Mandrel rotary draw bending

Mandrel rotary draw bending (MRDB) for aluminium thin-walled tube includes three processes: bending tube, retracting mandrel and springback (Xue et al., 2015a). The tool setup in the initial position state for MRDB is illustrated in Figure 5-31. In bending process, pulled by bend die and clamp die, the extruded tube rotates along the grooves of bend die to the desired bending degree and the bending radius. Meanwhile, the pressure die is to apply enough pressure force and bending moment to the tube and push it against the wiper die tightly. The wiper die, the vulnerable part with very thin feather edge, is often placed behind bend die to prevent the tube from wrinkling. Among the above tooling, mandrel with flexible cores is positioned inside the tube to provide the rigid support and reduce the cross section distorting.

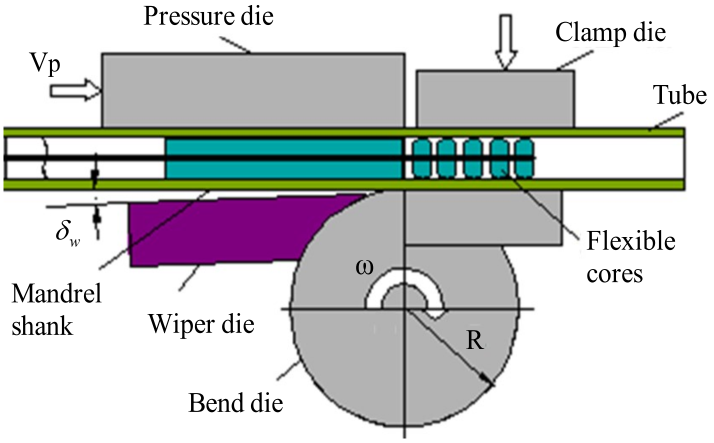

Figure 5-31 Tools setup and illustration of mandrel rotary draw bending process.

5.3.2 Definition of twist springback

In this work, twist springback of the asymmetric thin-walled tube (see Figure 5-32) includes two main codes of deformation behaviours. In the longitudinal direction, the amount of springback can be expressed as the value of springback angle

$$\Delta\theta = \theta - \theta' \tag{5.13}$$

where θ and θ' are the bending angles before and after springback, respectively, as shown in Figure 5-32a. In the circumferential direction (cross sections), the amount of twist can be decomposed into two parts: the rotary angle of neutral axis of closed section (rectangular tube) and the warping angle of open section (fin). φ_c and φ represent twist of the closed section and the open section, respectively, as shown in Figure 5-32b. The dark line (deform) is the section shape of the extruded tube after removal from tooling and the dotted light line (undeform) is the design intent.

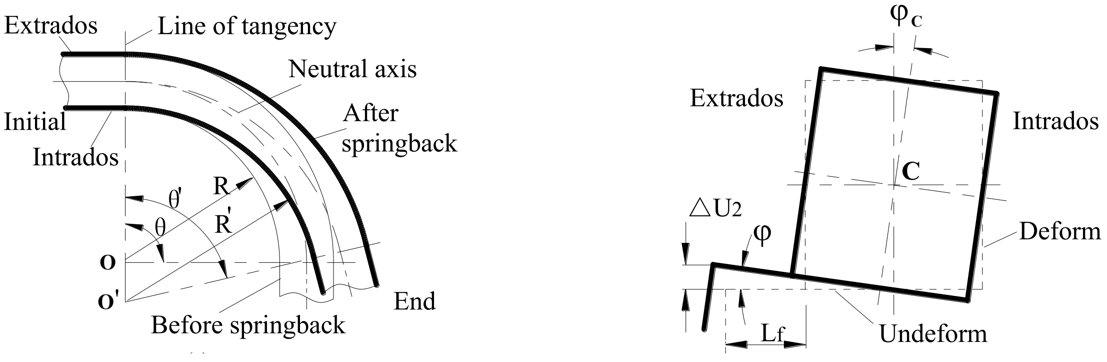

(a) (b)

Figure 5-32 Two deformation codes of twist springback: (a) longitudinal springback angle (b) twist springback angle of cross section.

In the next section, the torsion moment and twist angle relationship are analysed, in which figures out that the twist deformation of open section part should be much larger than that of closed rectangular part under the same process configurations. Therefore, twist angle of closed rectangular part can be ignored. In this work, the twist springback angle of open section part can be given by

$$\varphi = \arctan\frac{\Delta(U_2)}{L_f} \tag{5. 14}$$

where $\Delta(U_2)$ is the maximum displacement of open section part in the vertical direction (U_2), and L_f is the length of fin, as shown in Figure 5-32b. For the direction, the right-hand screw direction with respect to the longitudinal axis z was assumed as the positive direction for both twist and torsion moment.

5.3.3 Torsion moment-twist angle relationship for thin-walled tube

To analyse the twist deformation of thin-walled tubes, the concept of shear flow, q, needs to be understood. When a moment (or torque) load, *T*, is applied to a thin-walled tube, the load is distributed around the tube as shear stress, τ. But this is a difficult value to deal with since it is not constant. A better value is the shear flow, *q*, which is simply the stress multiplied by the changing thickness, *t*. For the thin-walled combined open and closed sections structure, the applied torque is given by

$$T=\sum_{j=1}^{n} 2q_i A_i+\sum_{i=1}^{m} GJ_i\theta \tag{5.15}$$

For this tube

$$T=2qA_E+GJ_F\theta \tag{5.16}$$

Here, A_E is the enclosed area defined by the wall midline, and J_F is the torsion constant of the open section part (the fin). Shear flow, *q*, represents the force per length acting around the tube caused by the moment as shown in Figure 5-33. Since *q* is constant along the contour, plainly the maximum shear stress occurs at the minimum thickness.

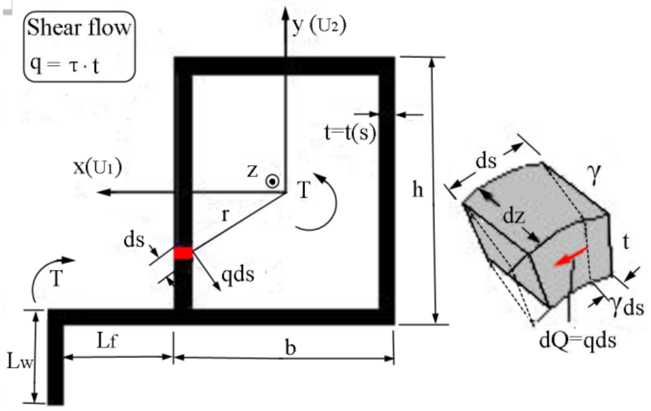

Figure 5-33 Thin-walled tube element deformation and the geometry of section.

The angle of twist can be developed using strain energy theory. For the small infinitesimal element, ds by dz, the force causing the deformation is dQ $(=qds)$. The deformation is zero and at the free end is (γds). Thus the average deformation is simply $(\gamma dz)/2$. According to Hooke's law $\gamma=\tau/G$, the strain energy equation can be given by:

$$dU=(qds)(\gamma ds)/2=q\gamma(ds)^2/2=q^2dsdz/2Gt \tag{5. 17}$$

This can now be integrated over the arc length of the bending tube, L, and around the circumference of the tube. This gives,

$$U = \frac{q^2}{2G}\int_0^L (\oint_S \frac{ds}{t})dz = \frac{q^2\rho\theta}{4G}\oint_S \frac{ds}{t} \tag{5. 18}$$

The energy caused by the applied moment is simply $U = T\varphi/2$, where φ is the angle of twist in radians. Using this condition and the shear flow relationship, $q = T/2A_E$, gives,

$$\frac{T\varphi}{2} = (\frac{T}{2A_E})^2 \frac{\rho\theta}{4G}\oint_S \frac{\mathrm{ds}}{t} \tag{5. 19}$$

Hence the angle of twist is given by

$$\varphi = \frac{T\rho\theta}{8GA_E^2}\oint_S \frac{\mathrm{ds}}{t} = \frac{T\rho\theta}{2GJ} \tag{5. 20}$$

Here the torsion constant of our particular cross section can be decomposed into two parts: J_C and J_A taken by the rectangular closed section tube and the open angle section fin, respectively. For the closed rectangular section, the torsion constant is given by

$$J_C = \frac{4A_E^2}{\oint \frac{\mathrm{ds}}{\mathrm{t}}} = \frac{2t(b-t)^2(h-t)^2}{b+h-2t} \tag{5. 21}$$

where *b, h* represent rectangular section width and height, respectively, as shown in Fig. 3. For the open angle section, the torsion constant is given by

$$J_A = \frac{1}{3}(L_f + L_w)t^3 \tag{5. 22}$$

where L_f, L_w denotes the length of flange and web of open angle section, respectively. With the assumption of the equivalent torsions occurred in rectangular tube and fin parts.

The ratio of the angle of twist for the closed section to the open section is given by

$$\frac{\varphi_C}{\varphi_A} = \frac{J_A}{J_C} = \frac{(L_f + L_w)t^2(b+h-2t)}{6(b-t)^2(h-t)^2} \approx \frac{(L_f + L_w)(b+h)}{6(bh)^2}t^2 \ll 1 \quad (\mathrm{t} \ll L_f, L_w, b, h) \tag{5. 23}$$

It is clear from this ratio that the twist angle of closed section is much smaller than open section having the same forming configuration. In other words, the twist deformation occurs predominantly in the open angle section fin for thin-walled tubes bending.

5.3.4 Finite element modelling and its key techniques

5.3.4.1 Experimental and numerical conditions

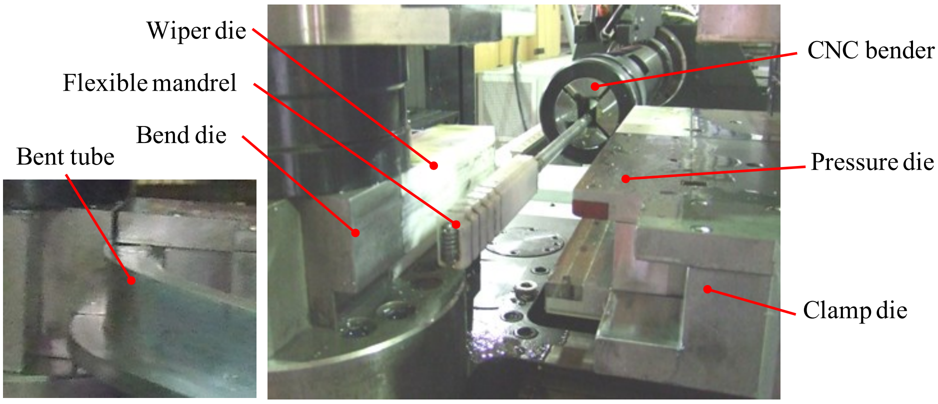

Figure 5-34 Experimental equipment and tools for MRDB.

The experiment equipment for the rotary draw bending process is a CNC microcomputer controlled bender, as shown in Figure 5-34. The main process parameters are listed in Table 5-2. The simulation process parameters are the same as the experimental one. With these parameters, a 3D Finite Element (FE) model was developed to simulate the bending of the aluminium tube using ABAQUS platform.

Table 5-2 Main forming parameters of MRDB.

No.	Parameters	Values
1	Bending velocity, ω/(rad·s)	0.523
2	Bend angle, θ/(°)	45
3	Bend time, (s)	3
4	Minimum bend radius, R/(mm)	116
5	Speed of pressure die, V_p(mm/s)	60
6	Clearances between tube and tools (mm)	0.1
7	Speed of mandrel retracted, V_m (mm/s)	100
8	Wiper die rake angle, δ_{w}/(°)	1
9	Mandrel extension, (mm)	2
10	Mandrel flexible cores	5

In this model, the bending, clamp, pressure dies and mandrel are defined as 3D bilinear rigid quadrilateral discrete rigid elements with four nodes (R3D4). The tube is meshed with linear, 4-node shell elements with reduced integration (S4R) elements. The mesh size of deformable part is 2mm×5mm. As two main section properties of element, the rule and the point of thickness integration are Simpson and 15, respectively. Boundary loading conditions of the moveable dies are carried out through the linear velocity (V_p and V_m, mm/s) and angular velocity (ω, rad/s), respectively, as shown in Figure 5-35.

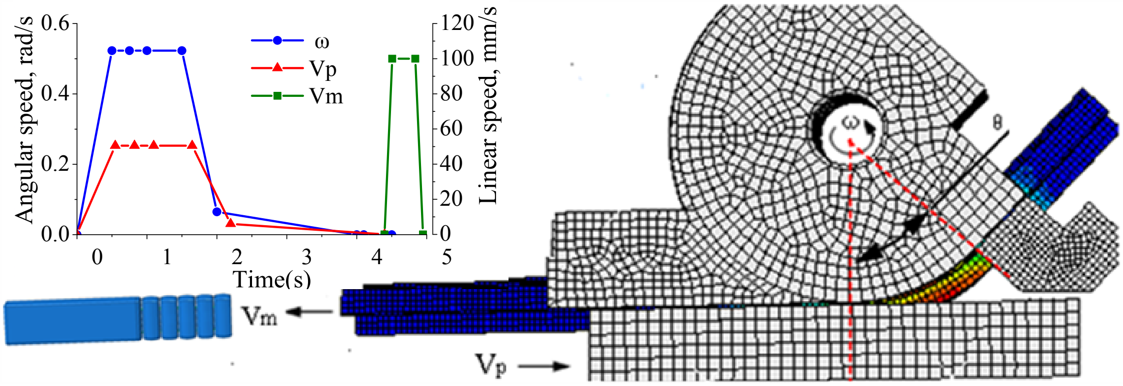

Figure 5-35 Boundary loading conditions of dies in the FE model.

Due to complex multi-body system of the mandrel and cores in the rotary draw bending, efficient kinematic constraint and accurate contact model of flexible mandrel and cores are critical for establishing a reliable and efficient numerical model.

5.3.4.2 Surface-based coupling constraint for flexible mandrel using HINGE connector element

Due to the complex multi-body system of mandrel-rotary draw bending process, the efficient boundary conditions and accurate contact model of flexible mandrel are necessary for establishing a considerable whole numerical model. Zhu et al. (2012) try to use simplified surface-to-surface friction contact instead of “JOIN+REVOLUTE’’ link (Zhao, 2009), which can avoid the turning around phenomenon and have the movement freedom of the cores be consistent with the experimental situation. However, the simplified surface contact model occupies too much computation time because there are many contact pairs involved in it. The geometry of flexible mandrel should be simplified to reduce the computational cost. This leads to be a lower accuracy of springback prediction because of the different geometry of mandrel with the real one in the experiment. This work introduces a surface-based coupling constraint for flexible mandrel using “hinge” connector element, which joins the position of two nodes and provides a revolute connection between their rotational degrees of freedom. By modelling the joint with an equivalent rotational HINGE connector element, the number of degrees of freedom can be reduced sufficiently to be more easily used in multi-body system analyses with minimal added degrees of freedom or computational cost (Desombre et al., 2011). The whole equivalent coupling hinge model of flexible mandrel is illustrated in Figure 5-36. The act of HINGE connector likes a non-linear rotational spring with non-linear damping to mimic the axial device properties based on the moment arm of its connection in the experimental setup.

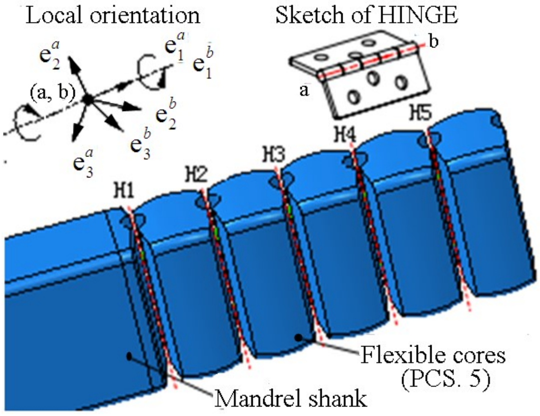

Figure 5-36 HINGE connector element and surface-based coupling constraint for flexible mandrel.

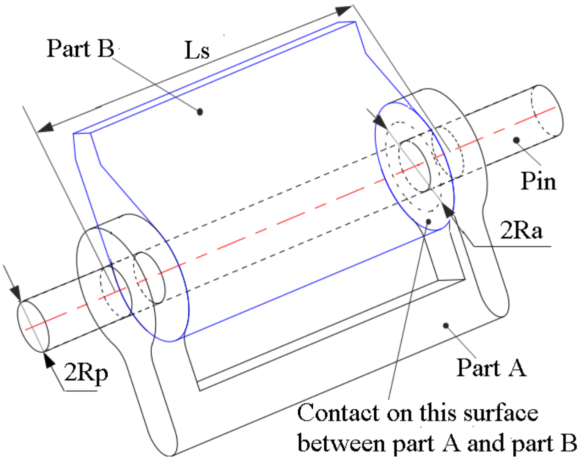

Figure 5-37 Illustration of the geometric scaling constants for a HINGE connection.

The connector constraint forces and moments reported as connector output depend strongly on the order and the location of the nodes in the connector element. Since the kinematic constraints are enforced at node *b* (the second node of the connector element), the reported forces and moments are the constraint forces and moments applied at node *b* to enforce the HINGE constraint. Thus, in most cases the connector output associated with a HINGE connection is best interpreted when node *b* is located at the centre of the device enforcing the constraint. This choice is essential when moment-based friction is modelled in the connector since the contact forces are derived from the connector forces and moments, as illustrated in Figure 5-37.

Table 5-3 The parameters that are used to specify predefined friction in HINGE connection.

No.	Parameters	Values
1	Kinematic constraints:	JOIN + REVOLUTE
2	Constraint force and moment output:	f_1, f_2, f_3, m_1, m_2
3	Available components:	μr_1
4	Kinetic force and moment output:	m_1
5	Orientation at *a*:	Required
6	Orientation at *b*:	Optional
7	Connector stops:	$\theta_1^{\min} \le \alpha \le \theta_1^{\max}$
8	Predefined friction parameters:	Required: R_p ,optional: $R_a, L_s, \mathrm{M}_\mathrm{C}^{\mathrm{int}}$
9	Contact moment for predefined friction:	M_C
10	Coupling constraint	Continuum distributing

Predefined Coulomb-like friction in the HINGE connection relates the kinematic constraint forces and moments in the connector to a friction moment in the rotation about the hinge axis. Table 5-3 summarizes the parameters that are used to specify predefined friction in this connection type as discussed in detail next. The geometric scaling constants for HINGE connection are illustrated in Figure 5-37.

Since the rotation about the 1-direction is the only possible relative motion in the connection, the frictional effect is formally written in terms of moments generated by tangential tractions and moments generated by contact forces, as follows:

$$\Phi=\mathrm{P(f)}-\mu\mathrm{M}_\mathrm{N} \le 0 \qquad (5.\ 24)$$

where the potential P(f) represents the moment magnitude of the frictional tangential tractions in the connector in a direction tangent to the cylindrical surface on which contact occurs, M_N is the friction-producing normal moment on the same cylindrical surface, and μ is the friction coefficient. Frictional stick occurs if $\Phi < 0$; and sliding occurs if $\Phi = 0$, in which case the friction moment is $\mu\mathrm{M}_\mathrm{N}$.

The normal moment M_N is the sum of a magnitude measure of friction-producing connector moments, $\mathrm{M}_C = g(f)$, and a self-equilibrated internal contact moment (such as from a press-fit assembly), $\mathrm{M}_{\mathrm{C}}^{\mathrm{int}}$:

$$\mathrm{M}_{\mathrm{N}} = \left|\mathrm{M}_C + \mathrm{M}_{\mathrm{C}}^{\mathrm{int}}\right| = \left|g(f) + \mathrm{M}_{\mathrm{C}}^{\mathrm{int}}\right| \tag{5. 25}$$

The magnitude measure of friction-producing connector contact moments, M_C, is defined by summing the following two contributions. One is a moment from an axial force, $F_a R_a$, where $F_a = |f_1|$ and R_a is an effective friction arm associated with the constraint force in the axial direction (the R_a radius could be interpreted as an average radius of the outer sleeve cylindrical sections as found in a typical door hinge or as an effective radius associated with the hinge end caps, if they exist; if R_a is 0.0, F_a is ignored); The other is a moment from normal forces to the cylindrical face, $F_n R_p$, where R_p is the radius of the pin cross-section in the local 2–3 plane and F_n is itself a sum of the following two contributions:

(1) A radial force contribution, F_r (the magnitude of the constraint forces enforcing the translation constraints in the local 2–3 plane):

$$F_r = \sqrt{f_2^2 + f_3^2} \tag{5. 26}$$

(2) A force contribution from “bending,” F_{bend}, obtained by scaling the bending moment, $\mathrm{M}_{\mathrm{bend}}$ (the magnitude of the constraint moments enforcing the Revolute constraint), by a length factor, as follows:

$$M_{\mathrm{bend}} = \sqrt{m_2^2 + m_3^2},\ F_{bend} = 2\frac{M_{\mathrm{bend}}}{L_s} \tag{5.27}$$

where L_s represents a characteristic overlapping length between the pin and the sleeve. If L_s is 0.0, M_{bend} is ignored.

Thus,

$$\mathrm{M}_C = g(f) = F_a R_a + F_n R_p = |f_1 R_a| + \sqrt{(R_p f_2)^2 + (R_p f_3)^2} + \sqrt{(\eta m_2)^2 + (\eta m_3)^2} \tag{5. 28}$$

where $\eta = {2R_p}/{L_s}$. The moment magnitude of the frictional tangential tractions, $\mathrm{P}(f) = |m_1|$.

Coupling constraints with HINGE connector element has three common types, i.e., kinematic, continuum distributing and structural distributing. In this work, the continuum distributing has been employed as coupling constraint. The continuum coupling method couples the translation and rotation of the reference node to the average translation of the coupling nodes. The constraint distributes the forces and moments at the reference node as a coupling nodes force distribution only. No moments are distributed at the coupling nodes. The force distribution is equivalent to the classic bolt pattern force distribution when the weight factors are interpreted as bolt cross-section areas. The constraint enforces a rigid beam connection between the attachment point and a point located at the weighted centre of position of the coupling nodes. Finite displacement and rotation terms take the form of a continuum constraint on the motion of the reference node as a function of the coupling-node finite incremental motions.

5.3.4.3 Numerical inverse method for interfacial friction coefficient identification

The interfacial frictional forces between dies and tube under mandrel-rotary draw bending (MRDB) cause non-homogeneous deformation, which affects both the material flow and the forming load. It is desirable to determine the flow stress considering the interfacial friction effect. The material flow and plastic deformation are sensitive to interfacial friction for MRDB with highly nonlinear dynamic conditions. Oliveira et al. (2005) assess the lubricant performance experimentally in tube bending of steel/aluminium tubes, and find that the mandrel load, surface quality and thinning degree of bending tube are manifestly affected by the lubricant type. While more quantitative study on friction role and underlying mechanism of bending behaviours cannot be conducted by the experiment because of the complexion of the MRDB (Yang et al., 2010). Either, the analytical results far deviate from the experimental ones since the friction conditions on various interfaces are difficult to be considered in the formulas. Nowadays, 3D FE simulation has been proved to be the primary approach to probe the deformation behaviours of tube bending with complicated contact conditions (Li, 2007). However, in most reported FE modelling, the coefficients of friction (COF) on different die–tube interfaces are designed as default value without robust physical foundation.

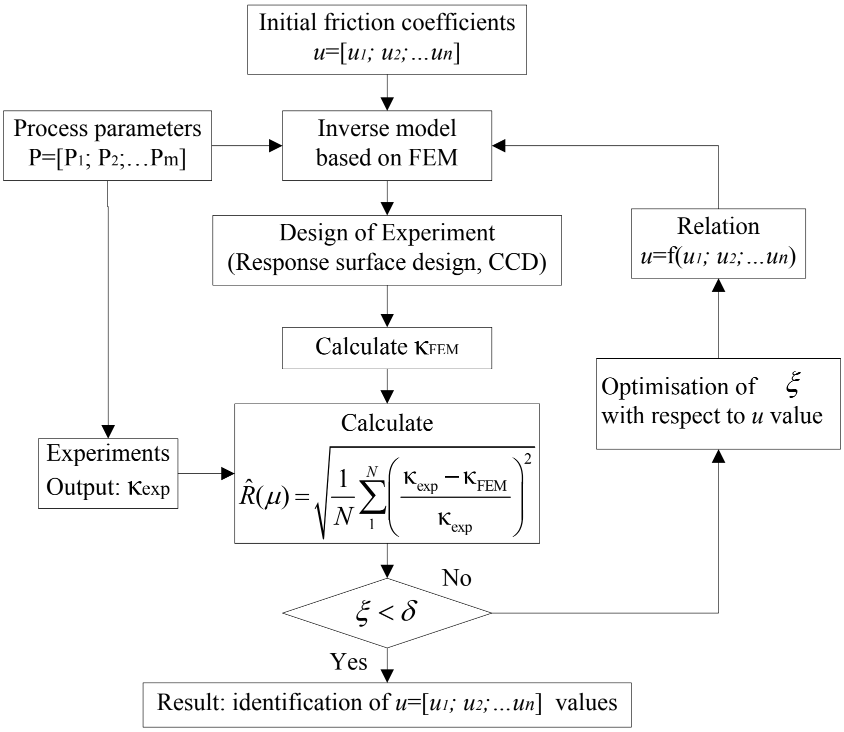

Figure 5-38 Flow chart for identification of interfacial friction coefficients by inverse analysis.

Numerical inverse method for friction coefficient identification in material forming has been proved to be an effective approach to probe the deformation behaviours with complicated contact conditions (Lin and Chen, 2005). Meanwhile, rotary draw tube bending is a complex non-linear physical process with coupling multi-factor interactive effects. This means several variables such as pressure force, rotate speed and boost force can be varied under dynamic contact conditions. Thus a comprehensive friction test for rotary draw tube bending is complicated and difficult. Yang et al. (2010) attempted to experimentally obtain the friction coefficients by using twist compression test (TCT). Through the friction coefficients obtained by experimental tests can be considered as initial approximate parameters, the friction coefficients still need to be optimized and introduced into the FE model for improving the prediction accuracy of plastic deformation. Therefore, numerical inverse method for interfacial friction coefficient identification in rotary draw tube bending is proposed in this work.

The procedure for inverse analysis is illustrated in Figure 5-38. The twist springback angles of the tested tube experimentally measured and numerical prediction are compared to identify the equivalent friction coefficients inversely. The inverse model can be represented by optimization problem

$$\begin{cases} \min\ y=f(x)=\hat{R}(\mu_1, \mu_2, \dots \mu_n)=\sqrt{\dfrac{1}{N}\sum_{1}^{N}\left(\dfrac{\kappa_{\exp}-\kappa_{\mathrm{FEM}}}{\kappa_{\exp}}\right)^2} \\ \text{s.t. } \mu \in [0.05,\ 0.7]. \end{cases} \tag{5.29}$$

where N is the total number of sampling points of the measurements, $\kappa_{\exp}$ and κ_{FEM} are the twist springback of experimental and simulative results, respectively.

In the experiment, the frictions on interfaces between the pressure die, the clamp die, the wiper die, the bend die and the tube are all the dry friction. Mineral oil is used between the mandrel-cores and the tube. In this work, one typical lubricant of tube bending, i.e., IRMCO GEL 980-000, was used in the experiments. The lubricant was applied manually on the flexible mandrel using a brush to provide a uniform distribution of lubricant on the contacting surface. In simulation of metal forming process, the Coulomb law is generally chosen to represent the friction behaviours. According to the friction test (Yang et al., 2010) and the conclusions of Ref. (Zhu et al., 2012), the range of friction coefficient can be from 0.05 to 0.7. Usually, friction coefficient of 0.7 can be identical to “Rough”. The friction on clamp die-tube interface can be equivalent to “Rough” because of large clamp force and tough tribological condition. The equivalent friction coefficients (u_i) are chosen for independent variables, and the twist springback κ_t is selected as response for inverse model. A central composite design (CCD) with three-level, four-factors based on Response Surface Methodology (RSM) is used to find out the relationship between response functions and design variables. The code values of friction coefficients in the FE model can be set as shown in Table 5-4.

Table 5-4 The friction on various die-tube interfaces and inverse coefficients.

No.	Contact interfaces	Lubricant conditions	Symbol	Code values (α=1.41)					Inverse values
				-α	-1	0	1	α	
1	Tube-bend die	Dry	μ_1 (μ_b)	0.07	0.1	0.15	0.2	0.23	0.1
2	Tube- pressure die	Dry	μ_2 (μ_p)	0.13	0.2	0.3	0.4	0.47	0.38
3	Tube- mandrel	Mineral oil	μ_3 (μ_m)	0.02	0.05	0.1	0.15	0.18	0.08
4	Tube- wiper die	Dry	μ_4 (μ_w)	0.02	0.05	0.1	0.15	0.18	0.15
5	Tube-clamp die	Tough dry	μ_5 (μ_c)	non					rough

Experimental plan for the coded values and FE Simulation results are shown in Appendix Table C.1. Since nonlinear responses of structures need to be considered, the following quadratic model approximates the FE simulation data:

$$\hat{R}(\mu) = \beta_0 + \sum_{i=1}^{n} \beta_i \mu_i + \sum_{i=1}^{n} \beta_{ii} \mu_i^2 + \sum_{i} \sum_{j>1} \beta_{ij} \mu_i \mu_j + \eta \tag{5.30}$$

where β is polynomial coefficient, n is number of design variables, and η is minor error. The coefficients of two empirical models are shown in Appendix Table C.2.

Statistical testing of the empirical models has been done by the Fisher's statistical test for Analysis of Variance–ANOVA. Appendix Table C.3 and Table C.4 show that the ANOVA tests applied to the individual coefficients in the model are significant. The F-value is the ratio of the mean square due to regression to the mean square due to residual. The Model F-value of springback and twist response are 9.29 and 16.75 respectively, which implie the models are significant. There are only 0.59% chance refered to springback response model and 0.12% chance refered to twist response model that the "Model F-Value" could occur due to noise. Values of "Prob>F" less than 0.05 indicate model terms are significant. The Determination coefficients of regression analysis results are $R^2(\theta) = 0.956$ and $R^2(\varphi) = 0.975$ respectively, indicating a high degree of correlation between the FE simulation values and predicted inverse values obtained from the response models.

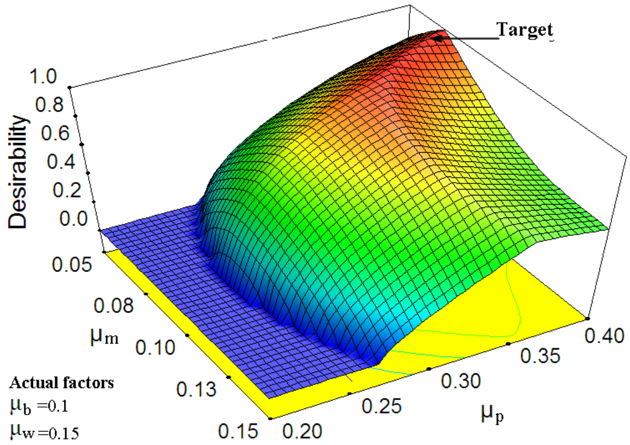

Figure 5-39 The desirability of response surfaces in terms of twist springback.

Based on the above analysis, an optimal strategy by means of inverse model is proposed against different contact interfaces to ensure the suitable stress/strain distributions and precise prediction of twist springback of bending tube. Using the proposal inverse model, this work intends to determine the optimum value of interfacial friction coefficients with the minimum error comparing with target value. In this work, the ideal value of target can be set as the experimental result. Taking the desirability of above regression models as response function, the optimal value of interfacial friction coefficients can be obtained, as shown in Figure 5-39. This plot has another special significance from technological point of view, because it will be determined for the interfacial friction parameters, which ensure the obtaining of bent tubes with an acceptable quality. For example, the proper tribological conditions should be adopted to achieve the desired friction levels for each friction interface. According to desirability of response surface, the related friction issues include whether to lubricate, to use suitable tooling materials for given tube material and to apply proper lubricant on correct interface.

5.3.5 Results and discussions

5.3.5.1 Comparison and experimental validation

For the particular asymmetric thin-walled tube, the twist springback within the open angle sections is considered in the analysis. This means that the other forming defects such as cross section distortion, over wall thinning and wrinkling are not considered here. This exclusion is based on real forming quality analysis, which clearly manifests that twist springback within the open angle sections is a serious defect at the assembly stages. In the industrial frame design, the angle section or other attached structure design typically are key parts for assembling. Improvement of the quality of asymmetric thin-walled bending tube means efficient control of twist springback, as well as numerical prediction.

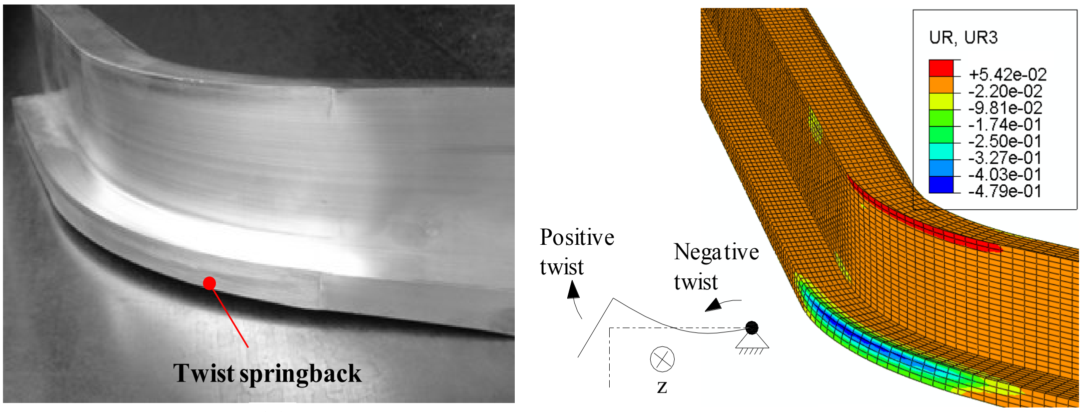

(a) (b)

Figure 5-40 Experimental and simulation results of twist springback of the asymmetric thin-walled tube: (a) experimental part; (b) simulation results by inverse values.

Based on the improved FE model, comparative analysis and experimental validation will be performed in this Section. Figure 5-40a shows the experimental part after forming, which has evidently twist springback occurred at the extrados of bending part. The rotation about 3-direction (UR3) is defined as the rotation about Z direction of numerical element. The whole distribution of UR3 after springback (see Figure 5-40b) shows the majority of tube has positive rotation but small value. The maximum value of positive rotation is only 0.05rad, but that of negative rotation is much larger 0.48rad. This simulation result also verifies analytical analysis in Section 5.3.3, which indicates that the twist angle of closed section is much smaller than open section under the same configuration.

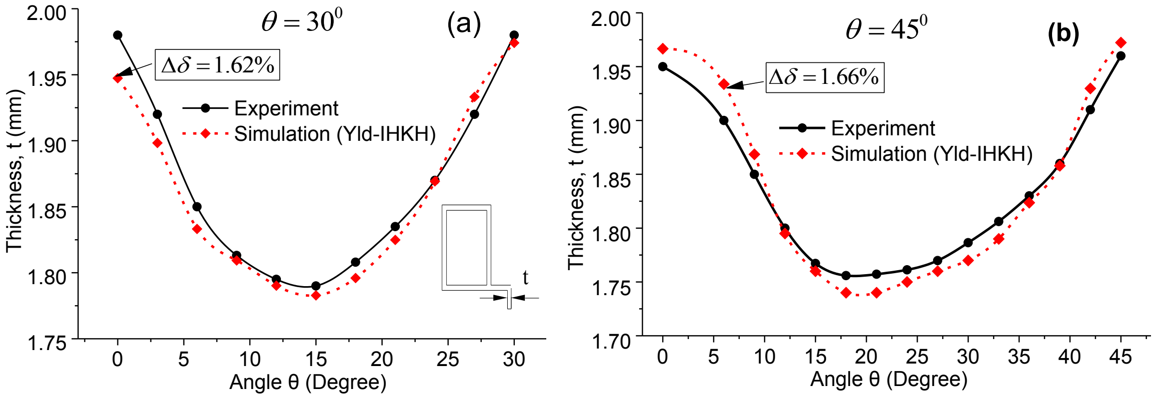

Figure 5-41 Side wall thickness distribution at the extrados of this tube after 30 degree (a) and 45 degree (b) rotary draw bending.

The side wall thinning at the extrados of this tube were used for comparison of experiment and the simulation results. Figure 5-41 shows the experimental side wall thickness and the predicted one by using the Yld2000-2d and the IHKH model. Note that the definition of angle θ is illustrated in Figure 5-32a, representing the measured position in the tube. It can be seen that all the simulation results are very close to the experimental values. The maximum error of wall thinning degree is 1.62% for 30 degree bending and 1.66% for 45 degree bending, which are in the allowable range. Therefore, the established FE model is valid and reliable.

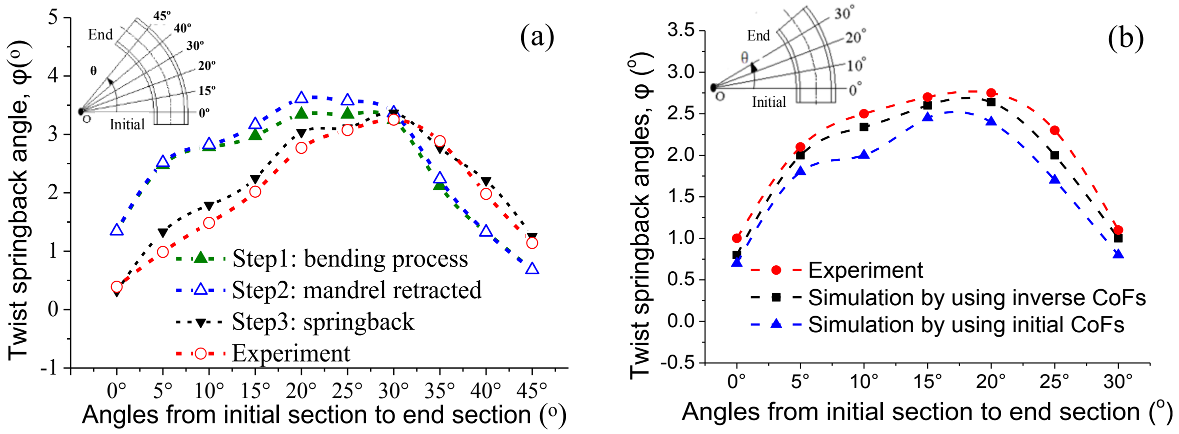

Figure 5-42 Comparison results of twisting deformation: (a) different steps and experimental results (b) another experimental validation of inverse method.

The validity of the FE model is also assessed by comparison of twist deformation history during different steps between the numerical prediction and the experimental results, as shown in Figure 5-42. It can be found that the twist angles slightly increase after mandrel retracted and decrease after springback. It can be also seen that with the progressing of the process, the twist moves backwards gradually along the bending tube. The validity of the numerical inverse method for interfacial friction coefficient identification is assessed by comparing with another experimental result, which has different bent angle under the same forming configuration. The Figure 5-42b shows that the prediction results of twist springback by using inverse values of friction coefficients still agree well with the experimental results, and are better than the simulation results using initial friction coefficients.

5.3.5.2 Deformation analysis

In order to explore the source of twist springback, the tangential stress distribution during different bending steps has been analysed, as shown in Figure 5-43. It can be seen that the tangential stress in the tension stress zone releases gradually with the progressing of the process. The maximum tangential stresses occur in the first bending process. During the mandrel retracting, the tangential stresses in the closed rectangular section part decrease but nearly keep unchanged in the open angle section part, as show in Figure 5-43b. This is because the interior flexible mandrel don’t directly contact with the open section part. In other words, mandrel condition makes little effect on the plastic deformation of open section part, e.g. twist deformation of angle section. But it affects the deformation of closed section part such as longitudinal springback and cross section distortion. Springback is the final unloading process, residual stress released after the dies moved away. Except the angle change of bent tube, it also affects the twist deformation in the open section part.

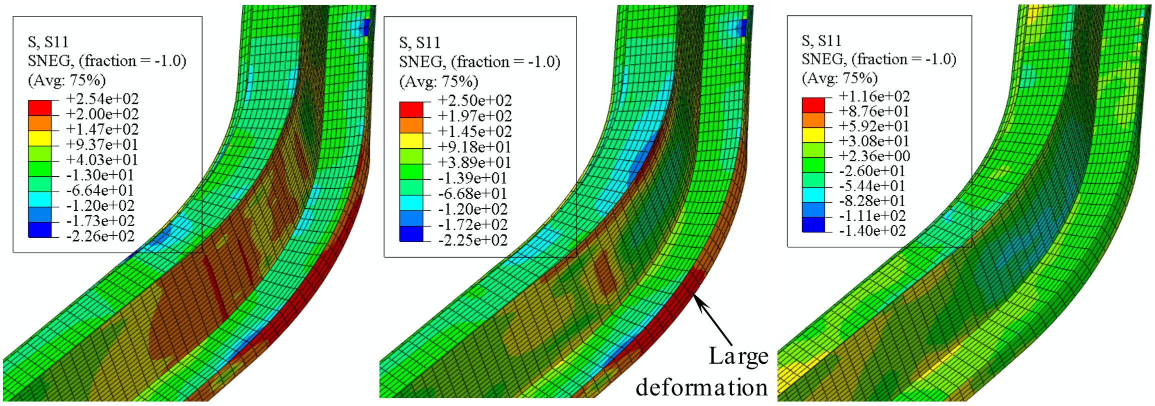

(a) (b) (c)

Figure 5-43 Global distribution of tangential stress at different steps: (a) bending process; (b) mandrel retracted; (c) springback.

Figure 5-44a shows the distribution of displacement (U2) at the end of whole process. The point A at the outside edge can be chosen as an object for tracking. From Figure 5-44b, it shows that the maximum twist angle of the trace point A increases lightly in the second step (mandrel retracted) but decreases in the final step. The fluctuation of displacement path in the steady plastic deformation stage is aroused by the unsteady contact deformation. The fluctuation evidently occurs in the springback step because the non-linear contact between dies and tube and dynamic die unloading paths

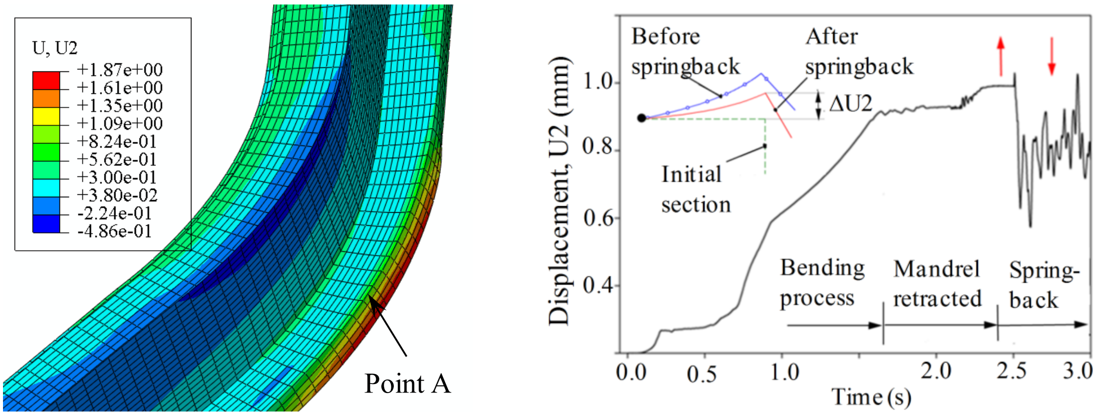

(a) (b)

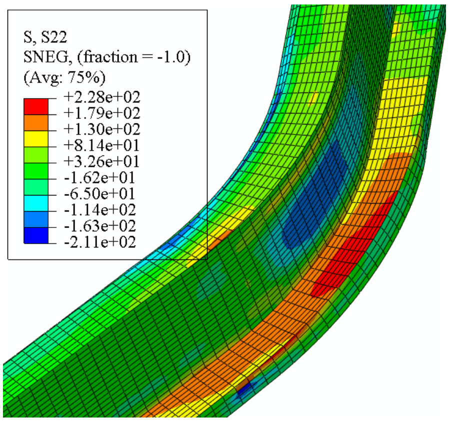

(c)

Figure 5-44 (a) The distribution of displacement (U2) (b) the displacement path of trace point A (c) the distribution of circumferential stress after mandrel retracted step.

In this section, the twist caused by springback could be analysed. During the springback step, the circumferential stress (S22) and the tangential stress (S11) respectively produce the negative and positive torsion moments. Figure 5-43b and Figure 5-44c indicate that the tangential stress on the open section part is larger than the circumferential stress after mandrel retracted process. This produces final positive torsion moment on bent sections during the springback step and makes the final twist angle decreased.

5.4 Partial conclusion

By using theoretical, experimental and numerical methods, two typical metal forming processes, deep drawing of DP steel sheets and rotary draw tube bending of asymmetric thin-walled aluminium alloy, are addressed due to their evident twist springback. A more reasonable definition of twist springback with respect to the principal inertia axes of the cross-sections is proposed. The relationship between torsion moment and twist angle is analysed to explain the occurrence of twist springback. Several key modelling techniques are performed for improving the robustness of the numerical models. The mechanism of twist springback is analysed from the evolution of in-plane stress and deformation history in the components after forming. The principal conclusions are:

For deep drawing of DP steel sheets:

- Several key modelling techniques, i.e., one-step formability analysis considering springback match and boundary constraint points for initial blank shape determination, digital image correlation technique and friction coefficient identification by correcting draw-in length of selected trace points were carried out to improve the prediction of numerical model.

- The adopted constitutive models, i.e., the anisotropic yield criterion Yld2000-2d and initial homogeneous anisotropic hardening (HAH) model are very efficient for the simulation due to their ability in predicting complex material behaviour. The validity of the FE model is assessed by comparing the predicted in-plane strain and twist springback with the experimental ones.
- The mechanism of twist springback is analysed from the in-plane stress and deformation in the channels after forming. It is found that the unbalanced bending / torsion moments, are responsible for twist springback in the proposed channel benchmarks.

For tube bending of asymmetric AA6060 thin-walled tube:

- A further improved 3D FE model with surface-based coupling HINGE constraint for flexible mandrel has been developed.
- Numerical inverse model for interfacial friction coefficient identification in MRDB is proposed by means of response surface methodology. A high degree of correlation between the FE simulation values and predicted inverse values has been obtained from the response models. The optimal values of friction coefficients have a high desirability of the twist and springback responses.
- The source of twist is analysed by the tangential stress distribution during different bending steps. The circumferential stress and the tangential stress produce the positive and negative torsion moments, respectively. The simulation results show that the tangential stress on the open section part is larger than the circumferential stress after mandrel retracted process. This produces positive torsion moment on bent sections during the springback step and makes the final twist angle decreased.

Chapter 6

Sensitivity analysis of twist springback

6.1 Introduction

In order to obtain the knowledge of the influence of forming factors on twist springback and improve the optimization, the sensitivities of some key parameters are performed. The influence of material constitutive models to the accuracy of twist springback prediction are analysed and discussed as well as some deep drawing process and numerical parameters of tube bending.

6.2 Influence of constitutive models on twist springback prediction

6.2.1 Elastic modulus

In Section 4.5, a significant effect of the loading strategy on the determination of nonlinear elastic behaviours was observed and discussed, as well as the sensitivity of different elastic modulus degradations of DP steels on the springback of the CFT case. Here, a special attention is paid to the sensitivity of elastic modulus variation on twist springback. DP780 steel with relatively higher springback amplitude was applied to test the sensitivity in the case of P-channel. It should be noted that the nonlinear elastic behaviour of the used aluminium alloy is not taken into account for this work since its week variation compared to that of dual-phase steels.

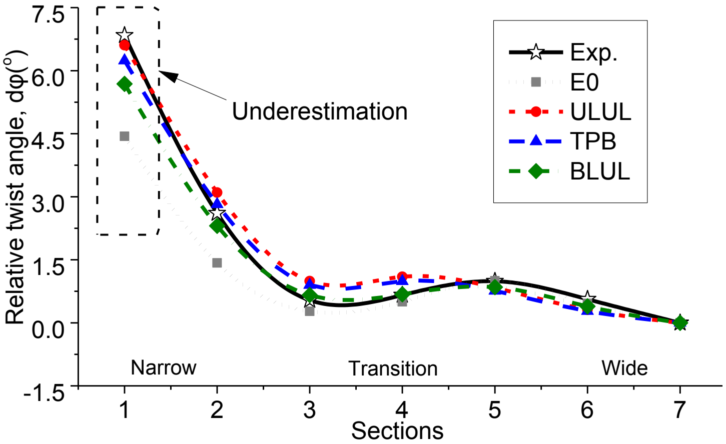

Figure 6-1 The influence of elastic modulus variation on the relative twist angle of the P-channel.

Two different types of elasticity models are considered in the present study. One follows the conventional Hooke's law, using a constant elastic modulus. The other assumes a strain-dependent elastic modulus in an exponential form, namely Yoshida chord model. In addition, the yield criterion Yld2000-2d integrated with the HAH model was adopted in the developed FE model to describe the material behaviours. In the case of P-channel, Figure 6-1 compares the measured twist angle with the predicted results based on initial average constant elastic modulus (E_0) and nonlinear elastic moduli, which were obtained from different loading strategies. It is observed that the twist evolution of the all simulation results agrees well with the experiment, although the twist springback is significantly underestimated by using the constant elastic modulus. The prediction of twist springback can be improved significantly by considering the degradation of the elastic modulus, which reveals the elastic modulus has a significant impact on the twist springback prediction.

The relationship between twist springback and elastic modulus degradation seems to be proportional. In the narrow section, all unloading strategies underestimate the twist. In the transition region, the uniaxial loading strategy (ULUL) and the three-point bending with pre-strained sheet (TPB) have a slight overestimation of the twist. This might be because the material flow at the transition region has experienced more complex strain path changes and the residual stress field was overestimated by using initial HAH model (Ha et al., 2013). It should be noted that the complex loading paths of the transition region should be further accounted for by using more advanced constitutive models. The work by Liao et al. (2016) implied that the selection of elasticity model should also consider loading path in the forming process. The common identification by ULUL test may not be appropriate for complex forming cases. For the C-channel, most of the elements were subjected to biaxial stress condition when the material flows into sidewall due to large deformation in both longitudinal and transverse directions. Thus, the elastic modulus identified by the BLUL test might be better suitable. But, for the P-channel, elements at the bottom web, the flange, sidewall of the straight side were under mostly uniaxial stress condition during the whole forming process. This might be the reason why the ULUL gave better results for this case.

6.2.2 Yield criterion

In order to study the influence of yield criterion on the prediction of twist springback in metal forming processes, three different yield criteria, i.e., von Mises, Hill'48 and Yld2000-2d were tested while constant elastic modulus and combined isotropic and kinematic hardening model were employed. Details of these models are described in the foregoing Section 3.3.

6.2.2.1 Deep drawing of DP steel sheet

For the DP500 C-channel, the comparison between experimental and numerical twist springback angle using different yield criteria combined with the IHKH model is shown in Figure 6-2. As observed in the experiment, the twist springback is the largest at the both ends, while the smallest is near the centre section but not the centre one. In other words, the twist springback evolution from centre to end section side is firstly slight decreased and then increased gradually. The simulated twist springback evolution of each cross-section is also in good agreement with experiments. Compared to isotropic yield criterion von Mises, the twist springback evolution is better predicted by the two anisotropic yield criteria, although globally the numerical twist springback deformation amount is lower than the experimental result. A quantitative comparison of the results from different yield functions is demonstrated by the standard deviation, as shown in Figure 6-2b.

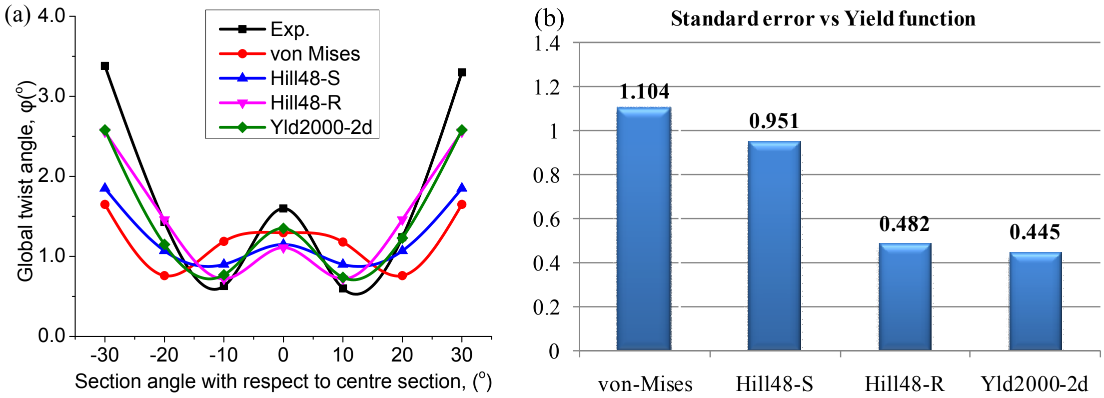

Figure 6-2 (a) Numerical prediction of the global twist angle using different yield criteria and experimental results (b) standard error.

The influence of the selected yield criteria on the predicted twist springback of the C-channel is evident. It can be clearly seen that the Hill48-R and Yld2000-2d yield functions lead to better results of twist springback than the other two models, while the Yld2000-2d model predicts the best. Note that the amplitude predicted with the Hill’48-R model is considerably better than that obtained using the Hill’48-S model. This might be due to that the stress anisotropy is not very pronounced for this material, and the error of stress from the Hill48-R is not so significant as the error of R-value for the Hill48-S, as observed in Section 4.2.1, Figure 4-5. It should be noted that although the r-value distribution dictated by Hill’48-R and Yld2000-2d is very close, the amplitude of the predicted twist angle is still slightly different. This likely correlate with the uniaxial yield stress directionality predicted by the Yld2000-2d model, which is more accurate. All the results indicate that the twist springback prediction is very sensitive to the yield function. A better twist springback prediction can be achieved by using anisotropic yield function which should be able to describe the anisotropy of both stress and R value of the materials. The prediction results also show that twist springback were underestimated by the aforementioned models. One possible reason for the lack of accuracy in springback prediction may be that the degradation of elastic modulus of DP steel was ignored in this comparison analysis.

6.2.2.2 Rotary draw bending of AA thin-walled tube

From the Table 6-1, it can be seen that for both 30° and 45° bending angle, the simulations using Yld2000-2d yield criterion show relatively good results for springback angle. The predicted results by the three yield criteria with IHKH model are all close to the experiment results. For 30° bending angle, the errors of the von Mises, Hill’48 and Yld2000-2d yield criterions are 6.3%, 5.50% and 5.3%, respectively. For 45° bending angle, the errors of the three yield criteria are 11.5%, 15.4% and 9.1%, respectively. It should be worth noting that taking into account Yld2000-2d improves the prediction results obviously. However, all yield criteria with IHKH model somewhat under predict the springback angle of the tube.

Table 6-1 Springback angle values calculated with three yield criteria.

Bending angle, θ	Yield criterion	Springback angle, $\Delta\theta$	Error, $\Delta\delta$	Exp. value, $\Delta\theta$
30	von Mises	3.75	6.3%	4.0
	Hill’48	3.78	5.5%	
	Yld2000-2d	4.21	**5.3%**	
45	von Mises	5.04	11.5%	5.7
	Hill’48	4.82	15.4%	
	Yld2000-2d	5.18	**9.1%**	

For twist deformation prediction, only the maximum twist angles are compared in Table 6-2. It can be seen that for both 30° or 45° bending angle, the simulation with von Mises and Hill’48 yield criterion always over predict the twist deformation while that with Yld2000-2d yield criterion underestimated them slightly. For 30° bending angle, the errors of twist by three yield criteria, i.e. von Mises, Hill’48 and Yld2000-2d, with IHKH model are 12.5%, 18.5% and 6.7%, respectively. For 45° bending angle, the errors of twist by the three yield criteria are 17.5%, 27.4% and 3.7%, respectively. Compared to springback angle, the twist deformation seems more sensitive to yield criterion. For the twist prediction, the simulation with Yld2000-2d yield criterion shows evident advantage than the other two yield criteria.

Table 6-2 Twist angle values calculated with three yield criteria.

Bending angle, θ	Yield criterion	Twist angle, ϕ	Error, $\Delta\delta$	Exp. value, ϕ
30	von Mises	3.04	12.5%	2.7
	Hill'48	3.20	18.5%	
	Yld2000-2d	2.52	6.7%	
45	von Mises	3.81	17.5%	3.24
	Hill'48	4.13	27.4%	
	Yld2000-2d	3.12	3.7%	

6.2.3 Hardening model

In order to study the influence of hardening model on the prediction of twist springback in metal forming processes, three different hardening laws, i.e., the isotropic hardening (IH), combined isotropic and kinematic hardening (IHKH) and the homogeneous anisotropic hardening model were tested as well as the adoption of Yld2000-2d anisotropic criterion.

6.2.3.1 Deep drawing

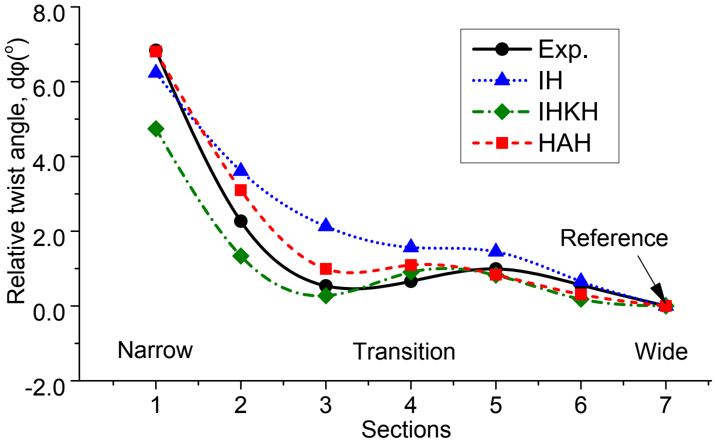

Figure 6-3 The influence of hardening model on relative twist angle of the DP780 P-channel.

Figure 6-3 compares the measured relative twist angle of DP780 P-channel with the predicted results by using the different hardening models, which were combined with the elastic parameter by ULUL. It is observed that the twist tendency seems to be better predicted by IHKH and HAH models than by IH model. In the narrow section, the HAH model leads to predicted twist angle in good agreement with the experimental measurement, although the values in the transition region are slightly overestimated. The twist springback are underestimated by the IHKH model but significantly overestimated by the IH model. One possible reason is that there are cross loading paths at the transition region during the deep drawing, and the used models (i.e., HAH-version 1 and IH) can't capture the transient behaviour of the DP steel for this loading conditions (Ha et al., 2013). This leads to overestimate the residual stress and the twist springback. Sun and Wagoner (2013) indicated that the IHKH model captured the response following a path change much better than isotropic hardening models, but there is a significant underestimation of the flow stress after a path change of principal strain axis.

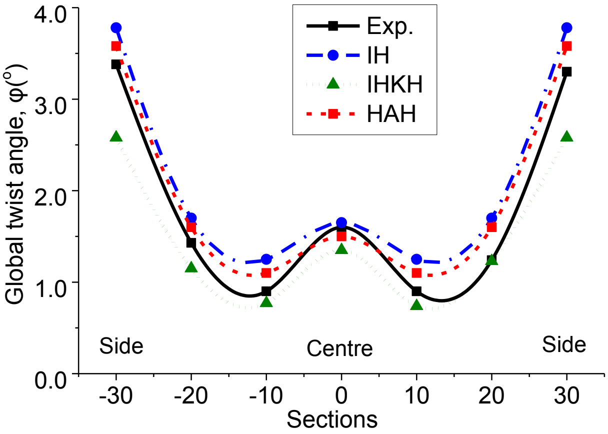

Figure 6-4 Influence of hardening model on relative twist angle of the DP500 C-channel.

Figure 6-4 shows the comparison of the experimental global twist angle of DP500 C-channel with the predicted resulted based on different hardening models and elastic modulus degradation obtained from the BLUL tests. It shows that, the IH model obviously overestimates the global twist springback, while the IHKH model underestimates the result. The HAH model overall seems to agree well with the experimental global twist evolution, although it has a slight overestimation except the centre section.

The above results indicate that the hardening model has a considerable effect on the twist springback prediction as well as the elastic modulus and yield criterion. The choice of hardening model should be based on the overall analysis of the other interaction factors such as unloading elastic property.

6.2.3.2 Tube bending

It is known that during rotary draw bending process, the tangent stress in the intrados of the tube is in the compression state and that in the extrados of the tube is in the tensile state. The difference between the residual tangential stresses yields a non-zero bending moment and thus the bending angle changes after springback. In an attempt to understand the effect of hardening models on springback angle and twist deformation for this tube, the tangent stress of two representative points A and B obtained by Yld2000-2d yield criterion with the IH and IHKH model are traced. The point A is in the intrados of the rectangular section, which is also the direct working area of the flexible cores and point B is in the flange. As shown in Figure 6-5, it is noticed that for point A, repeated loading and unloading processes and reversal loading occurred in the bending process.

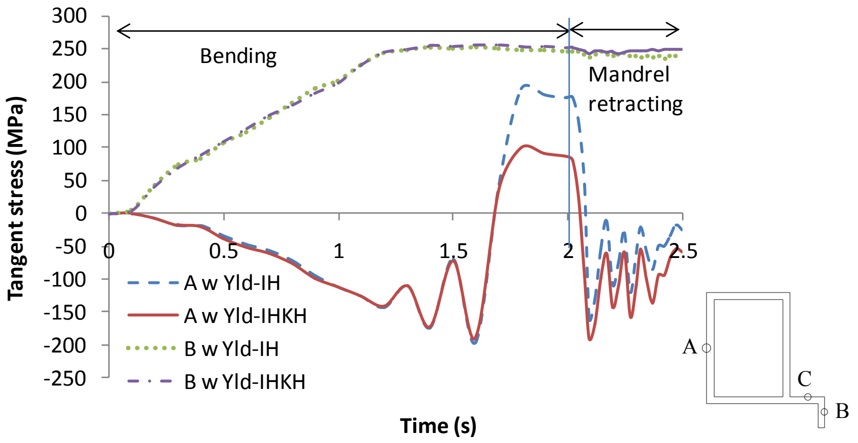

Figure 6-5 Tangent stress variations of point A and B during 45 degree bending process obtained by Yld-IH and Yld-IHKH models.

The two curves predicted by two hardening models don't show big difference during the forward loading process. However, when reversal loading occurs, some discrepancies between the two models are observed. The IH model predicts higher stress than that of IHKH model after load reverses. To explain this, the stress-strain curves of Figure 4-9, in which the mechanical behaviour of the material in forward-reverse shear tests reproduced by this two model, are compared. It is observed that just after load reverse, Bauschinger effect occurs and the IH model overestimate the stress during the transient stage, whilst the IHKH model reproduce the transient Bauschinger effect reasonably well as the experiment, i.e. the reverse stress is lower than that of the monotonic loading during the transient stage. Thereafter, it should be noted that curve crossing phenomenon occurs after the transient stage. Both the IH and IHKH model underestimated the flow stress, which correlates well with the results that the two models under predicts springback for this tube.

The comparison of the experimental springback and the predicted results based on IH and IHKH models respectively are shown in Figure 6-6a. On a whole, the IHKH model, although not perfectly, describes the mechanical response of this material better than the IH model, it achieves more accurate springback prediction results.

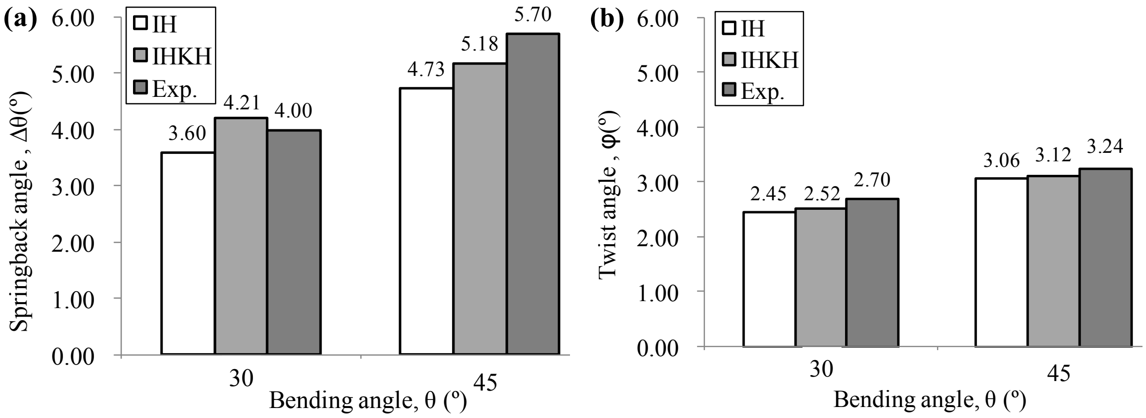

Figure 6-6 Comparison of the measured twist springback and the predicted results based on different hardening models: (a) Springback angle (b) twist angle.

From Figure 6-5, it is observed that for point B in the flange, reversal loading doesn't occur during bending and mandrel retracting processes. And not like point A, the tangent stress in the flange doesn't unload during mandrel retracting process. For curves obtained by the two different hardening models, it shows that the two are almost identical during the bending process. Comparing with the tangent stress variation of point A and B, it is obtained that the reversal loading and repeated loading unloading process are mainly caused by the flexible cores inside the rectangular section part. The flange, which didn't contact with the flexible cores directly, is not influenced by the reaction force caused by flexible cores during bending and mandrel retracting processes. This finding, which is similar to the conclusion presented in Zhu et al. (2013), show that the hardening model plays a very important role in the springback angle prediction for rotary draw bending process especially when the flexible cores are adopted as filler. However, as shown in Figure 6-6b, the twist deformation in the flange is less sensitive to the hardening model than the springback angle since the flexible cores has limited effect on the stress distribution in the flange.

6.3 Influence of some process and numerical parameters on twist springback

6.3.1 Deep drawing

In this Section, the sensitivities of the material direction, blank piercing and lubrication on twist springback were analysed and discussed. All experimental results were obtained from the deep drawing of DP500 C-channel.

6.3.1.1 Material direction

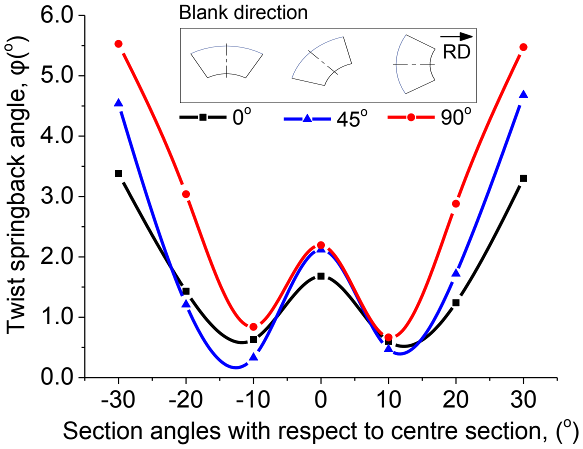

Figure 6-7 Experimental results of the twist springback (DP500) under different material direction configurations.

In order to further study the material plastic anisotropy on twist springback, three configurations of initial blank at 0°, 45°, 90° to the rolling direction and corresponding experiments of C-channel were performed. To avoid the effect of piercing, all the initial blanks did not have pilot holes, but were correctly positioned and aligned through the tool marks. As observed in Figure 6-7, the largest twist angles of the centre and side sections occur for the initial blank in the transverse direction (TD blank). The smallest twist angle occurs for the RD blank. The largest absolute values of twist angle are 5.53°and 3.38° for the TD and RD blank, respectively. This means that the material direction makes a significant effect on the twist springback.

For the 2D angular springback of the intrados and extrados flanges and sidewalls, as shown in Figure 4-20b, it can also be calculated as follows:

$$\begin{cases}\Delta\theta_e = \theta_e^f + \theta_e^s - 180^\circ \\ \Delta\theta_i = \theta_i^f + \theta_i^s - 180^\circ\end{cases} \tag{6.1}$$

In Figure 6-8a, it can be observed that the 2D angular springback of the intrados flange and sidewall ($\Delta\theta_i$) decreases from the centre to the side section along the longitudinal direction, while the value of the extrados flange and sidewall increases. The whole 2D angular springback is also listed in Appendix Table D1. Moreover, the angle of the extrados side is larger than that of the intrados side. This result also indicates that unbalanced elastic-plastic deformation occurs in the extrados and intrados and likely triggers twist springback. The ratio between extrados and intrados 2D springback angle is presented in Figure 6-8b, as a function of the section angle, indicating that the TD blank exhibits the highest level. This might also explain why the largest twist angle is observed for this material direction.

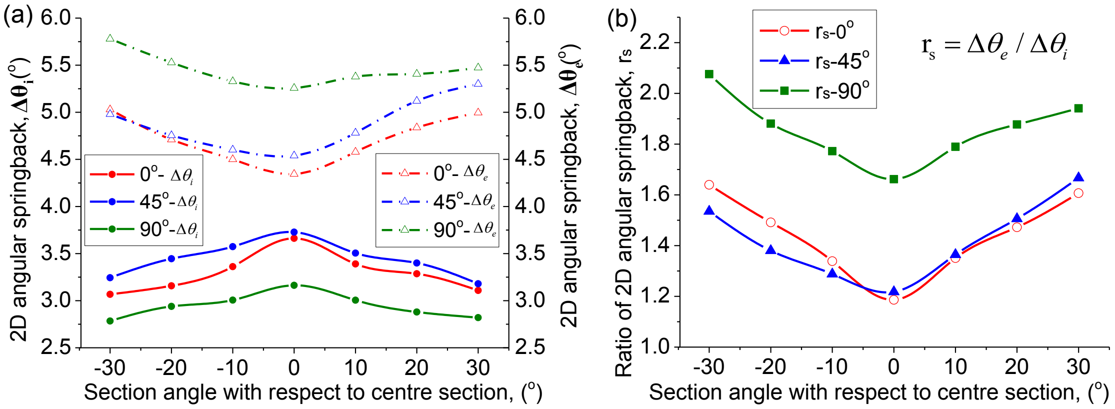

Figure 6-8 2D angular springback (DP500) of intrados and extrados flanges and sidewalls: (a) comparison of 2D springback under different material direction (b) the ratio of 2D springback.

From the stress distribution obtained by simulation (as shown in Figure 5-24), it is observed that the intrados and extrados flanges respectively produce stretching and shrinking deformations during the deep drawing process. This causes the thickness increase of the extrados flange, and consequently the contact area and frictional stress to be larger than the intrados flange. After forming, the opposite stress distribution in the intrados and extrados is one of the sources that lead to twist springback. Thus, any factor induced the stress difference between the intrados and extrados might affect the amplitude of twist springback. For instance, the r-value of cold rolled steel sheet acting for the deep drawability also affects the material flow during the deep drawing process, and influence the stress distribution. When the blank was changed along TD direction of the material, the stress difference between the intrados and extrados was higher than that along RD direction, leading to larger twist angle for this case.

6.3.1.2 Blank piercing

With respect to piercing, the complete set-up mainly includes detachable guide pillars in the punch and pilot holes in the initial blank. This design allows the initial blank to be in a consistent position under different forming configurations, especially for complex formed components. The centre of the holes can be used as boundary constraint points for the blank shape determination as well as a reference point for the measurements. However, as a major factor affecting the plastic flow during the forming process, the influence of blank piercing on the forming quality, in particular, twist angle, should be considered.

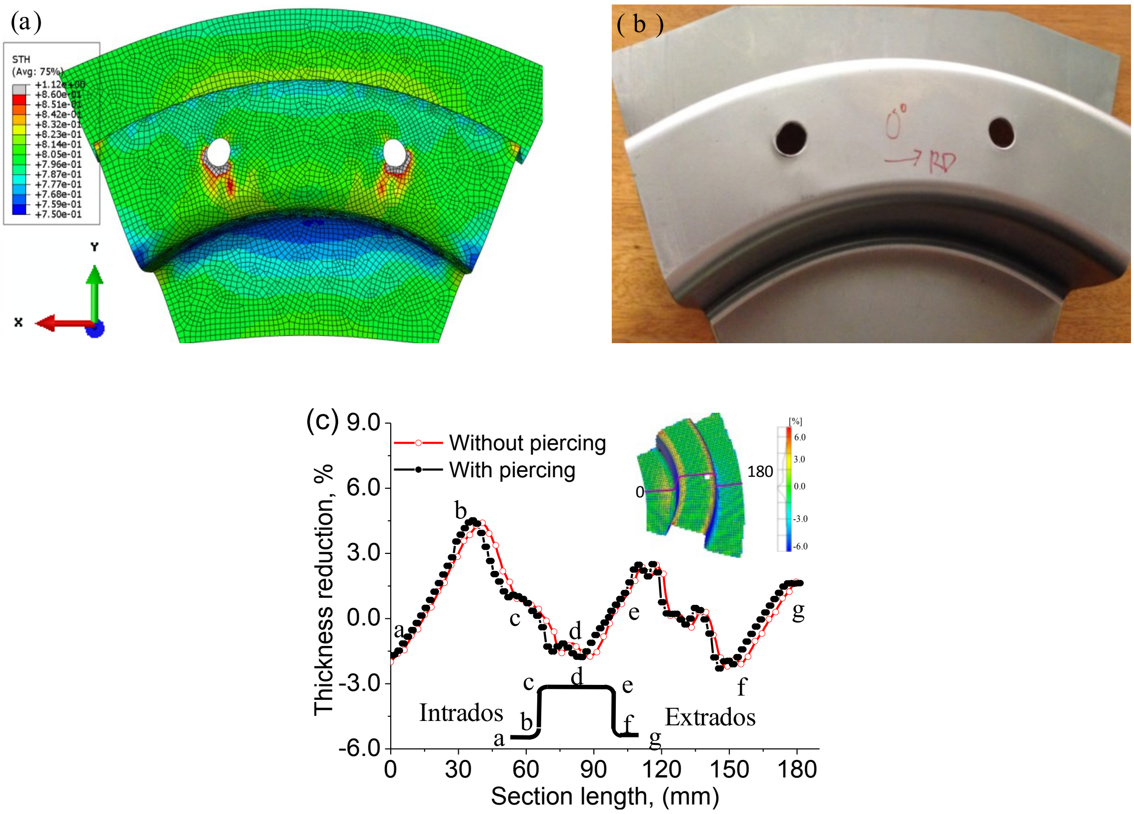

Figure 6-9 Influence of piercing on thickness reduction distribution: (a) Predicted result (b) drawn part with piercing (c) comparison of centre section thickness reduction.

The blank thickness distribution predicted with piercing is presented in Figure 6-9a. The thickness of the local area around the pilot holes is severely increased (reaching the maximum value of 1.12mm), which is in good qualitative agreement with the experimental observation shown in Figure 6-9b. However, the whole thickness distribution of the drawn part is not obviously changed. As observed in Figure 6-9c, the experimental thickness reduction of the centre section with piercing is slightly different from that without piercing. In other words, piercing has little effect on the formability of drawn part.

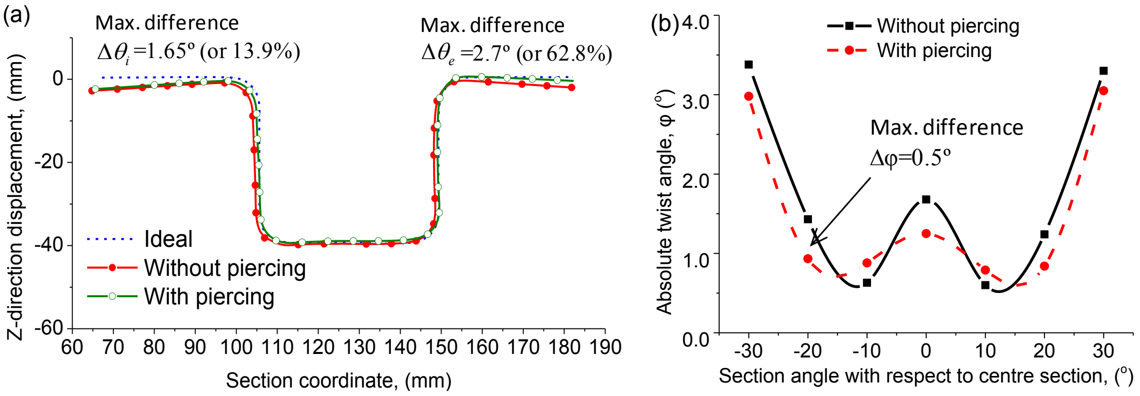

Figure 6-10 Influence of piercing on springback: (a) 2D angular springback of centre section (b) twist angle.

Due to piercing, the metal flow direction makes conspicuous changes around the pilot holes. Thus, the role and effect of piercing on forming quality should be taken into accounted on a case by case basis. Santos et al. (2002) noted that the existence of pilot holes did not seem to affect the final geometry of the final part in the case of 2D U-shape drawing. However, there are more complex plastic flow pattern and deformation field in the proposed 3D curved channel benchmark. The metal flow might be more sensitive to the geometric asymmetry of the part. Experimentally, the comparison of the centre section profiles indicates that the piercing has a considerable effect on the 2D angle springback of flanges, as shown in Figure 6-10a. The maximum differences of the 2D angular springback in intrados and extrados flanges are 1.65° (13.9%) and 2.7° (62.8%), respectively. For twist springback, Figure 6-10b indicates that the maximum angle difference occurs where the pilot holes are located. Therefore, piercing has a significant effect on the final geometry of the proposed curved channel.

6.3.1.3 Lubrication

In this work, the majority of the deep drawing experiments were performed by using mineral-base semisolid grease, namely GRASASH L-2. Because it can protect the surface grid marks and then provide well forming data using DIC technique. As shown in Figure 6-11, compared to the mineral oil, the semi-solid grease is a better option in terms of drawn surface quality and deformation analysis. The acceptable grids were about 95% of the whole geometry of C-channel. The average deviation for grid calculation by using semi-solid grease was 1.2% within an acceptable error range for the deformation analysis.

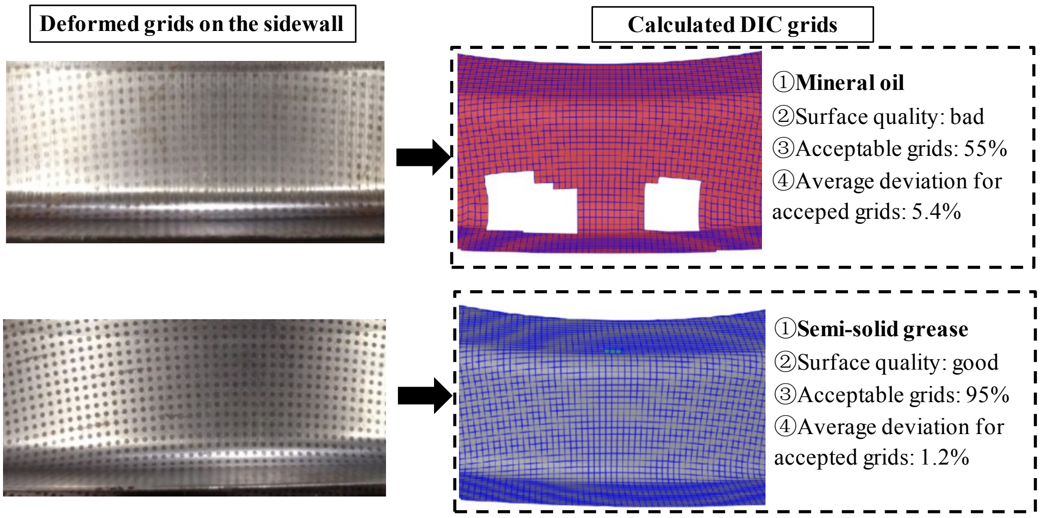

Figure 6-11 Influence of lubrication on drawing surface quality: (a) using viscosity oil lubrication (b) using semi-solid grease lubrication.

However, as a key process condition, lubrication should play an important role in deep drawing of AHSS sheet, particularly for springback. In this work, five types of lubricant conditions listed in Table 6-3 were employed to test the twist springback of DP500 sheets after the same forming configuration.

Table 6-3 Types of lubricants and some parameters

No.	Lubricant types	Parameter information
1	Dry lubricant	Tool surface roughness, R_a=0.48~1.0μm
2	Low viscosity mineral oil	Viscosity: 20W50
3	High viscosity mineral oil	Viscosity: 40W80
4	Mineral-base semisolid grease	Penetration at 25ºC (0.1mm): 265-295
5	PTFE film	25μm thick with one-side grease

Coordinate-measuring machine (CMM), namely Aberlink 3D CMM system, was considered to obtain the missing section coordinates of the drawn parts without lubricant and with mineral oil lubricants. Although this point contact measuring method is not time-efficient, as shown in Figure 6-12, it also provides a high accuracy with regard to surface geometry.

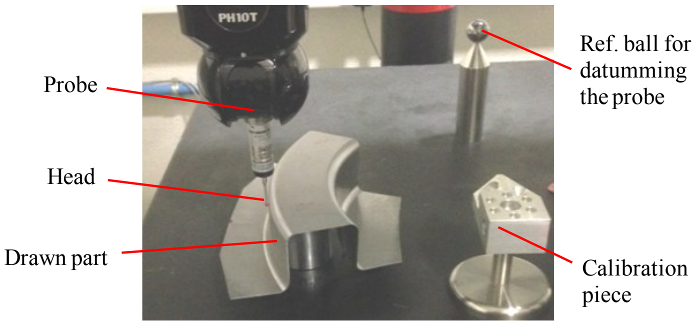

Figure 6-12 Measurement of section/surface coordinates using Aberlink 3D system.

Figure 6-13 compares the 2D angular springback of the intrados and extrados walls using different lubricants. It can be observed the usage of semi-solid grease or greased PTFE film have a little lower 2D angular springback than the other lubricants, whether intrados side or extrados side. In other words, the good lubrication not only provides good surface quality but also reduces the undesirable deformation, i.e., springback. This might be due to the decrease of restraining force with the better lubrication or lower friction. The frictional force caused by surface lubricant condition and pressure force plays an important role on deformation stress or strain field during the forming process.

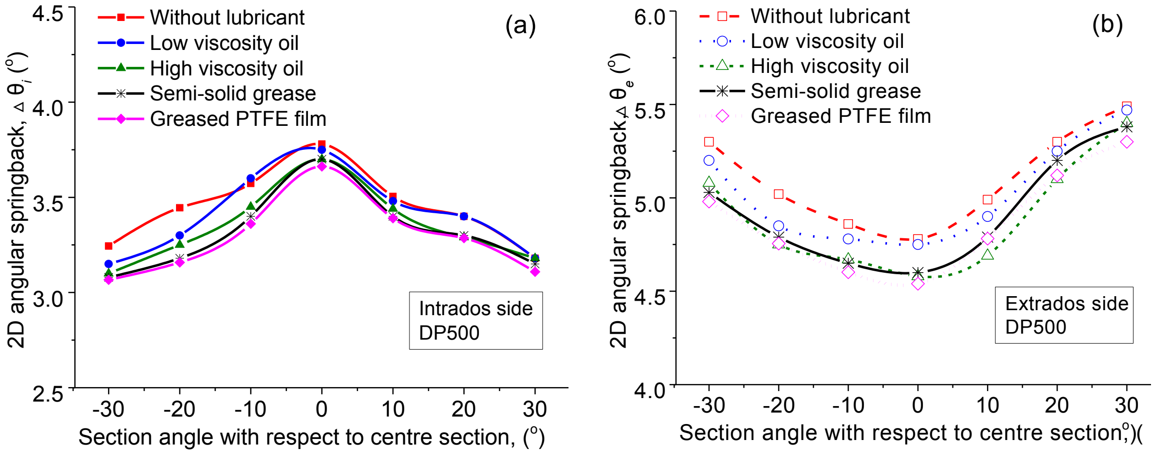

Figure 6-13 2D angular springback under different lubricates (a) intrados (b) extrados.

Figure 6-14 shows the comparison of the global twist angle of C-channel under different lubricants. It seems like that better lubricant less twist springback at the end sides. However, for the global twist analysis, it is difficult to find a further relationship between twist springback and lubrication condition.

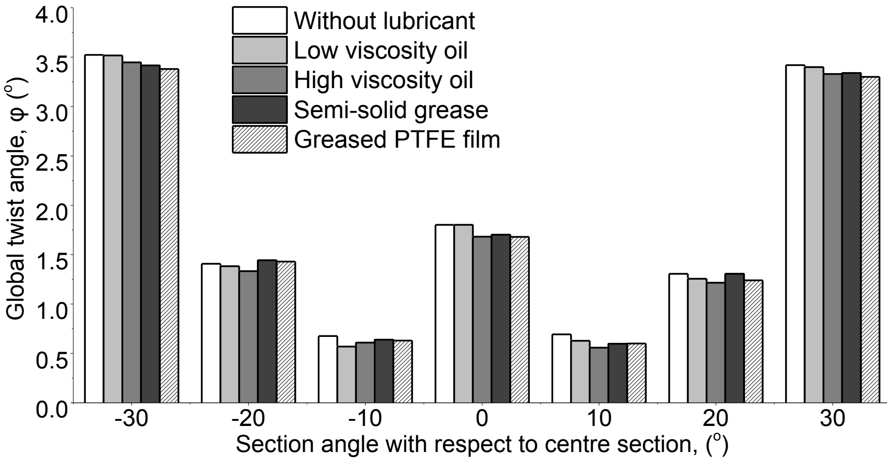

Figure 6-14 Global twist springback of C-channel under different lubricants.

6.3.2 Tube bending

In this Section, the sensitivities of two key numerical techniques for MRDB, boundary constraint for flexible mandrel and interfacial friction, on twist springback were analysed. The sensitivity of process conditions on twist springback is lacking because the experimental conditions are limited during the mass production of the studied industrial case.

6.3.2.1 Boundary constraint for flexible mandrel

During the mandrel-rotary draw bending process, the load and moment applied to the reference node of coupling constraint causes the complexity of the bending strain path. The coupling constraint of flexible mandrel should correctly reflect the frictional contact, deformation and force between the cores and the tube, and finally results in the high accuracy of the twist springback prediction.

Three models of mandrel flexible constraint, i.e., the single HINGE model, the simplified surface-to-surface contact proposed and the surface-based coupling HINGE model, are respectively applied to predict the twist springback and compared with experimental results, as shown in Figure 6-15. The present surface-based coupling HINGE model for mandrel flexible constraint has the highest precision than the others. Compared with simple HINGE model, the twist and springback prediction accuracy of the present model are improved by 9% and 9.5%, respectively. Compared with the surface-to-surface contact model, the twist and springback prediction accuracy of the present model are only improved by 5.3% and 5.7%, respectively. However, its computational cost has a large decrease, as well as simple HINGE model. In the others, the present surface-base coupling HINGE model for flexible mandrel can reach the balance between simulation accuracy and computational cost.

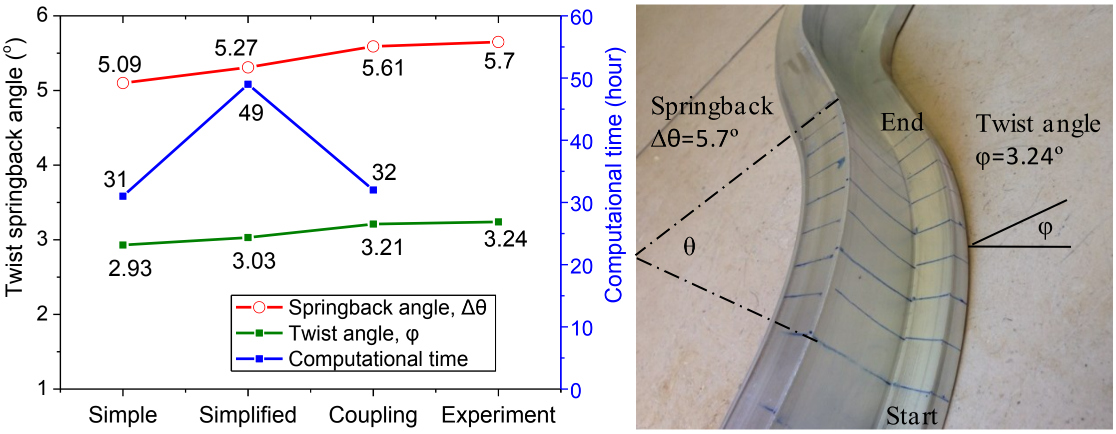

(a) (b)

Figure 6-15 (a) Comparison of twist springback prediction and computational cost using different constraint models of flexible mandrel (b) experimental results.

6.3.2.2 Interfacial friction

In this section, the role and effect of interfacial friction between dies and tube will be investigated. The friction on tube–clamp die interface should be sufficiently large to satisfy the necessary friction condition of MRDB. Generally, it can be increased by enhancing of the clamp force and surface treatment application. The methods of surface treatment such as knurling and coarse sand-blasting should be adopted on the groove of clamp die to increase the coefficients of friction (COFs) on this interface. The COFs on the other die-tube interfaces can be elaborated on by response surface methodology. Some of 3D response surfaces are given by empirical models, as shown in Figure 6-16. The plots depict the dependence between quality characteristics (i.e. twist and springback angle) and interfacial frictions. In the range of design variables, Figure 6-16a shows springback angle decreases with increasing of the friction on bend die-tube interface, while the friction on wiper die-tube interface has little effect on springback. Figure 6-16b shows that springback angle decreases with increasing of friction on flexible mandrel-tube interface, but the effect is not obvious. Meanwhile, the amplitude reduces with increasing of the friction on pressure die –tube interface. As it can be seen from Figure 6-16c and Figure 6-16d, all actual factors are involved in multiple interactions with respect to twist angle. Based on the above synthetic analysis, the effects of interfacial friction on twist springback can be epistemologically revealed by applying response surface methodology. The analysis of the influence of interfacial friction is also important for tool design and process optimization.

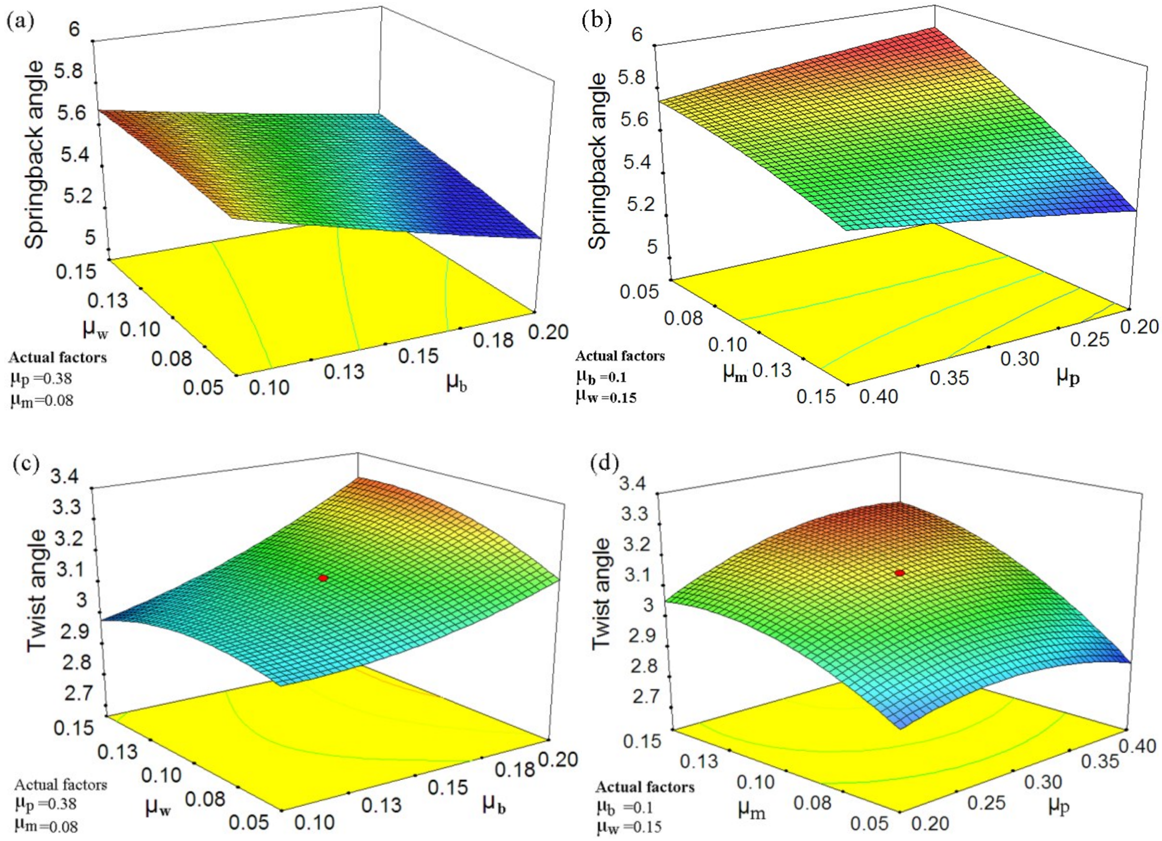

Figure 6-16 3D response surfaces and contour plots showing the effects of examined factors on responses.

The large friction should be applied to the interface between tube and pressure die in order to reduce the twist springback. However, the large friction of tube-pressure die may increase the wrinkling tendency to some extent. While the friction should not be large as that of tube-clamp die since large friction on this interface causes the tube surface scratched. The suitable COF on pressure die-tube interface should be 0.35–0.4. The friction of tube-wiper die interface makes little effect on springback and twist due to the wiper die rake angle, which lowers the contact deformation. Small friction need to be applied to the interface of tube-bend die, and the die surface should be polished enough. To reduce the friction on this interface, lubricant might be evenly pumped or hand-applied to the outside bend die surface. Though the friction of tube and mandrel interface has a little effect on the stress and strain states, it is generally regarded as small as possible. Because the mandrel is more or less undersized caused by the wear of tools during the mass production, the material of mandrel and the link between mandrel shank and flexible cores are more important than lubricate for MRDB.

6.4 Other potential factors

For the prediction of twist springback, some other potential numerical parameters affecting the accuracy will be the following:

- Mesh element type, e.g., brick element;
- Sheet/tube thickness section property, e.g., the number of the thickness integration point;
- Nonlinear contact model, e.g., friction formulation;
- Considered deformable tools in the numerical model;
- Virtual forming speed;

…

In sheet metal forming, some other potential process factors affecting the twist springback will be following:

- Stamping rate or forming speed;
- Blank holder force,
- Initial blank shape and its position;

…

In mandrel rotary draw bending of thin-walled tube, some other potential process factors affecting twist springback will be following:

- Mandrel material, e.g., PVC or steel
- Flexible core structure, e.g., chain connector;
- Bending speed, which also affects the efficiency of mass production;
- The residual stress of the extruded tube;
- The variable thickness design of complex thin-walled tube;

…

Twist springback phenomenon of lightweight automotive structures might be occurring in some other metal forming processes such as hot porthole extrusion, incremental sheet metal forming, welding or machining induced non-uniform residual stress and so on.

Sensitivity analysis of the underlying numerical and process parameters mentioned above should be helpful to gain a better understanding of the mechanism of twist springback and establish robust forming condition for stable and precise manufacturing of lightweight automotive components.

6.5 Partial conclusion

The sensitivities of the material constitutive models including elasticity model, yield criterion and hardening model on twist springback are shown to be significant. The main conclusions are as follows:

- First, the prediction of twist springback can be improved significantly by considering the degradation of the elastic modulus in case of deep drawing of P-channel. This reveals the elastic modulus has a considerable effect on the twist springback prediction.
- Second, all the simulations with Yld2000-2d yield criterion show evident advantage than the other yield criteria. In case of C-channel, globally the predicted twist springback angle is lower than the experimental measure. As for tube bending case, compared to springback angle, the twist deformation seems more sensitive to yield criterion.
- Third, the HAH model for the prediction of the twist springback of P-channel and C-channel overall seems to be better than the IH and IHKH models, although it still has a slight deviation compared to experimental result. For asymmetric thin-walled tube, the twist deformation in the flange is less sensitive to the hardening model than the springback angle. This is because the flexible mandrel, which plays an important role in the reversal loading and repeated loading unloading process, has limited effect on the stress distribution in the flange.

The influence of deep drawing process parameters (material direction, blank piercing and lubrication) and numerical parameters of tube bending (boundary constraint for flexible mandrel and interfacial friction) on twist springback are provided.

For deep drawing process parameters:

- Related to the material direction of DP500 C-channel, the experimental observation shows that it has a considerable effect on twist springback. Twist springback occurred for the initial blank in the transverse direction (TD blank) is obviously larger than that for the RD blank.
- Blank piercing is shown to significantly affect the final geometry of the curved C-rail drawn part, although it had little effect on the thickness reduction.
- The good lubrication not only provides good surface quality but also reduces the undesirable deformation, i.e., 2D springback. It seems like that better lubricant leads to less twist springback at the end sides. However, for the global twist analysis, it is difficult to find a further relationship between twist springback and lubrication condition.

For numerical parameters of tube bending:

- Compared with simple HINGE model, the twist and springback prediction accuracy of the present model are improved by 9% and 9.5%, respectively. Compared with the surface-to-surface contact model, the twist and springback prediction accuracy of the present model are improved by 5.3% and 5.7%, respectively. Furthermore, its computational cost has a large decrease, as well as simple HINGE model. The present improved FE model can reach the balance between simulation accuracy and computational cost.
- The sensitivity analysis of interfacial friction on twist springback shows that the large friction should be applied to the interface between tube and pressure die to reduce the twist springback, and the suitable COF on pressure die-tube interface should be 0.35–0.4. The exhaustive analysis provides guidelines for applying the tribological conditions to establish the robust bending condition for stable and precise manufacturing of tubes.

Chapter 7

Control strategy of twist springback

7.1 Introduction

In this Chapter, a special attention is paid to the control strategy of twist springback in terms of individual case, a topic that has not been emphasised often so far. For deep drawing of AHSS channels, two control strategies, variable die radius and partial draw bead design, were proposed to reduce the twist springback of the C-channel and the P-channel, respectively. For mandrel rotary draw tube bending, optimization of mandrel nose placement and push assistant loading are presented to assess the efficiency for the twist springback control. These FEA-based control strategies should be helpful to establish robust tool design and forming condition for stable and precise manufacturing of lightweight automotive structures.

7.2 AHSS channels

7.2.1 Variable die radius design for C-channel

From the previous stress/moment analyses, it can be deduced that decreasing the unbalance bending moment distribution in the longitudinal direction decreases twist springback. Generally, the approaches achieve springback control primary focus on process optimization and die compensation (Lingbeek et al., 2008). As for the control of twist springback, Geka et al. (2013) attempted to reduce springback by a stroke returning deep drawing method in the case of the hat channel with high-strength steel sheets. This approach can be an alternative to reduce twist springback mainly for the bottom web of U-shape channel products, but it is still difficult to reduce twist springback of the whole profile including side walls and flanges. Iyama et al. (2003) investigated the twist springback of a complex-shaped hat channel product, which combines a straight part with a curved part in the longitudinal direction. Their results pointed out that the twist deformation might be decreased by reducing the bending moment, which can be achieved by adjusting the die radius. These efforts suggested controlling twist springback by performing a suitable relative balance of stresses or moments in deep drawing. However, they did not obtain the accurate metal flow evolution and further study the relationship between the variable die radii and twist springback. As a major factor affecting material flow and bending moment, the die radius appears to play a considerable role on the control of twist springback in the present benchmark.

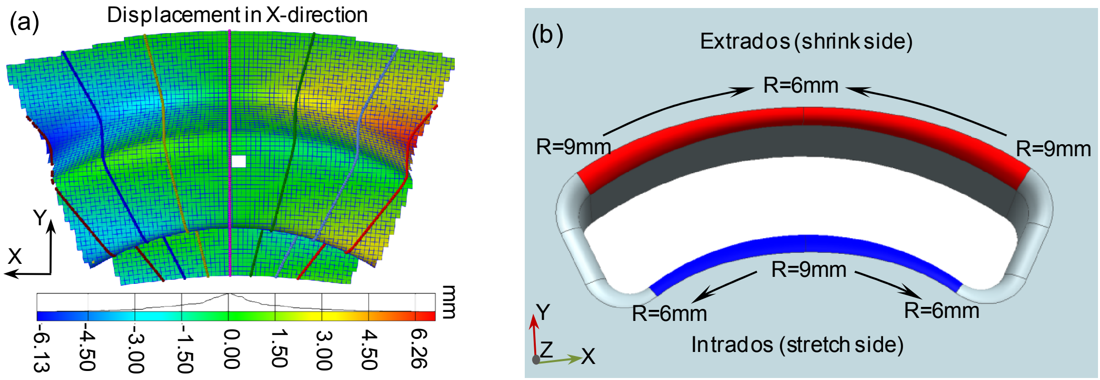

Figure 7-1 The modified tool design: (a) displacement distribution in the X direction of uniform die radius by DIC technique (b) variable die radius.

Figure 7-1a indicates that displacement due to metal flow is greater at the end sides than in centre section on the extrados. In contrast, the displacement in the centre section is larger than that at the end side on the intrados. Therefore, in this work, a modified tool design with variable die radius is proposed. As shown in Figure 7-1b, R represents the variable die radii at the corresponding positions, and the direction of allow illustrates the evolution of variable die radius from large to small values. From the centre to side sections, the extrados die radius is increased smoothly from 6.0 to 9.0mm while the intrados die radius is decreased smoothly from 9.0 to 6.0mm. This is because the relatively larger die radius should favour metal flow in the circumferential direction during deep drawing. Moreover, the metal flow induced by the modified variable die radius in the longitudinal direction becomes more difficult on the extrados but easier on the intrados. This means that the modified design is helpful for decreasing a positive bending moment on the extrados and increasing the negative bending moment on the intrados.

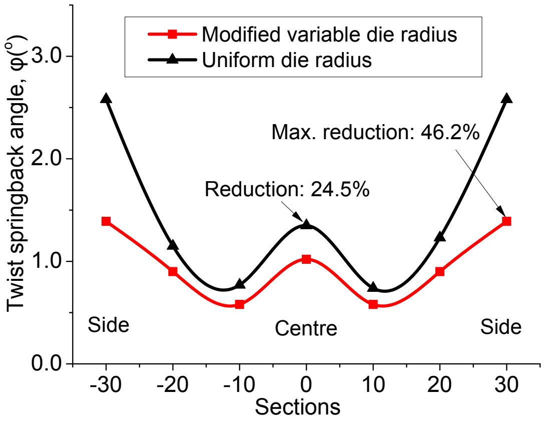

Figure 7-2 Comparison results of twist springback angle between modified variable die radius and uniform one based on simulation results.

Figure 7-2 compares twist angles obtained using the constant and variable die radii, indicating that twist springback can be obviously decreased with variable die radius. The maximum twist springback angle at the side section is reduced by 46.2%, while the twist springback angle at the centre section is reduced by 24.5%. Therefore, the design based on variable die radii to balance the extrados and intrados bending moment should be an alternative for the minimization of twist springback.

Table 7-1 Several sets of variable die radius ratio

No.	Intrados die radius (mm)		Extrados die radius (mm)		Ratio
	Centre	Side	Centre	Side	
1	6.0	6.0	6.0	6.0	1.0
2	7.5	6.0	6.0	7.5	1.25
3	9.0	6.0	6.0	9.0	1.5
4	10.5	6.0	6.0	10.5	1.75
5	12	6.0	6.0	12	2.0

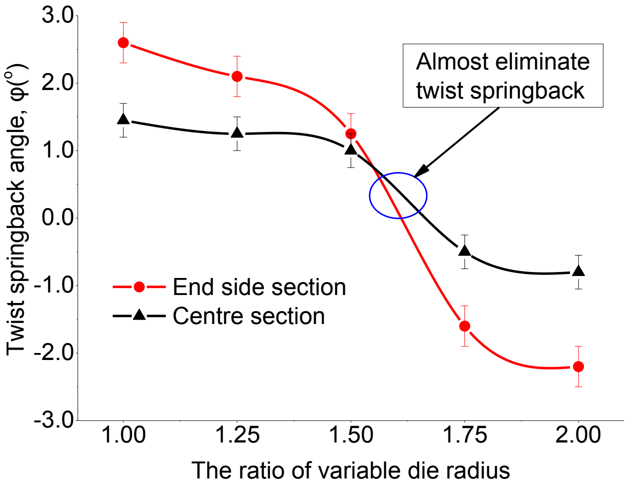

Figure 7-3 The relationship between the ratio of variable die radius and twist springback.

In order to explore the relationship between the variation of die radius and twist springback, several sets of variable die radius ratio were performed based on the numerical model, as listed in Table 7-1. The minimum die radius was fixed to 6.0mm, and the variable die radius ratio changes from 1.25 to 2.0. Figure 7-3 indicates that the twist springback angle decreases with the increase of the ratio of variable die radius. The evolution from positive to negative occurs at the ratio close to 1.6, which is the optimum value to almost eliminate twist springback in the proposed C-rail benchmark. More different geometry but similar cases should be further studied and helpful for die design. This work is particularly important for AHSS channel components where the shape of the section varies along a curvature path. In addition, further investigations are needed for the design optimization of the die radius as well as the coupling effects between 2D springback and twisting.

7.2.2 Partial draw bead design for P-channel

From the analyses of torsion moment in Section 5.2.8, it is clear that the torsion moment is mainly caused by the asymmetric longitudinal in-plane stress on the curved transition flange and sidewall, and the narrow section is prone to cause twist than wide section under the same torsion moment. Beside one reason that the torsion stiffness of narrow section is less than that of wide section, the other main reason is the large residual compression longitudinal stress on the sidewall of transition region close to the narrow side. Based on this finding, one countermeasure against the twist problem of P-channel that disperses or reduces the stress in the affected portions was studied: partial draw bead design. The developed P-channel deep drawing of DP 780 sheets was applied to verify the efficiency of this control strategy.

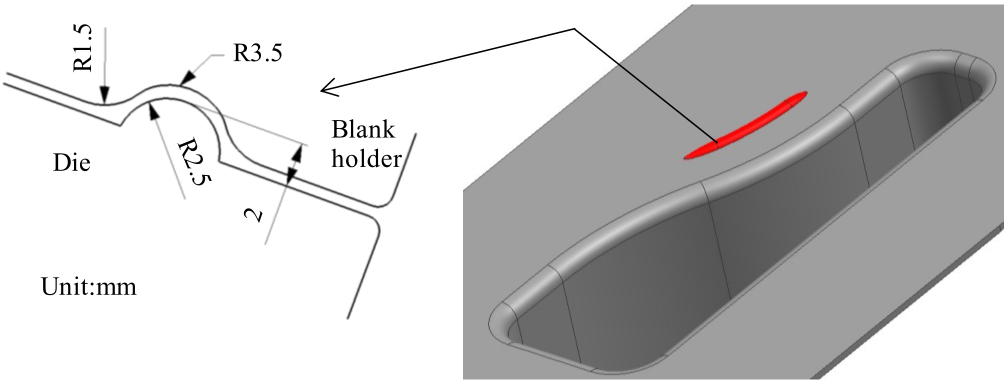

Figure 7-4 Schematic of section shapes of partial bead.

In order to disperse and reduce the longitudinal stress imposed on the narrow transition flange and sidewall that caused the torsion moment change, bead was formed along the narrow transition corner, and the effect of its presence was examined. As can be seen in Figure 7-4, the bead was mainly designed to have a round section 2.5 mm in radius (on the die side) and 2.0 mm in height.

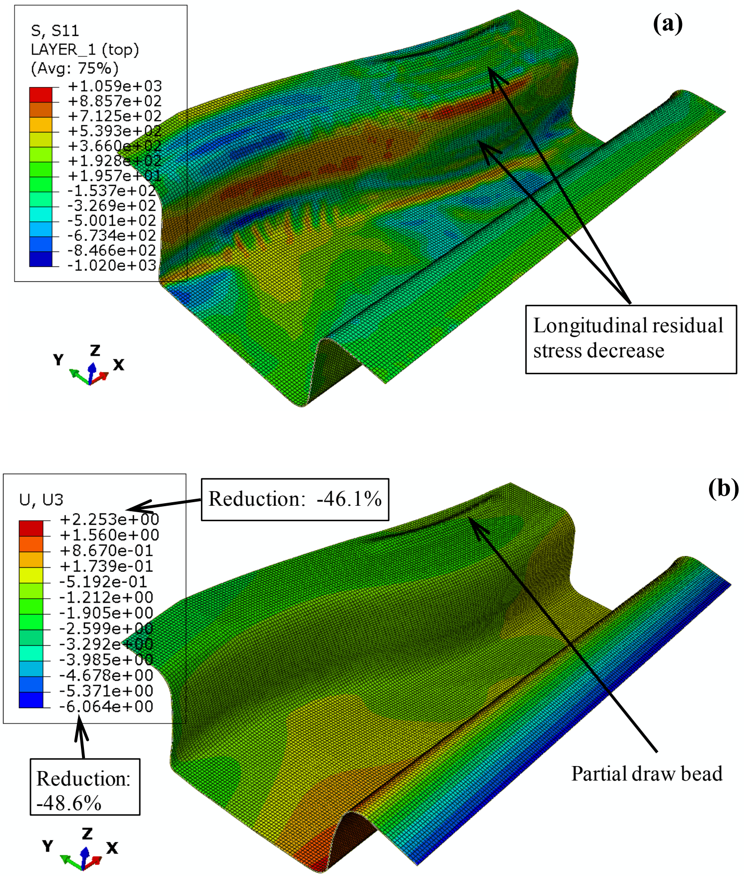

Figure 7-5 Simulation results by using the partial draw bead: (a) The global in-plane longitudinal stress distribution of DP780 (b) displacement springback along Z-direction (U3).

Figure 7-5 shows the simulation results of the global in-plane longitudinal stress distribution and displacement springback by using the partial draw bead. It can be observed that the longitudinal stress in the narrow transition regions reduce significantly. The partial draw bead proves to be effective at controlling the residual stress in specific portions of walls and the flanges. The maximum positive and negative displacement springback in the Z-direction are reduced by 46.1% and 48.6% respectively. The overall balance of springback is improved.

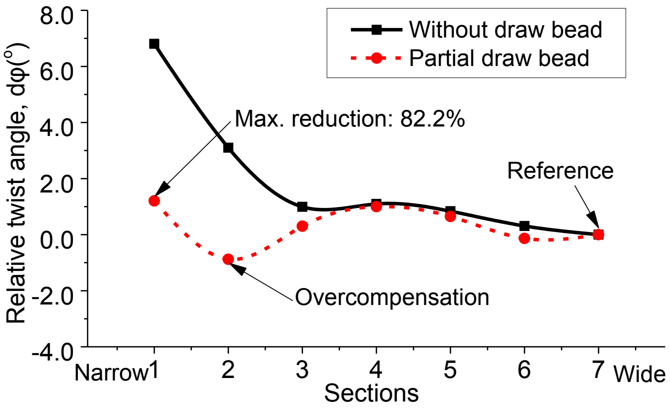

Figure 7-6 Comparison results of relative twist springback angle without and with partial draw bead based on simulation results.

Figure-7-6 shows the effects of the presented partial draw bead to rectify the twist problem obtained in deep drawing of P-channel case. The maximum reduction of relative twist angle at the narrow section can be achieved to 82.2%, although there is a slight overcompensation at section 2. The results indicate that it is possible to adequately control the residual stress and avoid forming problems by using partial draw bead. It also became clear, however, that the effects of this control strategy were dependent not only on the section shapes of partial bead position, but also its position where they were applied. Therefore, it is essential to clarify the related factors and study the effects of each measure thoroughly before actually applying them.

7.3 Asymmetric thin-walled tube

7.3.1 Mandrel nose placement (MNP)

In MRDB, the tube wall will thicken along the inside radius (intrados) and will thin along the outside radius (extrados) as the clamps draw the tube around the bend die. The purpose of the mandrel nose is to cover this region of flowing material and ensure a consistently round cross section by mitigating the simultaneous compression and stretching of the tube wall. As one scheme, the mandrel in a too far forward position stretches the material on the outside of the bend more than necessary. This increases the length of material on the outside beyond what is required to make a bend. Figure 7-7a is an exaggerated example. Bumps appear on the extrados of the bend and are most evident at the end of bend. A step may begin to appear on the intrados at the start of the bend. On the other hand, the mandrel in a too far back forward does not adequately stretch the material on the outside of the bend and generate enough pressure on the inside of the bend to compress the material. This may lead to form a wrinkle or wave on the intrados of the tube, as shown in Figure 7-7b. Therefore, the mandrel nose placement (MNP) relative to the point of bend or the line of tangency, as shown in Figure 7-7c, not only affects the stress and deformation state of the bent tube but also the degree of springback.

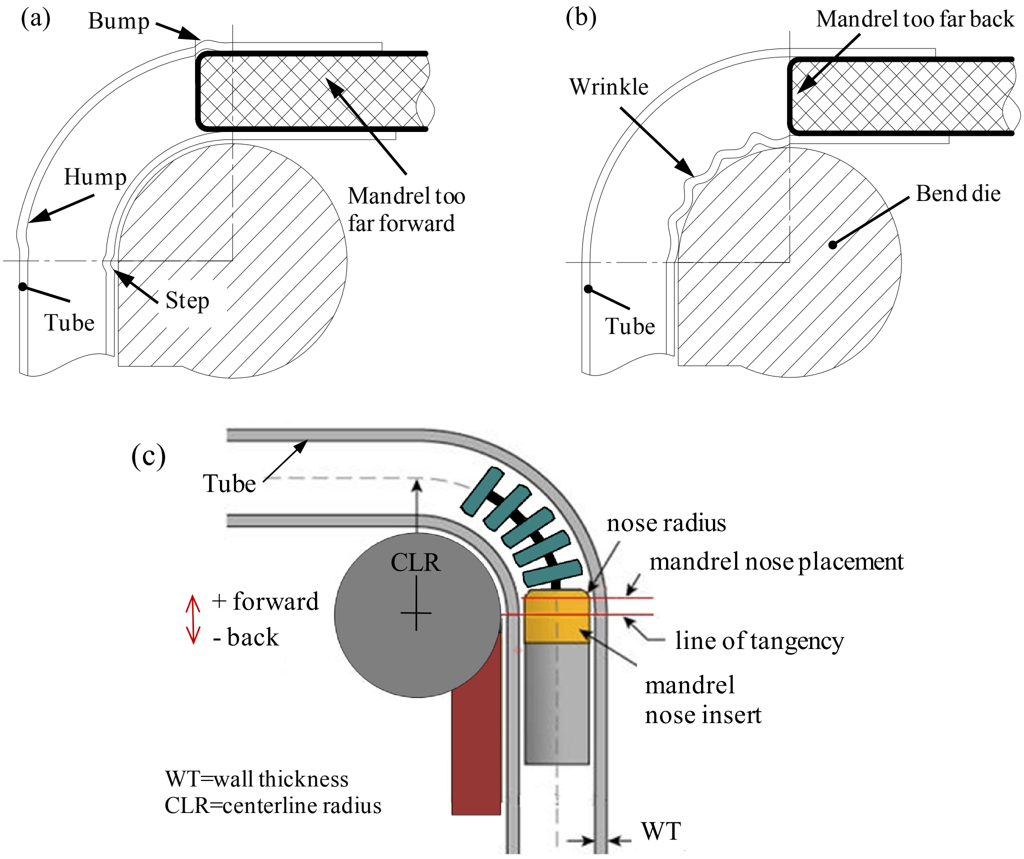

Figure 7-7 (a) The mandrel in a too far forward position (b) the mandrel in a too far back position (c) illustration of mandrel nose placement.

Several forward MNP were introduced into the FE model and tested the feasibility for the control of twist springback. The range of the MNP change is from 0 to 10mm, and there are almost no undesirable defects mentioned above. Figure 7-8 shows the comparison of the predicted twist springback by using different MNP in the case of 45° bending thin-walled tube. It can be observed that the springback angle is firstly slight increased and then decreased. This might be because the first increase of MNP aggravates the large deformations on the extrados side including the rate of elastic deformation, which leads to the larger springback. The further increase of MNP may mitigate the intrados compression deformation and then cause the decrease of springback. The MNP also makes an important effect on the ovalisation or distortion of the close section. For the twist deformation in the flange, no remarkable difference was observed between the situations.

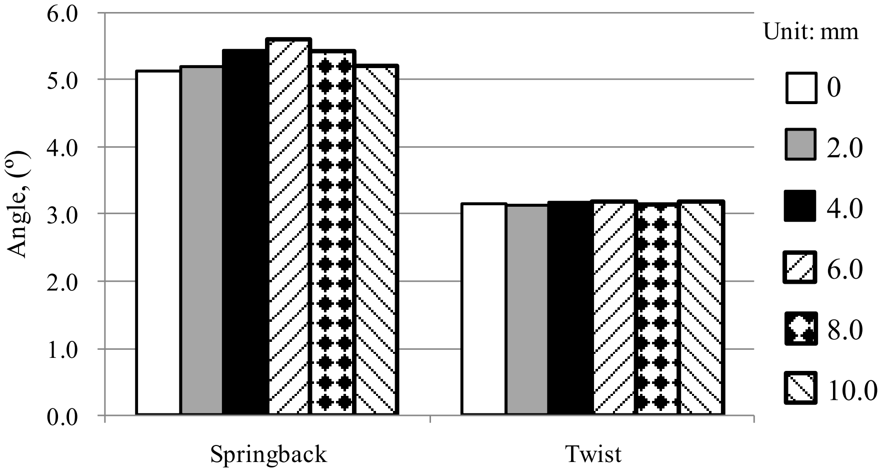

Figure 7-8 Comparison of twist springback calculated by using different MNP.

7.3.2 Push assistant loading (PAL)

The booster, one of the movable pushing tools, can be used to apply the axial boosting force or push assistant loading (PAL) to the trailing end of the tube to control the flow state of tube materials. Figure 7-9 shows that there are five possible methods to apply the axial boosting force via booster:

(a) To provide the push assistant force directly at the trailing end of tube;

(b) To provide the push assistant force by the friction between booster and outer surface of tube;

(c) To combine the above two boosting methods to exert the boosting force;

(d) To provide the push assistant force by the friction between booster and inner surface of tube;

(e) To combine the first method and the fourth one to boost the tube. To evaluate the efficiency of the boosting method on springback control of thin-walled tube, the last boosting method with respect to different boosting force conditions was adopted based on the developed FE model.

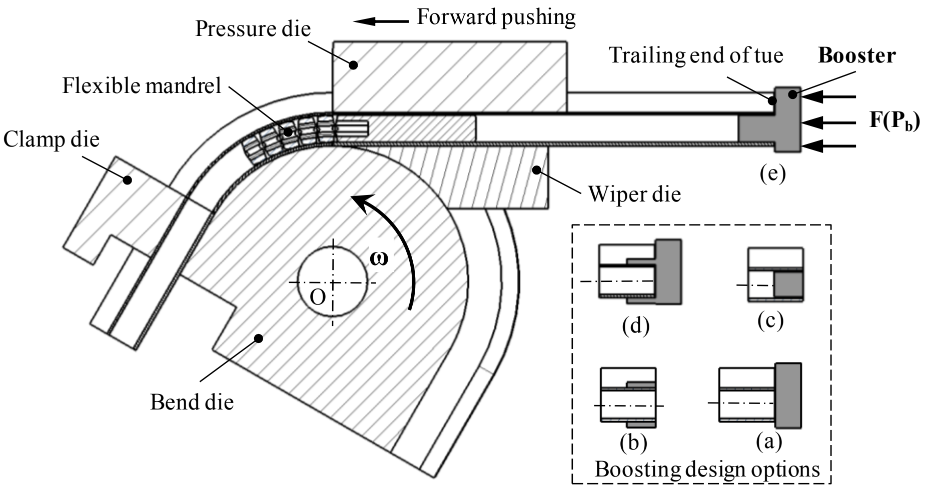

Figure 7-9 Sketch of boosting design options for push assistant loading in MRDB.

The PAL helps push the materials past the tangent point and into the bending regions, which decreases the tensile stress and makes the strain neutral line (NL) shift outwards, as shown in Figure 7-10. However, it might induce or aggravate the local wrinkling due to simultaneously induced excessive compressive stress at the intrados of tube. Thus it is necessary to study the interactive effects of PAL conditions on different defects such as wrinkling, wall thinning and twist springback.

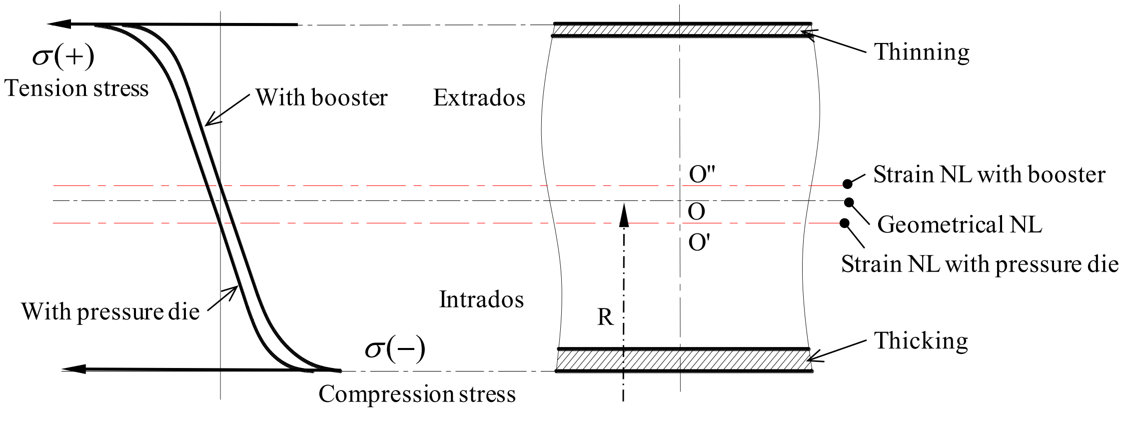

Figure 7-10 Stress distribution and strain neutral line change of the cross-section of bending tube under PAL conditions.

Four PAL conditions, 0.3MPa, 0.5MPa, 0.7MPa and 0.9MPa, were applied on the trailing end of the thin-walled tube during the MRDB. Figure 7-11 compares the maximum twisting and springback angles calculated by using different PAL conditions. It can be observed that 23.5% degradation of twisting deformation can be achieved by 0.9MPa PAL condition compared to no PAL condition. However, the compensation of springback of bending angle is not attained and even a slight increase is observed.

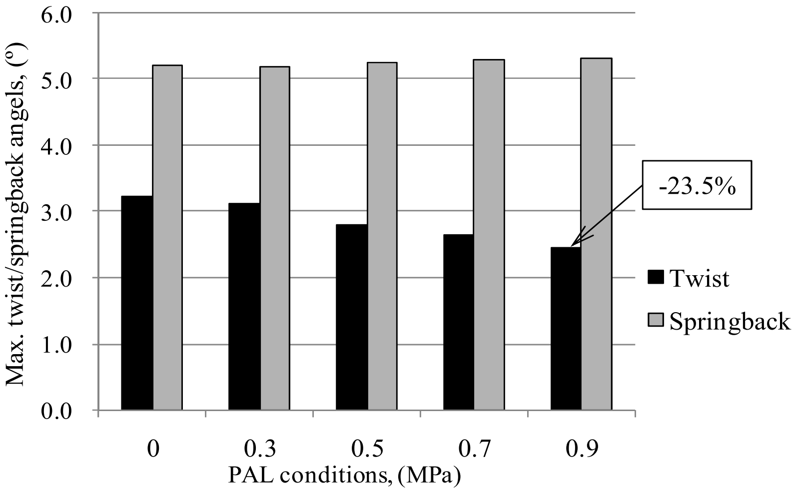

Figure 7-11 Comparison of twist springback calculated by different PAL conditions.

Figure 7-12 shows that the selected intrados and extrados sidewall thickness distributions were calculated by using different PAL conditions. The thickness of intrados sidewall increases with the increase of push assistant pressure, while that of extrados sidewall decreases. This means that the extrados sidewall has less deformation, but the risk of the wrinkle in the intrados sidewall rises.

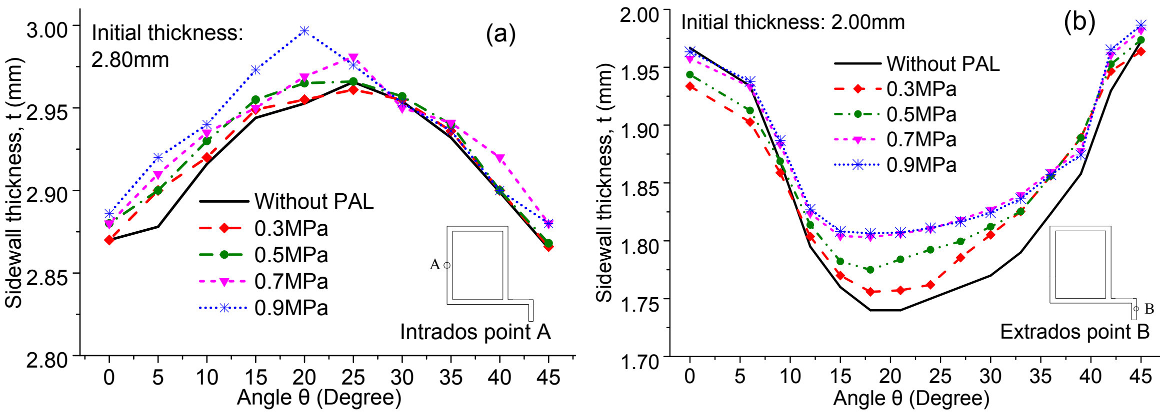

Figure 7-12 Comparison of the intrados and extrados sidewall thickness distributions calculated by using different PAL conditions.

Although the proposed PAL method seems not so high efficiency to reduce the twist deformation of the presented case, it provides an alternative method for the other possible industrial applications.

7.4 Partial conclusion

The FEA-based control strategy for the minimization of twist springback is presented. Certain regions of the die design are varied in a numerical analysis to reduce or eliminate the uneven torsion moment induced the twist springback in terms of AHSS channels. The optimization of mandrel nose placement and the application of push assistant loading are to assess the efficiency for the twist springback control in mandrel rotary draw bending of the presented asymmetric thin-walled tube. The principal conclusions are as follows:

- For C-channel, twist springback can significantly decreases by employing a variable die radius in the case of DP500 sheet. The maximum twist springback angles at the side and centre section are reduced by 46.2% and 24.5%, respectively. The relationship between the ratio of variable die radius and twist springback is explored for twist springback control. Design optimization using a variable die radius for the balance of extrados and intrados bending moment appears to be a valuable alternative to control twist springback of deep drawn curved channels.

- For P-channel, the partial draw bead proves to be effective at controlling the residual uneven longitudinal in-plane stress in certain region. It is an alternative method to reduce the twist springback of asymmetric channels.

- For thin-walled tube, the MNP mainly affect the springback but not twist deformation. The springback angle is firstly slight increased and then decreased after several forward MNP tests. This might be because the first increase of MNP aggravates the large deformations on the extrados side including the rate of elastic deformation, which leads to the larger springback. The further increase of MNP may mitigate the intrados compression deformation and then cause the decrease of springback. The PAL method is possible to reduce twist deformation, but the risk of springback of bending angle and wrinkle in the intrados sidewall also rises.

Chapter 8

Conclusions and future works

8.1 Final conclusions

The twist springback characteristics of lightweight automotive structures with complex cross-sectional shape were investigated by means of theoretical, experimental and numerical methods. The main conclusions of this dissertation are as follows.

Firstly, in order to ensure accurate modelling of twist springback, a reliable test data of material behaviours under various loading /unloading conditions are essential as well as appropriate constitutive models. The material characterization and the corresponding identification of constitutive parameters allow the following conclusions to be drawn:

- The yield function Yld2000-2d exactly captures both yield stress and r-value directionalities in uniaxial tension while the other yield criterion Hill'48 is limited to describe the anisotropy of stress and strain simultaneously.
- The HAH model well captures the complex material behaviours including the Bauschinger effect, transient hardening with high rate and permanent softening. The IH model overestimates the stress after load reversals, especially at the onset of load reversals. The IHKH model captures the Bauschinger effect, thus it gives a better description of the flow stress under load reversal than the IH model. However, it still cannot reproduce the permanent softening.
- The mechanical measurements of the nonlinear elastic modulus degradation of the DP steels are sensitive to the loading strategy. Among the three test methods considered, the highest elastic modulus degradation was obtained with the uniaxial loading strategy and the lowest with the biaxial loading strategy. The proposed TPB-P appears to be a good alternative method to determine the nonlinear elastic material behaviour. The choice of loading strategy for the determination of elastic modulus degradation should consider the deformation path and the other adopted constitutive models during the real forming process.

Secondly, two typical metal forming processes, deep drawing of DP steel sheets and rotary draw tube bending of aluminium alloy asymmetric thin-walled tube, were selected as subjects and studied cases due to their evident twist springback. A more reasonable definition of twist springback with respect to the principal inertia axes of the cross-sections was proposed. The relationship between torsion moment and twist angle was analysed to explain the occurrence of twist springback. Several key modelling techniques including the friction coefficient identification, surface-based coupling constraint for flexible mandrel using HINGE connector element and digital image correlation were performed for improving the robustness of the numerical models. The mechanism of twist springback was analysed from the evolution of in-plane stress and deformation history in the components after forming.

Thirdly, the sensitivities of material constitutive models to the accuracy of twist springback prediction were analysed and discussed. The influence of some deep drawing process and numerical parameters of tube bending on twist springback were provided.

- For the constitutive models: First, the prediction of twist springback can be improved significantly by considering the degradation of the elastic modulus. The elastic modulus has a considerable effect on the twist springback prediction. Second, all the simulations with Yld2000-2d yield criterion show evident advantage than the other yield criteria. As for tube bending case, compared to springback angle, the twist deformation seems more sensitive to yield criterion. Third, the HAH model for the prediction of the twist springback of P-channel and C-channel overall seems to be better than the IH and IHKH models, although it still has a slight deviation compared to experimental result. For asymmetric thin-walled tube, the twist deformation in the flange is less sensitive to the hardening model than the springback angle.
- For deep drawing process parameters: Material direction of initial blank is very sensitivity to twist springback in case of DP500 C-channel. Blank piercing is also shown to significant effect on the final geometry of the curved C-rail drawn part, although it had little effect on the thickness reduction. It seems like better lubricant leads to less springback to some extent. However, it is difficult to find a further relationship between global twist springback and lubrication condition.
- For numerical parameters of tube bending: The present surface-based coupling HINGE model for mandrel flexible constraint has the highest precision than the others. The sensitivity analysis of interfacial friction on twist springback shows that the large friction should be applied to the interface between tube and pressure die to reduce the twist springback. It also provides guidelines for applying the

tribological conditions to establish the robust bending condition for stable and precise manufacturing of tubes.

Finally, two control strategies, variable die radius and partial draw bead design, were proposed to reduce the twist springback of the C-channel and the P-channel, respectively. As for the tube bending, optimization of mandrel nose placement and push assistant loading were presented to assess the efficiency for the twist springback control. These FEA-based control strategies appear to be alternative methods to reduce the unbalance torsion moment and the twist springback in terms of individual case.

8.2 Future works

The following topics are considered as potentially future works:

- The influence of strain path changes on the non-linear elastic behaviour and its microscopic mechanisms should be further investigated as well as the anisotropic elastic behaviour related to twist springback.
- For better description of the complex material behaviours and the improvement of prediction accuracy, more advanced constitutive models and the corresponding non-proportional loading tests would be considered. For example, the adoption of the enhanced HAH model. Extension of the existing chord model or QPE model to make them better describing the nonlinear elastic behaviour could be an additional topic for future research.
- The solid element or the mixed solid-shell element might be adopted for the calculation of the torsion moment in a cross section. The modification of shell elements, which make them capable of behaving accurately in the regions with fully three-dimensional stress state, can be another interesting approach.
- Other potential factors affecting twist springback might be further investigated. The interaction effects between springback and other undesirable defects, e.g., wrinkle, should be further investigated.
- Of particular interest and complexity are the twist springback characteristics in the other metal forming processes such as incremental sheet metal forming, porthole hot extrusion, joining of dissimilar metal, and so on.

- More control strategies for the minimization of twist springback, e.g., tool design related to additional geometric stiffener, will be addressed in terms of individual forming case.

References

ABAQUS, Reference Manuals, (2011), Hibbit, Karlsson, and Sorensen, Inc.

Abdullah A.B., Salit M.S., Samad Z., MTandoor. K.H., Aziz N.A. (2013). Twist springback measurement of autonomous underwater vehicle propeller blade based on profile deviation. Am. J. Appl. Sci. 10(5): 515-524.

Alaoui A.H., Woignier T., Scherer G.W., Phalippou J. (2008). Comparison between flexural and uniaxial compression tests to measure the elastic modulus of silica aerogel. J. Non. Cryst. Solids. 354: 4556–4561.

Andar M.O., Kuwabara T., Yonemura S., Uenishi A. (2010). Elastic–plastic and inelastic characteristics of high strength steel sheets under biaxial loading and unloading. ISIJ Int. 50: 613-619.

Armstrong P.J, Frederick C.O. (1966). A mathematical representation of the multi-axial Bauschinger effect. G.E.G.B report RD/B/N 731.

Atkinson M. (1997). Accurate determination of biaxial stress-strain relationships from hydraulic bulging tests of sheet metals. International Journal of Mechanical Sciences 39(7): 761-769.

Banabic D., Barlat F., Cazacu O., Kuwabara T. (2010). Advances in Anisotropy and Formability. Int. J. Mater. Form. 3: 165-189. doi: 10.1007/s12289-010-0992-9.

Barlat F., Brem J.C., Yoon J.W., Chung K., et al. (2003). Plane stress yield function for aluminium alloy sheets—Part I: theory. Int. J. Plast. 19:1297–1319.

Barlat F., Aretz H., Yoon J.W., Karabin M.E., Brem J.C., Dick R.E. (2005) Linear transformation-based anisotropic yield functions. Int. J. Plast. 21:1009–1039.

Barlat F., Gracio J.J., Lee M.-G., Rauch E.F., Vincze G. (2011). An alternative to kinematic hardening in classical plasticity. Int. J. Plast. 27 (9): 1309–1327.

Barlat F., Ha J., Gracio J.J., Lee M.G., Rauch E.F., Vincze G. (2012). Extension of homogeneous anisotropic hardening model to cross-loading with latenteffects. Int. J. Plast. 46: 130-142.

Bernert. W., et al. (2010). Advanced high-strength steel applications design and stamping process guidelines. Auto/Steel Partnership, Southfield, Michigan.

Bergström Y., Granbom Y., Sterkenburg D. (2010). A dislocation-based theory for the deformation hardening behaviour of DP steels: Impact of martensite content and ferrite grain size. J. Metall., Article ID 647198, 16 pages. doi:10.1155/2010/647198.

Boesemann W., Godding R., Huette H. (2000). Photogrammetric measurement techniques for quality control in sheet metal forming. Int. Arch. Photogram. Rem. Sen. B5: 291-299.

Boger R.K. (2006). Non-Monotonic strain hardening and its constitutive representation. PhD. Dissertation. The Ohio State University.

Böhlke T, Bertram A. (2003). Asymptotic values of elastic anisotropy in polycrystalline copper for uniaxial tension and compression. Comput. Mater. Sci. 26: 13-19.

Bower A.F. (1989). Cyclic hardening properties of hard-drawn copper and rail steel. J. Mech. Phys. Solids 37: 455–470.

Buranathiti T., Cao J. (2004). An effective analytical model for springback prediction in straight flanging processes. Int. J. Mater. Prod. Technol. 21:137-153.

Burchitz I.A., Meinders T. (2008). Adaptive through-thickness integration for accurate springback prediction.

Int. J. Numer. Meth. Eng. 75 (5): 533–554.

Cai M., Field D.P., Lorimer G.W. (2004). A systematic comparison of static and dunamic aging of two Al-Mg-Si alloys. Mater. Sci. Eng. A 373: 64-71.

Cao J., Kinsey B., Solla S.A. (2000). Consistent and minimal springback using a stepped binder force trajectory and neural network control. ASME J. Eng. Mater. Technol. 122:113-118.

Chaboche J.L. (1986). Time-independent constitutive theories for cyclic plasticity. Int. J. Plast. 2:149–188.

Chatti S, Hermi N. (2011).The effect of non-linear recovery on springback prediction. Comput. Struct. 89: 1367–1377.

Chatti S. (2013). Modeling of the elastic modulus evolution in unloading-reloading stages, Int. J. Mater. Form. 6: 93–101.

Chatti S., Fathallah R. (2014). A study of the variations in elastic modulus and its effect on springback prediction. Int. J. Mater. Form. 7: 19-29.

Chen Z., Gandhi U., Lee J.W., Wagoner R.H. (2016). Variation and consistency of Young's modulus in steel. J. Mater. Process. Technol. 227: 227–243.

Cheng H.S., Cao J., Xia Z.C. (2007). An accelerated springback compensation method. Int. J. Mech. Sci. 49 (3), 267–279.

Cheng M. (2010). Effect of Preheating Condition on Strength of AA6060 Aluminium Alloy for Extrusion. Master thesis. Auckland University of Technology. New Zealand.

Chongthairungruang B., Uthaisangsuk V., Suranantchai S., Jirathearanat S. (2011). Influence of pre-deformation on the springback effect of advanced high strength steel. J. Iron Steel. Res. Int. 18: 855–861.

Chun B.K., Jinn J.T., Lee J.K. (2002). Modeling the Bauschinger effect for sheet metals, part I: theory. Int. J. Plast. 18: 571–595.

Chung K., Yoon J.W., Richmond O. (2000). Ideal sheet forming with frictional constraints. Int. J. Plast. 16: 595–610.

Chung K., Lee M.-G., Kim D., Kim C., Wenner M.L., Barlat F. (2005). Spring-back evaluation of automotive sheets based on isotropic–kinematic hardening laws and non-quadratic anisotropic yield functions. Part I: theory and formulation. Int. J. Plast. 21: 861–882.

Cleveland R, Ghosh A. (2002). Inelastic effects on springback in metals. Int. J. Plast.18: 769–785.

Dafalias YF, Popov EP. (1976). Plastic internal variables formalism of cyclic plasticity. T-ASME, J. Appl. Mech. 98: 645-651.

Damoulis G. L., Gomes E., G. BatalhaF. (2010). New trends in sheet metal forming analysis and optimization trough the use of optical measurement technology to control springback. Int. J. Mater. Form. 3(1): 29-39.

Desombre, J., et al. (2011). Experimentally validated FEA models of HF2V damage free steel connections for use in full structural analyses. Struct. Eng. Mech. 37: 385-400.

Dezelak M., Stepisnik A., Pahole I., Ficko M. (2014). Evaluation of twist springback prediction after an AHSS forming process. Int. J. Simul. Model. 13: 171-182.

Dwivedi J.P., Upadhyay P.C., Talukder N.K. D. (1992). Springback analysis of torsion of L-sectioned bars of work-hardening material. Comput. Struct. 43(5): 815-822.

Dwivedi J. P., Shah S. K., Upadhyay P.C., Talukder N. K. D. (2002). Springback analysis of thin rectangular bars of non-linear work hardening material. Int. J. Mech. Sci. 44, 1505-1519.

Eggertsen P.A., Mattiasson K. (2009). On the modelling of the bending–unbending behaviour for accurate springback predictions. Int. J. Mech. Sci. 51(7): 547–563.

Eggertsen P.A., Mattiasson K. (2010). On constitutive modeling for springback analysis. Int. J. Mech. Sci. 52(6): 804–818.

Eggertsen P.A and Mattiasson K. (2012). Experiences from experimental and numerical springback studies of a semi-industrial forming tool. Int. J. Mater. Form. 5: 341-359.

Emil E., Andrej H., Jana T. (2001). Measurement and evaluation of friction ratios at deep drawing. J. Technol. Plast. 2: 81-88.

ESI/PSI. (1995). User manual for PAM-STAMP, Paris, France.

Esat V., Darendeliler H., Gokler M.I. (2002). Finite element analysis of springback in bending of aluminium sheets. Mater. Des. 23: 223–229.

Fedorov V. (2012). Bend-twist coupling effect in wind turbine blades. PhD. Dissertation. Technical University of Denmark, Lyngby, Denmark.

Gan W., Wagoner R.H., (2004). Die design method for sheet springback. Int. J. Mech. Sci. 46 (7): 1097–1113.

Gangwar M., Choubey V.K., Dwivedi J.P., Talukder N. K. D. (2011). Springback Analysis of Thin Tubes with Arbitrary Stress-Strain Curves. J. Mech. Eng. 8(1): 57-76.

Garcia D., Orteu J. J., Penazzi L. (2002). A combined temporal tracking and stereo-correlation technique for accurate measurement of 3D displacements: application to sheet metal forming. J. Mater. Process. Technol. 125: 736-742.

Geng L, Wagoner RH. (2000). Springback analysis with a modified hardening model. SAE paper No. 2000-01-0768, SAE, Inc.

Geng L, Shen Y, Wagoner R H. (2002). Anisotropic hardening equations derived from reverse-bend testing. Int. J. Plast.18:743–67.

Geka T., et al. (2013). Reduction of springback in hat channel with high-strength steel sheet by stroke returning deep drawing. Key Eng. Mater. 554-557: 1320-1330.

Ghaei A., Green D.E., Taherizadeh A., (2010). Semi-implicit numerical integration of Yoshida–Uemori two-surface plasticity model. Int. J. Mech. Sci. 52 (4): 531–540.

Ghaei A., Green D.E., Aryanpour A. (2015). Springback simulation of advanced high strength steels considering nonlinear elastic unloading–reloading behavior. Mater. Des. 88: 461-470.

Govik A., Rentmeester R., Nilsson L. (2014). A study of the unloading behaviour of dual phase steel. Mater. Sci. Eng. A; 602: 119–126.

Guner A., Soyarslan C., Brosius A., Tekkaya A.E. (2012). Characterization of anisotropy of sheet metals employing inhomogeneous strain fields for Yld2000-2D yield function. Int. J. Solid Struct. 49: 3517-3527.

Ha J. J., Lee M.G., Barlat F. (2013). Strain hardening response and modeling of EDDQ and DP780 steel sheet under non-linear strain path. Mech. Mater. 64: 11-26.

Haddadi H., Bouvier S., Banu M., Maier C., Teodosiu, C. (2006). Towards an accurate description of the anisotropic behavior of sheet metals under large plastic deformation: modelling, numerical analysis and identification. Int. J. Plast. 22: 2226–2271.

Hannon A., Tiernan P. (2008). A review of planar biaxial tensile test systems for sheet metal, J. Mater. Process. Technol. 198: 1-13

Hassan H., Maqbool F., Güner A., Hartmaier A., Khalifa N.B., Tekkaya A.E. (2015). Springback prediction and reduction in deep drawing under influence of unloading modulus degradation. Int. J. Mater. Form. 5: DOI 10.1007/s12289-015-1248-5.

Hershey, A.V. (1954). The plasticity of an isotropic aggregate of anisotropic face centred cubic crystals, J. Appl. Mech. 21, 241–249.

Hill R. (1948). A theory of the yielding and plastic flow of anisotropic metals. Proceedings of the Royal Societies of London; A193:145–85.

Hishida Y., Wagoner R.H. (1993). Experimental Analysis of Blank Holding Force Control in Sheet Forming. J. Mater. Manu. 2:409-415.

Hodge P.G. (1957). A new method of analyzing stresses and strains in work hardening solids. T-ASME, J. Appl. Mech. 24: 482–496.

Holmedal B., Houtte P.V., An, Y. (2008). A crystal plasticity model for strain-path changes in metals. Int. J. Plast. 24: 1360–1379

Huang M., Brouwer J. (2005). Characterization and control of the springback of advanced high strength steel. In: Proceedings of the Materials Science and Technology Conference 4: 3-14.

Iyama T., et al. (2003). Twist resulting in high strength steel sheet hat channel product consisting of straight portion combined with curved portion. Int. J. Mech. Eng. 46(3): 419-425.

Ito K., Kondou T., Uemura G., Mori N. (2007). New method to evaluate and compensate 3D springback. Numiform07. AIP Conf. Proc. 978: 1477-1482.

Jiang Z.Q., Yang H., Zhan M., Xu X. D., Li G. J. (2010). Coupling effects of material properties and the bending angle on the springback angle of a titanium alloy tube during numerically controlled bending, Mater. Des. 31: 2001–2010.

Karafillis A.P., Boyce, M.C. (1996). Tooling and binder design for sheet metal forming processes compensating springback error. Int. J. Mach. Tool. Manu. 36 (4): 503–526.

Kennedy J, Eberhart R. (1995). A new optimizer using particle swarm theory. In:Proceedings of the sixth international symposium on micro machine and human science, Nagoya , Japan, pp. 39–43.

Kim H., Kimchi M., Kardes N., Altan T. (2011). Effects of variable elastic modulus on springback predictions in stamping advanced high-strength steels (AHSS). In: Proceeding of 10th International Conference on Technology of Plasticity, ICTP 2011, Sep. 25-30, Aachen, Germany.

Kim H., Kim C., Barlat F., Pavlina E., Lee M.G. (2013). Nonlinear elastic behaviors of low and high strength steels in unloading and reloading. Mater. Sci. Eng. A; 562: 161–171.

Kim J.H., Kim D., Barlat F., Lee M.G. (2012). Crystal plasticity approach for predicting the Bauschinger effect in dual-phase steel. Mater. Sci. Eng. A; 539: 259–270.

Kim J.H., Kim Y.Y. (2000). One-dimensional analysis of thin-walled closed beams having general cross-sections. Int. J. Numer. Meth. Eng. 49: 653-668.

Kim Y.Y, Kim Y. (2002). A one-dimensional theory of thin-walled curved rectangular box beams under torsion and out-of-plane bending. Int. J. Numer. Meth. Eng. 53: 1573-1595.

Komgrit L., Hamasaki H., Hino R., Yoshida F. (2016). Elimination of springback of high-strength steel sheet by using additional bending with counter punch. J. Mater. Process. Technol. 229:199–206.

Kourtis L., Carter D., Beaupre G. (2014). Improving the estimate of the effective elastic modulus derived from three-point bending tests of long bones. Ann. Biomed. Eng. 42: 1773-1780.

Ku T.W., Lim H.J., Choi H.H., Hwang S.M., Kang B.S. (2001). Implementation of backward tracing scheme of the FEM to blank design in sheet metal forming. J. Mater. Process. Technol. 111: 90–97.

Kuwabara T., Ikeda S., Kuroda T. (1998). Measurement and analysis of differential work hardening in cold-rolled steel sheet under biaxial tension. J. Mater. Process. Technol. 80: 517-523.

Kuwabara T., Bael A.V., Iizuka E. (2002). Measurement and analysis of yield locus and work hardening characteristics of steel sheets wtih different r-values. Acta. Mater. 50: 3717-3729.

Laurent, H., Greze, R., Manach, P. Y., Thuillier, S. (2009). Influence of constitutive model in springback prediction using the split-ring test. Int. J. Mech. Sci. 51, 233-245.

Lee K.C., Jhang J.Y. (2006). Application of particle swarm algorithm to the optimization of unequally spaced antenna arrays. J. Electromagnet Wave. 20(14): 2001–2012.

Lee M.G., Kim, D., Kim, C., Wenner M.L., Chung, K. (2005). Springback evaluation of automotive sheets based on isotropic-kinematic hardening laws and non-quadratic anisotropic yield functions, part III: applications. Int. J. Plast. 21: 915-953.

Lee M.G., Kim D., Wagoner R.H., Chung K. (2007). Semi-analytic hybrid method to predict springback in the 2D draw bend test. J. Appl. Mech. T- ASME. 74:1264-1275.

Lee M.G., Kim J.H., Chung K., Kim S.J., Wagoner R.H., Kim H.Y. (2009). Analytical springback model for lightweight hexagonal close-packed sheet metal. Int. J. Plast. 25:399-419.

Lee J.W., Lee M.G., Barlat F. (2012a). Finite element modelling using homogeneous anisotropic hardening and application to spring-back prediction. Int. J. Plast. 29: 13-41.

Lee J.W., Lee J.Y., Barlat F., Wagoner R.H., Chung K., Lee M.G. (2013). Extension of quasi-plastic–elastic approach to incorporate complex plastic flow behavior—application to springback of advanced high-strength steels. Int. J. Plast. 45: 140–159.

Lee J.Y., Lee J.W., Lee M.G., Barlat F. (2012b). An application of homogeneous anisotropic hardening to springback prediction in pre-strained U-draw/bending. Int. J. Solids. Struct. 49(25): 3562-3572.

Lee S.W, Yang D.Y. (1998). An assessment of numerical parameters influencing springback in explicit finite element analysis of sheet metal forming process. J. Mater. Process. Technol. 80: 60–67.

Leotoing L., Guines D. (2015). Investigations of the effect of strain path changes on forming limit curves using an in-plane biaxial tensile test. Int. J. Mech. Sci. 99: 21-28.

Li B.J, Zhang X.K., Zhou P., Hu P. (2010). Mesh parameterization based on one-step inverse forming. Compu. Aid. Des.; 42: 633-640.

Li, H., Yang, H., Zhan, M., Sun, Z.C., Gu, R.J. (2007). Role of mandrel in NC precision bending process of thin-walled tube. Int. J. Mach. Tool. Manu. 47: 1164–1175.

Li H., Yang H., Zhang Z.Y, Wang Z.K. (2012). Size effect related bending formability of thin-walled aluminium alloy tube. Chin. J. Aeronaut. 26(1): 230–241.

Li H.Z., Sun G.Y., Li G.Y., Gong Z.H., Liu D.H., Li M. (2012). On twist springback in advanced high strength steels. Mater. Des. 32(6): 3272–3279.

Li K.P., Carden W.P., Wagoner R.H. (2002). Simulation of springback. Int. J. Mech. Sci. 44: 103-122.

Liao J., Xue X., Zhou C., Gracio J.J., Barlat F. (2013). A Springback Compensation Strategy and Applications to Bending Cases. Steel Res. Int. 84(5): 462-472.

Liao J., Xue X., Lee M.G., Barlat F., Gracio J. (2014). On twist springback prediction of asymmetric tube in rotary draw bending with different constitutive models. Int. J. Mech. Sci. 89: 311-322.

Liao J., Xue X., Lee M.G., Barlat F., Vincze G., Pereira A.B. (2016). Constitutive modelling for path-dependent behaviour and its influence on twist springback in channel forming. Int. J. Plast. submitted.

Lin, Z.C., Chen, C.K. (200). Inverse calculation of the friction coefficient during the warm upsetting of molybdenum. Int. J. Mech. Sci. 47: 1059-1078.

Lingbeek R.A, Huetnik J., Ohnimus S., Petzoldt M. (2005). The development of a finite elements based springback compensation tool for sheet metal products. J. Mater. Process. Technol. 169: 115–125.

Lingbeek R.A., Meinders T., Ohnimus S., Petzoldt M., Weiher J. (2006). Springback Compensation: Fundamental Topics and Practical Application. In: ninth ESAFORM conference on Material Forming, April 2006, Glasgow, U.K , pp. 403-406.

Lingbeek R.A., Gan W., Wagoner R.H., Meinders T., Weiher J.(2008). Theoretical verification of the displacement adjustment and spring forward algorithms for springback compensation. Int. J. Mater. Form. 1: 159-168.

Liu G., Lin Z., Bao Y., Cao J. (2002). Eliminating springback error in U-shaped part forming by variable blank holder force. J. Mater. Eng. Perform. 11:64-70.

Liu, J., Yang, H., Zhan, M., Jiang, Z. Q., (2012). Accurate prediction of the profile of thick-walled titanium alloy tube in rotary-draw bending considering strength-differential effect. Comp. Mater. Sci. 60, 113-122.

Liu W., Guines D., Leotoing L., Ragneau E. (2015). Identification of sheet metal hardening for large strains with an in-plane biaxial tensile test and a dedicated cross specimen. Int. J. Mech. Sci. 101-102: 387-98.

Lourakis M.I.A. (2005). A brief description of the Levenberg-Marquardt algorithm implemented by levmar. Technical Report, Institute of Computer Science, Foundation for Research and Technology – Hellas, Greece.

Luo M., Dunand M., Mohr D. (2012). Experiments and modeling of anisotropic aluminum extrusions under multi-axial loading-Part I: Plasticity. Int. J. Plasticity 36, 34-49.

Martins, B., Santos, A. D. , Teixeira, P. , Ito, K., Mori, N. (2013). Determination of Flow Curve Using Bulge Test and Calibration of Damage for Ito-Goya Models. Key Eng. Mater. 182: 554-557.

Mattiasson K., Sigvant M. (2008). An evaluation of some recent yield criteria for industrial simulations of sheet forming processes. Int. J. Mech. Sci. 50: 774-787.

Mendiguren J., Cortés F., Gómez X., Galdos L. (2015). Elastic behaviour characterisation of TRIP 700 steel by means of loading–unloading tests. Mater. Sci. Eng. A; 634: 147–152.

Miller, J. E., Kyriakides, S., Bastard, A.H., 2001. On bend-stretch forming of aluminum extruded tubes-I: experiments. Int. J. Mech. Sci. 43: 1283-1317.

Miller, J. E., Kyriakides, S., 2003. Three-dimensional effects of the bend-stretch forming of aluminum tubes. Int. J. Mech. Sci. 45: 115-140.

Mroz Z. (1967). On the description of anisotropic work hardening. J. Mech. Phys. Solids 15:163–175.

Oliveira, D.A., Worswick, M.J., Grantab, R. (2005). Effect of lubricant in mandrel-rotary draw tube bending of steel and aluminum. Canadian Metallurgical Quarterly 44, 71–78.

Oliveira M.C., Alves J.L., Chaparro B.M., Menezes L.F. (2007). Study on the influence of work-hardening modeling in springback prediction. Int. J. Plast. 23: 516–543.

Pavlina E.J., Lin C., Mendiguren J., Rolfe B.F., Weiss M. (2015a). Effects of microstructure on the variation of the unloading behavior of DP780 steels. J. Mater. Eng. Perform. 24: 3737-45 .

Pavlina E.J., Lee M.G., Barlat F. (2015b). Observations on the nonlinear unloading behavior of advanced high strength steels. Metall. Mater. Trans. A; 46: 18-22.

Pham C.H., Thuilier S., Manach P.Y. (2014). Twisting analysis of ultra-thin metallic sheets. J. Mater. Process. Technol. 214: 844-855.

Prager W. (1956). A new method of analysing stresses and strains in work hardening plastic solids. J. Appl. Mech. 23: 493–496.

Rauch E.F. (1998). Plastic anisotropy of sheet metals determined by simple shear tests. Mater. Sci. Eng. A; 241, 179-183.

Rauch E.F., Gracio J., Barlat F. (2007). Working-hardeningmodel for polycrystalline metals under strain reversal at large strains. Acta Mater. 55: 2939-2948

Santos A.D., et al. (2002). Towards standard benchmarks and reference data for validation and improvement of numerical simulation in sheet metal forming. J. Mater. Process. Technol.125-126: 798-805.

Schmitt J.H., Aernoudt E., Baudelet B. (1985). Yield loci for polycrystalline metals without texture. Mater. Sci. Eng. A; 75: 13-20.

Shima M. (2011). Torsion and shear stresses in ship. Springer-Verlag GmbH.

Sousa J.A., Pereira A.B., Martins A.P., Morais A.B. (2015). Mode II fatigue delamination of carbon/epoxy laminates using the end-notched flexure test. Compos. Struct. 134: 506-512.

Sun G.Y., et al. (2010). Multi objective robust optimization method for drawbead design in sheet metal forming. Mater. Des.31, p1913-1929.

Sun L., Wagoner R.H. (2011). Complex unloading behavior: Nature of the deformation and its consistent constitutive representation. Int. J. Plast. 27: 1126-1144.

Sun L., Wagoner R.H. (2013). Proportional and non-proportional hardening behavior of dual-phase steels. Int. J. Plast. 45: 174–187.

Sunseri M., Cao J., Karafillis A.P., Boyce M.C. (1996). Accommodation of Springback Error in Channel Forming Using Active Binder Force Control: Numerical Simulations and Results. ASME J. Eng. Mater. Technol.118:426–435.

Takamura et al. (2011). Investigation on twisting and side wall opening occurring in curved hat channel products made of high strength steel sheets. The 8th International Conference and Workshop on

Numerical Simulation of 3D Sheet Metal Forming Processes. AIP Conf. Proc. 1383, 887-894.

Tang B.T., Lu X.Y., Wang Z.Q., Zhao Z. (2010). Springback investigation of anisotropic aluminum alloy sheet with a mixed hardening rule and Barlat yield criteria in sheet metal forming. Mater. Des. 31, 2043-2050.

Tang N.C. (2000). Plastic deformation analysis in tube bending. Int. J. Pres. Ves. Pip. 77, 751–759.

Teodosiu C., Hu Z. (1998). Microstructure in the continuum modeling of plastic anisotropy. In: Proceedings of the Risø International Symposium on Material Science. Modelling of Structure and Mechanics of Materials from Microscale to products, Denmark, pp. 149–168.

Thuillier S., Manach P.Y., Menezes L.F. (2010). Occurence of strain path changes in a two-stage deep drawing process. J. Mater. Process. Technol. 210:226–232.

Vladimirov I.N., Reese S. (2012). Material modelling of evolving elastic and plastic anisotropy with application to deep drawing processes. In Blucher Mechanical Engineering Proceedings of 10th World Congress on Computational Mechanics, 8-13 July, Sao Paulo, Brazil.

Vladimirov I.N., Pietryga M.P., Reese S. (2010). Anisotropic finite elastoplasticity with nonlinear kinematicand isotropic hardening and application to sheet metal forming. Int. J.Plast. 26:659-687.

Vincze G. (2007). Investigation methodologies for metals used in forming processes. PhD. Dissertation. University of Aveiro, Portugal.

Vrh M., Halilovič M., Štok B. (2011). The evolution of effective elastic properties of a cold formed stainless steel sheet. Exp. Mech. 51: 677-695.

Vrh M., Halilovič M., Starman B., Stok B., Comsa D-S., Banabic D. (2014). Capability of the BBC2008 yield criterion in predicting the earing profile in cup deep drawing simulations. Eur. J. Mech. A-Solids. 45: 59-74.

Wagoner R.H., Li M. (2007). Simulation of springback: Through-thickness integration. Int. J. Plast. 23:345-360.

Wagoner R.H, Lim H., Lee M.G. (2013). Advanced Issues in springback. Int. J. Plast.45: 3-20

Wang H.B, Yan Y., Wan M., Wu X.D. (2012). Experimental investigation and constitutive modeling for the hardening behaviorof 5754O aluminum alloy sheet under two-stage loading. Int. J. Solids. Struct. 49: 3693-3710.

Wijskamp S. (2005). Shape distortion in composites forming. PhD Dissertation. University of Twente, Enschede, Netherlands.

Xu S., Zhao K., Lanker T., Zhang J., Wang C.T. (2005). Springback Prediction, Compensation and Correlation for Automotive Stamping. NUMISHEET2005. AIP Conf. Proc. 778: 345-350

Xue P., Yu T.X., Chu E. (1999). Theoretical prediction of the springback of metal sheets after a double-curvature forming operation. J. Mater. Process. Technol. 90, 65–71.

Xue X., Liao J., Vincze G., Gracio J.J. (2013). Optimization of an asymmetric thin-walled tube in rotary draw bending process. NUMISHEET2014. AIP Conf. Proc. 1567, 1111-1116.

Xue X., Liao J., Vincze G., Gracio J. (2015a). Modelling of mandrel rotary draw bending for accurate twist springback prediction of an asymmetric thin-walled tube. J. Mater. Process. Technol. 216, 405-417.

Xue X., Liao J., Vincze G., Barlat F. (2015b).Twist springback characteristics of dual-phase steel sheet after non-symmetric deep drawing, Int. J. Mater. Form. DOI: 10.1007/s12289-015-1275-2.

Xue X., Liao J., Vincze G., Sousa J.A, Barlat F., Gracio J. (2016). Modelling and sensitivity analysis of twist springback in deep drawing of dual phase steel. Mater. Des. 90: 204-217.

Yang M., Akiyama Y., Sasaki T. (2004). Evaluation of change in material properties due to plastic deformation. J. Mater. Process. Technol. 151: 232–236.

Yang H., Li H., Zhan M. (2010). Friction role in bending behaviors of thin-walled tube in rotary-draw-bending under small bending radii. J. Mater. Process. Technol. 210: 2273-2284.

Yang X.A., Ruan F. (2011). A die design method for springback compensation based on displacement adjustment. Int. J. Mech. Sci. 53(5): 399–406.

Yi H.K., Kim D.W., Van Tyne C.J., Moon Y.H. (2008). Analytical prediction of springback based on residual differential strain during sheet metal bending. J. Mech. Eng. Sci. 222: 117-129.

Yoon J.W., Barlat F. (2006). Modeling and Simulation of the Forming of Aluminum Sheet Alloys. ASM Handbook, Metalworking: Sheet Forming 14B: 792–826.

Young W.C., Budynas R.G. (2002). Formulas for Stress and Strain, 8th edition. McGraw-Hill book company, Englewood Cliffs.

Yoshida F., Uemori T., Fujiwara K. (2002). Elastic–plastic behavior of steel sheets under in-plane cyclic tension–compression at large strain. Int. J. Plast.18:633–659

Yoshida F., Uemori T. (2003). A model of large-strain cyclic plasticity and its application to springback simulation. Int. J. Mech. Sci. 45(10), 1687–1702.

Yoshihara H., Tsunematsu S. (2006). Feasibility of estimation methods for measuring Young's modulus of wood by three-point bending test. Mater. Struct. 39: 26-39.

Yu H.Y. (2009). Variation of elastic modulus during plastic deformation and its influence on springback. Mater. Des. 30: 846-850.

Zang S.L., Lee M-G, Sun L., Kim J.H. (2014). Measurement of the Bauschingerbehavior of sheet metals by three-point bending springback test with pre-strained strips. Int. J. Plast. 59: 84-107.

Zhan M., Yang H., Huang L. (2006). A numerical-analytic method for quickly predicting springback of numerical control bending of thin-walled tube. J. Mater. Process. Technol. 22:713-720.

Zhan M., Huang T., Zhang P.P., Yang H. (2014). Variation of Young's modulus of high-strength TA18 tubes and its effects on forming quality of tubes by numerical control bending. Mater. Des. 53: 809–815.

Zhang D., Cui Z., Ruan X., Li Y. (2007). An analytical model for predicting springback and side wall curl of sheet after U-bending, Comp. Mater. Sci. 38 (4): 707-715.

Zhang J.C., Di H.S., Deng Y.G., Li S.C., Misra R.D.K. (2015). Microstructure and mechanical property relationship in an ultrahigh strength 980 MPa grade high-Al low-Si dual phase steel, Mater. Sci. Eng. A, 645, 232-240.

Zhang Z.T., Hu S.J. (1998). Stress and residual stress distributions in plane strain bending. Int. J. Mech. Sci. 40 (6), 533–543.

Zhao G.Y., Liu Y.L., Yang H., Lu C.H., Gu R.J. (2009). Three-dimensional finite-elements modelling and simulation of rotary-draw bending process for thin-walled rectangular tube. Mater. Sci. Eng. A; 499, 257–261.

Zhu Y.X., Liu Y.L., Yang H., Li H.P. (2012). Improvement of the accuracy and the computational efficiency of the springback prediction model for the rotary-draw bending of rectangular H96 tube. Int. J. Mech. Sci. 66, 224–232.

Zhu Y.X., Liu Y.L., Li H.P., Yang H. (2013). Springback prediction for rotary-draw bending of rectangular H96 tube based on isotropic mixed and Yoshida Uemori two surface hardening models. Mater. Des. 47: 200-209.

Ziegler H. (1959). A modification of Prager's hardening rule. Quarterly of Applied Mechanics; 17: 55–65.

Appendixes

Appendix A

A.1 The experimental 2D springback of the curved-flanging test and the predicted results by using different elastic modulus degradations, which were associated with different loading strategies, are tabulated in this Section.

Table A. 1 Experimental and predicted 2D springback under different loading strategies.

Material	Type	θ_e^f	θ_e^s	R_e	θ_i^s	θ_i^f	R_i
DP500	Exp.	95.250	96.650	160.250	91.050	93.950	168.005
	ULUL	95.481	96.252	143.572	90.689	94.237	162.193
	BLUL	95.271	95.131	158.768	90.108	94.056	166.605
	TPB	95.061	96.603	171.593	91.326	93.803	175.593
DP600	Exp.	95.950	97.300	125.500	91.550	94.500	136.050
	ULUL	96.648	97.950	153.942	91.080	95.173	168.874
	BLUL	94.942	96.514	110.311	90.272	93.674	124.398
	TPB	95.505	97.583	148.232	91.612	94.374	162.103
DP780	Exp.	100.122	95.276	114.950	93.270	94.005	131.686
	ULUL	100.363	97.023	91.920	93.514	94.600	125.813
	BLUL	99.194	95.967	113.413	92.293	94.770	128.831
	TPB	100.072	95.426	111.903	93.014	94.470	126.823

Appendix B

The measured draw-in lengths of the selected trace points by using DIC technique and the predicted results using different friction coefficients are tabulated in this Section.

Table B. 1 Experimental and predicted results of draw-in lengths of the selected trace points.

Trace point	Experiment, (mm)	Numerical results under different friction coefficients, (mm)				
		μ=0.05	μ=0.075	μ=0.1	μ=0.125	μ=0.15
1	30.083	30.730	29.969	29.675	29.060	29.010
2	-36.854	-36.850	-36.828	-36.283	-36.170	-36.050
3	29.575	30.190	29.140	28.610	28.330	28.310
4	-37.399	-37.650	-37.180	-37.040	-36.950	-36.810
5	30.101	30.740	29.969	29.675	29.060	29.010
6	-36.838	-36.850	-36.829	-36.283	-36.070	-35.540

Appendix C

The detailed results of friction coefficient identification by means of numerical inverse model are presented in this Section.

Table C. 1 Experimental plans for the coded values in Table 5-4 and simulation results.

Run	Coded independent variables				Response variables	
	x_1 (μ_1)	x_1 (μ_2)	x_3 (μ_3)	x_4 (μ_4)	Springback angle θ (°)	Twist angle φ(°)
1	-1	1	-1	1	5.81	3.04
2	α	0	0	0	5.23	3.42
3	0	0	0	0	5.57	3.18
4	-1	-1	1	-1	5.42	3.29
5	-1	1	1	1	5.61	3.12
6	1	1	-1	-1	5.43	2.61
7	0	0	α	0	5.08	3.12
8	-α	0	0	0	5.82	3.13
9	0	0	-α	0	5.61	2.65
10	1	-1	1	1	5.14	2.82
11	0	0	0	α	5.61	3.01
12	0	-α	0	0	5.34	2.85
13	1	1	1	-1	5.32	3.28
14	0	α	0	0	5.52	3.03
15	0	0	0	-α	5.34	2.91
16	-1	-1	-1	0	6.39	3.03

Table C. 2 The coefficients of two empirical models.

Model	Coefficients							
	β_0	β_1	β_2	β_3	β_4	β_{12}	β_{13}	β_{14}
$\theta(\mu)$	9.79	-19.2	-7.74	-18.2	-11.3	29.86	52.50	12.15
$\varphi(\mu)$	3.83	-8.25	-2.47	7.56	-7.37	9.88	13.25	19.02
Model	**Coefficients**							
	β_{23}	β_{24}	β_{34}	β_{11}	β_{22}	β_{33}	β_{44}	
$\theta(\mu)$	17.25	23.3	44.50	3.27	-0.6	9.99	-19.2	
$\varphi(\mu)$	9.73	43.2	-38.2	14.82	-6.6	-29.1	-21.6	

Table C. 3 ANOVA for quadratic model of springback angle of thin-walled tube.

Source	SS	DF	MS	F-value	P-value	Evaluation
Model	1.446	14	0.13	9.29	0.0059	Significant
x_1	0.115	1	0.12	10.37	0.0181	
x_2	0.010	1	0.010	0.88	0.3839	
x_3	0.379	1	0.379	34.13	0.0011	
x_4	0.014	1	0.014	1.30	0.2976	
x_1x_2	0.074	1	0.074	6.65	0.0419	
x_1x_3	0.138	1	0.138	12.40	0.0125	
x_1x_4	0.003	1	0.003	0.28	0.6188	
x_2x_3	0.060	1	0.060	5.36	0.0599	
x_2x_4	0.045	1	0.045	4.02	0.0919	
x_3x_4	0.099	1	0.099	8.91	0.0245	
x_1^2	0.001	1	0.001	0.09	0.7744	
x_2^2	0.001	1	0.001	0.05	0.8341	
x_3^2	0.013	1	0.013	1.13	0.3293	
x_4^2	0.002	1	0.002	0.17	0.6938	
Residual	0.067	6	0.011			
Total	1.512	20				

R^2=0.956; SS-sum of square; DF-degree of freedom; MS-mean square

Table C. 4 ANOVA for quadratic model of twist angle of thin-walled tube.

Source	SS	DF	MS	F-value	P-value	Evaluation
Model	0.732	14	0.052	16.75	0.0012	Significant
x_1	0.080	1	0.080	25.61	0.0023	
x_2	0.007	1	0.007	2.30	0.1798	
x_3	0.263	1	0.263	84.10	0.0001	
x_4	0.003	1	0.003	1.02	0.3505	
x_1x_2	0.008	1	0.008	2.59	0.1587	
x_1x_3	0.009	1	0.009	2.81	0.1447	
x_1x_4	0.007	1	0.007	2.40	0.1724	
x_2x_3	0.019	1	0.019	5.93	0.0508	
x_2x_4	0.154	1	0.154	49.40	0.0004	
x_3x_4	0.073	1	0.073	23.42	0.0029	
x_1^2	0.020	1	0.020	6.48	0.0437	
x_2^2	0.065	1	0.065	20.66	0.0039	
x_3^2	0.079	1	0.079	25.35	0.0024	
x_4^2	0.040	1	0.040	12.73	0.0118	
Residual	0.019	6	0.003			
Total	0.750	20				

R^2=0.975; SS-sum of square; DF-degree of freedom; MS-mean square

Appendix D

The measured results of the 2D angular springback of cross sections in the DP500 C-channel are tabulated in this Section.

Table D. 1 The measured 2D angular springback of the intrados and extrados flanges under different material directions.

Section	**Intrados flange springback, α1**			**Extrados flange springback, α2**		
	0º	**45º**	**90º**	**0º**	**45º**	**90º**
-30º	3.067	3.244	2.784	5.029	4.980	5.779
-20º	3.158	3.445	2.939	4.710	4.755	5.528
-10º	3.361	3.573	3.006	4.500	4.602	5.328
0º	3.662	3.728	3.163	4.344	4.54	5.257
10º	3.390	3.505	3.005	4.579	4.782	5.378
20º	3.286	3.400	2.880	4.838	5.120	5.407
30º	3.109	3.180	2.820	4.996	5.300	5.474